HEAT TRANSFER ANALYSIS OF A PROPOSED FUEL ASSEMBLY FOR SUPERCRITICAL WATER REACTORS USING STAR-CCM+ CFD CODE

A thesis presented to the:

Department of **MEDICAL PHYSICS**

GRADUATE SCHOOL OF NUCLEAR AND ALLIED SCIENCES

UNIVERSITY OF GHANA

BY

CHABI SILAS, 10633008

BEng, the Copperbelt University, Zambia, 2013

In partial fulfillment of the requirements of the award of

MASTER OF PHILOSOPHY

IN

NUCLEAR SCIENCE AND TECHNOLOGY PROGRAM

JULY, 2018

DECLARATION

This thesis is a result of research work undertaken by Silas Chabi in the Department of Medical Physics, School of Nuclear and Allied Sciences (SNAS), University of Ghana, under the supervision of Dr. Seth K. Debrah and Dr. Edward Shitsi.

…… Date: …….
Silas Chabi
(Student)

…… Date: ……
S. K. Debrah, PhD
(Principal Supervisor)

…… Date: ……...
E. Shitsi, PhD
(Co-supervisor)

ABSTRACT

Accurate knowledge and understanding of heat transfer characteristics near and above critical conditions is crucial to the successful design of the SCWR. Many studies, both numerical and experimental assessments have been conducted on bare tubes and simple geometries like annuli. However, heat transfer performance studies of the fuel assemblies for SCWR are scarce. Thus, there is still a lack of understanding of heat transfer performance in the fuel assembly designs for SCWR. Moreover, the importance of this study cannot be over-emphasized as it will broaden and better the understanding of the concept of heat transfer in the rod bundle geometry by providing more numerical data.

In this study a 3D CFD code STAR CCM+ was used in assessing the performance of heat transfer in the square fuel assembly of a High Performance Light Water Reactor (HPLWR). Utilizing the computational environment and the flexibility of STAR CCM+ code, test analysis was conducted using the four turbulence models, namely AKN low-Re, Standard Lien's low-Re, Standard Wilcox κ-ω and SST κ-ω to choose a suitable turbulence model yielding satisfying prediction (capabilities) in describing the heat transfer and flow of supercritical water in the fuel assembly "near", at and after the pseudo-critical region. The analysis was carried out at 25 MPa system operating pressure, mass flow rate of 0.167 kg/s (601.2 kg/h), 300 °C inlet temperature with uniform heat flux of 650 kW/m^2. Turbulence sensitivity analysis was performed and SST κ-ω model was selected based on its simplicity and superiority to others especially with regard to numerical stability. Moreover, SST κ-ω model also does not involve damping functions, but allows simple Dirichlet specified boundary conditions

Furthermore, using the SST κ-ω with low $y+$ wall treatment the selected heat transfer correlations were assessed. Overall, the Cheng et al. correlation provided the most satisfying prediction for the wall temperatures in all the sub-channels and captured closely Wataa's Numerical data. This was followed by the McAdams correlation, but the Dyadyakin and Popov and the Petukhov correlations also yielded acceptable results.

Test analysis results of the heat transfer correlation also confirmed the occurrence of heat transfer enhancement and heat transfer deterioration at the pseudo-critical point and after or beyond respectively. The maximum wall temperature was obtained in sub-channel 9, the hottest sub-channel and exceeded the design limit of 620 °C by 60 °C for the Cheng correlation while for the other correlations it was more. The difference in temperature between the hottest and coldest sub-channels was approximately 80 °C.

Finally, parametric analysis was conducted in sub-channels 4 and 9 by varying mass flow rates 0.1670 kg/s (601.2 kg/h) and 0.1559 kg/s (561.2 kg/h), pressure 23 MPa and 25 MPa and with or without gravity. Results from this test analysis showed that mass flow rate, pressure and gravity have significant influence. It was observed that at low mass flow rate with varying pressure (23 MPa and 25 MPa), the temperatures significantly increased in the heat transfer deterioration region. Nevertheless, experimental investigations involving rod bundles adopted in this study should be conducted to validate the results obtained numerically and address the inconsistence of the conclusions drawn, "when compared with similar studies". These experimental studies would also be helpful in validating similar numerical studies in future.

DEDICATION

This thesis work is dedicated to my unborn child, my brothers, Humphrey Chabi, Chiluba A. Chabi and my sisters, Elizabeth Chabi, Bwalya SC. Kaoma, Alice Bwalya and Sylvia M Chabi. Special mention, my Father and Mother, mentor and role models since childhood Mr. AM and Mrs. S Chabi, an ocean of wisdom, knowledge and experience. Thank you for continuously refining and polishing me to be a man that people take pride in

TABLE OF CONTENTS

APPENDICES

LIST OF TABLES

LIST OF FIGURES

NOMENCLATURE

C_p	Specific heat capacity [kJ/kg]
$\bar{C}_p$	Mean specific heat, $\frac{H_w - H_b}{T_w - T_b}$ $[\frac{kJ}{kgK}]$
D_{hy}	Hydraulic diameter [mm]
G	Mass flux [kg/m^{2}s]
Gr	Grashof number, $\frac{(\rho_b - \rho_w) g D_{hy}^3}{\rho \nu^2}$ [-]
Gr*	Grashof number based on heat flux, $\frac{g \beta D_{hy}^4 q}{\lambda \nu^2}$ [-]
H	enthalpy [kJ/kg]
g	gravity [m/s^2]
h	heat transfer coefficient [kW/m^{2}K]
k	thermal conductivity [W/m.K]
q	Heat flux [W/m^2]
T	temperature [°C]
$\overline{Pr}$	Mean Prandtl number, $\frac{\mu \cdot \bar{C}_p}{\lambda}$ [-]
Nu	Nusselt number, $\frac{h D_{hy}}{\lambda}$ [−]
Pr	Prandtl number, $\frac{\mu C_p}{\lambda}$ [−]

Re	Reynolds number, $\frac{GD_{hy}}{\mu}$ $[-]$
U, V and W	Velocity components in *x, y and z* directions
S	Source term
P	Pressure (Pa)

Subscripts

b	*bulk*
col	*coolant*
fcl	*fluid centre-line*
hy	*hydraulic*
in	*inlet*
w	*wall*

Greek letters

α	Thermal diffusivity [m^2/s]
β	Thermal expansion coefficient [1/K]
ε	Turbulent dissipation rate
κ	Kinetic energy [J]
λ	Thermal conductivity [W/mK]

μ Dynamic viscosity [Pa·s]

μ_t Turbulent viscosity

ν Kinematic viscosity [m^2/s]

ρ Density [kg/m^3]

τ viscous stresses

ω Specific dissipation rate

Δ Change in a specific quantity

ACRONYMS

ATHLET	Analysis of Thermal-hydraulics of Leaks and Transients
CFD	Computational Fluid Dynamics
CR	Control Rods
EURATOM	European Atomic Energy
FA	Fuel Assembly
FFFPPs	Fossil Fuel Fired Power Plants
GIF	Generation IV International Forum
HPWLR	High Performance Light Water Reactor
HTC	Heat Transfer Coefficient
HTD	Heat Transfer Deterioration
HTE	Heat Transfer Enhancement
LOCA	Loss of Coolant Accidents
MCNP	Monte Carlo N-Particle code
NHT	Normal Heat Transfer
pc	Psuedo-critical
PT	Pressure Tube
PV	Pressure Vessel
RANS	Reynolds-Averaged Navier-Stokes
RPV	Reactor Pressure Vessel
SC	Sub-channel

SCW	Supercritical Water
SCWR	Supercritical Water Reactor
Sdr	Specific dissipation rate
sq	Square
STAFANAS	Sub-chanel Themal-Hydraulic Analysis of a Fuel Assembly design under Supercritical conditions
STAR-CCM+	Simulation of Turbulent flow in Arbitrary Regions Computational Continuum Mechanics C ++ based
SST	Shear-Stress Transport

ACKNOWLEDGEMENT

I wish to heartily acknowledge and gratefully thank God Almighty for blessing and allowing me to receive the fellowship award from International Atomic Energy Agency (IAEA) and the Government of Zambia to undertake studies in Ghana.

My profound gratitude to my supervisors Dr. S.K Debrah and Dr. Edward Shitsi whose guidance, conscientiousness and meticulous attention to detail was instrumental in the write-up of this thesis.

In the same vein, my profound gratitude also goes to Prof. Yaw Serfor Armah, Emeritus Prof. E.H.K Akaho, Prof. C. Shandorf, Prof. G. Emi- Reynolds, Dr. D Adotey, Dr V.Y Agbodemegbe, Dr Ampomah Amoako, Dr R.B. M Sogbadji, Dr. Danso, Rev. Dr. A. Bamford, Dr. O. Gyampo and Dr. R. Abrefah for the priceless impartation of knowledge. I would also like to thank Mr. Reuben Katebe at National Institute for Scientific and Industrial Research (NISIR) and Dr. J. Siame Chemical Engineering Head of Department, at the Copperbelt University, Riverside Campus, Zambia for their confidence in me and awarding me this opportunity. May God richly bless you.

Finally, I also wish to record my heartfelt thanks to my dearest friend and partner Thandiwe Phiri for her invariable support and encouragement I received while doing this research work, also my family, special friends (Mr. Elias Mwape, Miss Ruth Nana Njantang and Miss Joana Otoo), advocates, CD-ADAPCO and everyone who contributed in many different ways and provided continuous support in this effort.

CHAPTER ONE : INTRODUCTION

This chapter outlines the phenomenon of the performance of heat transfer of a proposed fuel assembly for SCWR and establishes the justification for the study in association with the problem statement.

1.1 Background

The demand for energy globally has continued to increase, and growing concerns relating to the safeguarding of the environment, are envisaged to favor sources of energy with less impact on the environment in an economically competitive era. In this regard, Nuclear Power Plants (NPPs) have a pivotal role to play in developing the supply of future energy, new goals as well as challenges which the energy sector and market poses [1]. Some of the key goals for the SCWR technology as indicated in the Generation IV Roadmap [2], are reliability and safety that focus on the operation being safe and reliable and also protection of the investment, thus improving public acceptability. However, economic goals are focused on competitive life cycle and the cost of production for the energy and financial risk.

In view of the above aforementioned, supercritical pressure water cooled reactor (SCWR) has been regarded as an innovative nuclear reactor by the Department of Energy (DOE) in the United States [3]. The performance of heat transfer under supercritical pressure is one of the most significant indicators for the design and development of the SCWR [4]. As the sixth candidate of the Generation IV reactor concept, this reactor is envisaged to be operated at supercritical pressure (i.e. greater than 22.1 MPa). The term supercritical shouldn't be mistaken for the term criticality that gives the definition of the changes in

neutron population in the reactor core. However, in this context the conditions above the thermodynamic critical point (i.e P_{cr} = 22.1 MPa, T_{cr} = 374) of water is referred to as supercritical conditions.

One of the remarkable features of SWCR is that above the critical point of water, boiling crisis or a distinct change from liquid to gas cannot occur within the core during operation. This in turn makes the design safer. Conversely, a higher temperature of about 620 ˚C for the cladding and a significant change of the coolant density by more than a factor of seven are some the design challenges of the fuel assembly design [5].

A general layout illustrating the proposed Reactor Pressure Vessel (RPV) of SCWR is shown in Figure 1.1. The core arrangement is similar to that of a PWR, ("lower half of the RPV"). Additionally, control rods are introduced at the top part of the RPV. Feed water entering the RPV is supplied via down-comer to the bottom-part of the reactor core "lower plenum" and also to the top-part of the core "upper plenum", where it flows as moderator water downwards [5]. The closed steam plenum on the upper part of the core will supply the generated steam to the turbines. This closed steam plenum is required for this counter current flow of moderator water and rising coolant, however moderator water is allowed to flow to the upper part of the core. Since core feed water as well as moderator water via the down-comer needs to be homogeneously mixed at the lower part of the core, a mixing plenum underneath the core is used.

Researchers, Schulenberg and Starflinger [6], optimized the fuel assemblies of the first hexagonal and square concepts of HPLWR with regard to a uniform neutron flux, coolant

heat-up and low temperature of the cladding surface reaching a high power density of the core.

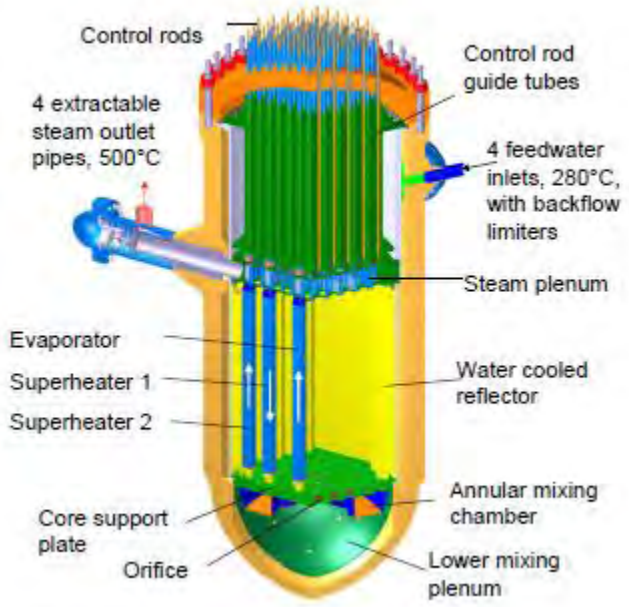

Figure 1.1: Reactor pressure vessel and core structures for a typical European HPLWR [7]

1.2 HPLWR Fuel Assembly Concept Overview

High Performance Light Water Reactor (HPLWR) is a European SCWR concept which uses supercritical water as a moderator and coolant. The concept can either be designed as fast or thermal reactor. Above the critical point (22.1 MPa) water is in single phase. Consequently, it is envisaged that the plant system will be simpler and more compact than PWRs and Boiling Water Reactors (BWRs) without a dryer, water-steam separators and recirculation pumps. At supercritical pressure, the coolant temperature is very high as there is no limitation of saturation temperature.

In general, SCWR fuel assembly concepts can either be classified as square (sq) or hexagonal (hex) configuration of fuel rods as reported by Hofmeister et al [5]. With this concept, the flow of coolant is upwards between the rods, while the moderator water flows downwards within the moderator box and in the gaps between the fuel assembly boxes. Fuel rods with a diameter of 8 mm and 1.15 P/D (pitch to diameter) ratio for a square type assembly were first proposed by Cheng et al. [8] based on the outcome of the preliminary results obtained from the sub-channel analysis. While for hexagonal a P/D ratio of 1.3 was considered. The spacing between the rod and box wall for each fuel assembly design, has been optimized to 1 mm.

3D-models of two squares ("sq1. 1" and"sq2. 1") and ("hex 1.1" and "hex2. 1") are illustrated as shown in Figure 1.2 and 1.3.

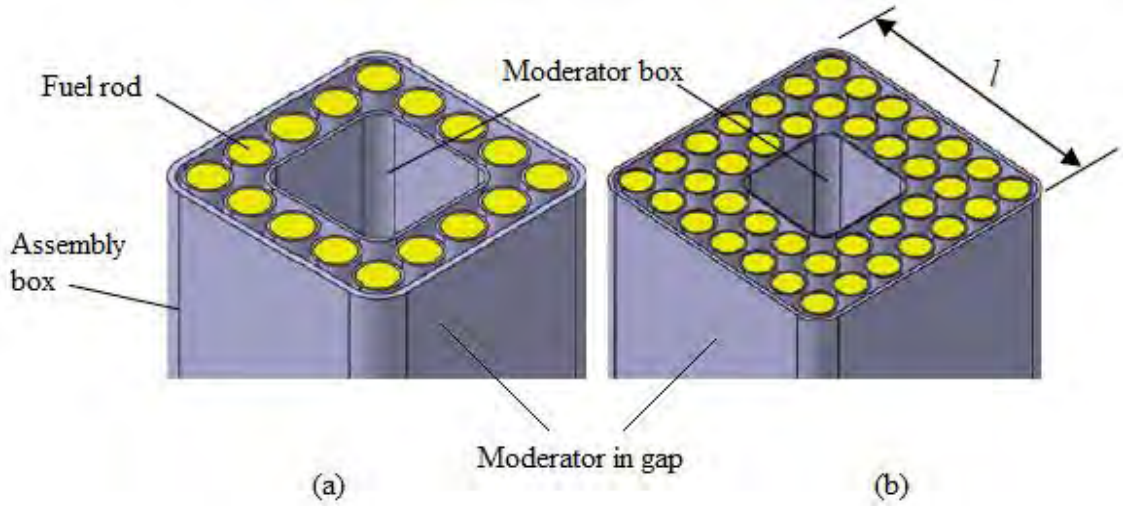

Figure 1.2: Square type fuel assemblies; (a) "sq1.1" and (b) "sq2.1".

[5]

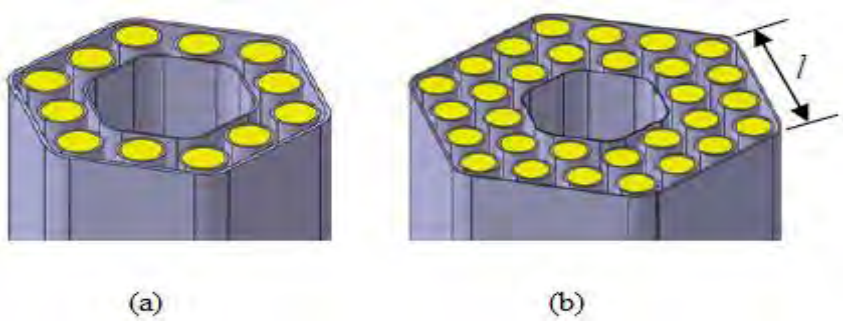

Figure 1.3: Hexagonal type fuel assemblies: (a) "hex1.1" and (b) "hex2.1". [5]

A systematic design study conducted by Hofmeister et al. [5] proved that a 2.1 square fuel bundle has the following advantages, namely structural material is minimized, the moderator to fuel ratio is optimized and there is a reduction in the fuel rod power [5].

1.3 Heat Transfer Studies in Supercritical Fluids and FA

A supercritical fluid is any fluid at a pressure higher than its critical pressure. In effect, supercritical fluids exhibit features of both liquid and gas, even though distinct liquid and gas phases do not exist at supercritical pressures. For instance, supercritical fluids can diffuse and completely fill up a container like a gas, while also being able to dissolve other substances like a liquid. Because of the single-phase nature of supercritical fluids, using them as coolant in a nuclear reactor can eliminate some of the potential safety issues that are inherent to reactors operating at subcritical pressures. For example, "boiling crisis" would not occur in a SCWR since supercritical coolant does not change phase. However, as shown in Figure 1.4, the thermo-physical properties of a supercritical fluid vary drastically when the temperature is near the vicinity of pseudo-critical temperature, defined as the temperature at which the specific heat is maximum.

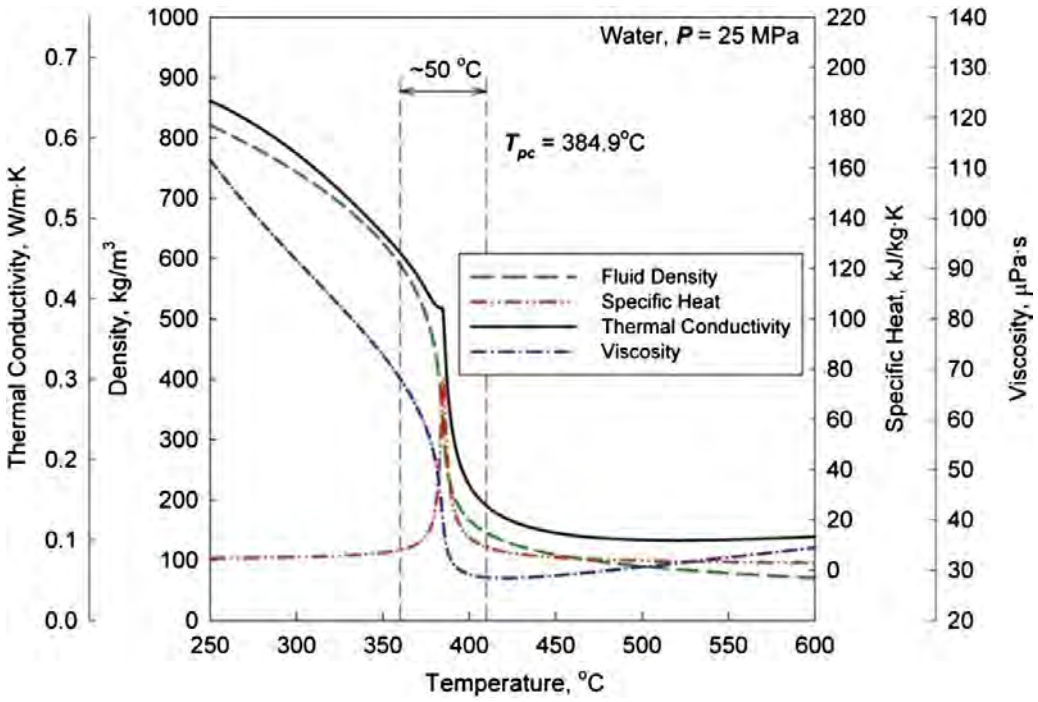

Figure 1.4: Property changes of water at 25 MPa [9]

This in turn can cause unusual heat transfer behaviour under certain circumstances. So far three different heat transfer modes have been observed in previous works [10]:

- Normal heat transfer, in which case the heat transfer coefficient (HTC, an indication of the efficiency of heat transfer) can be easily predicted by established correlations.
- Heat transfer Deterioration (HTD), with values of the HTC that are relatively low within a part of a test section; it usually occurs in tubes at high heat fluxes and low mass fluxes and is thought to be due to buoyancy forces and/or flow acceleration (Fewster and Jackson, [11]). This mode can be suppressed or even eliminated by the presence of turbulence-enhancing devices such as the spacer grids or wire-wraps.
- Enhanced heat transfer, with relatively high values of the HTC within some part of a test section.

Figure 1.5 (a) and (b) shows one of the previous experiments in which all three modes were observed. The prediction of the occurrences of these modes is crucial to the successful realization of a complex yet safe heat and mass transport system suitable for the SCWR.

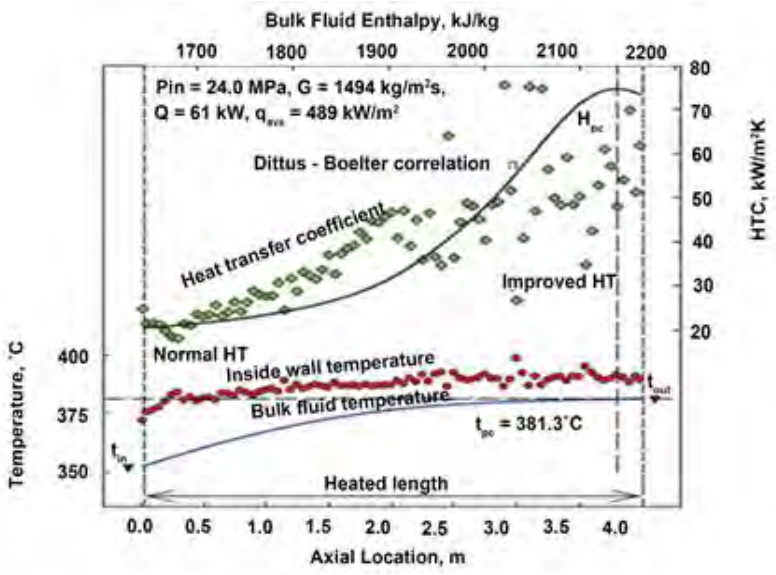

Figure 1.5: Three different heat transfer modes in SCW along the heated length of a vertical circular tube (a) and (b) [12]

The high enthalpy rise observed in the core facilitates the use of two- and three-pass cores, which contributes to the reduction of the maximum cladding temperature, but in turn increases the complexity of core design [13].

1.4 Statement of the Problem

Several designs for the SCWR assemblies based on square and hexagonal geometry have been proposed by researchers Dobashi et al. [14], Yamaji et al. [15] and Hofmeister et al. [16]. However, accurate knowledge and understanding of heat transfer characteristics near and above critical conditions is crucial to the successful design of the SCWR. Many studies, both numerical and experimental assessments, have been conducted on bare tubes and simple geometries like annuli. Even though heat transfer performance studies of the FAs for SCWR are still scarce, not much numerical analyses have been performed to validate the ability of the various heat transfer codes in terms of their accurate prediction of heat transfer. Thus there is still lack of understanding of heat transfer performance in the FA designs for SCWR. In this regard, in a bid to contribute to the extension of current knowledge of heat transfer in the fuel rod assembly designs of a SCWR, it is imperative that this research study is conducted.

1.5 Main Objective

The main objective of this study is to evaluate numerically heat transfer performance of a proposed Fuel Assembly Design [5] for SCWR using STAR CCM+ CFD code.

1.5.1 Specific Objectives

- To evaluate the performance of some selected turbulence models in order to select the best turbulence model for the numerical simulations. The evaluation will be performed by comparing the results of these selected turbulence models with the available numerical results of Waata [17].
- To conduct analysis of some developed heat transfer correlations for the assessment of heat transfer in the proposed fuel assembly using STAR-CCM+ computer code,
- To carry out a parametric and sub-channel analysis of the proposed SCWR fuel assembly design using STAR-CCM+ computer code.

1.6 Relevance and Justification

Merging the present advanced technology of nuclear and fossil fuel or coal fired plants will equate to SCWRs. In principle, higher efficiency coupled with improved economics qualifies the SCWR concept to be competitive with the current conventional reactor design. Heat transfer analysis is performed in order to predict the temperature field in the reactor core. The temperature prediction in the reactor core is important for the safety of the design and operation of the SCWR. Thus the importance of this study cannot be over-emphasized as it will broaden and better the understanding of the concept of heat transfer in the rod bundle geometry by providing more numerical data. This work will also contribute to addressing safety concerns of the design and operation of SCWR.

1.7 Scope and Limitation

The primary aim of this work is to perform heat transfer analysis in $1/8^{th}$ of the square fuel assembly proposed for HPLWR. The analysis is limited to conditions at supercritical

pressures. Thus only single phase flow modelling using STAR CCM+ CFD code has been considered in this work.

1.8 Thesis Structure

This thesis comprises five chapters. Chapter one provides an introduction and background to the study. It also emphasizes the importance of this work and its contribution to current knowledge on heat transfer and distribution in research reactors. Chapter two gives insight on the work performed in the study of heat transfer in SCWRs and highlights the knowledge gaps that need to be addressed by this research. A comprehensive discussion of the fundamentals of the STAR-CCM$^+$ code and its relevant features utilized in the computational modelling and analysis of the fuel assembly of SCWR is also undertaken in this chapter. Chapter three outlines the methodology employed for the analysis of heat transfer performance of FA for SCWR. It also discusses the geometry design, computational models used, boundary conditions and relevant parameters utilized in the research as well as explanations of the various processes undertaken by the code during computation. The results obtained from the study are clearly and logically presented in Chapter 4. Chapter five concludes the study and gives an overall summary of the research and recommendations for future studies.

CHAPTER TWO : LITERATURE REVIEW

Introduction

The Supercritical-Water-Cooled Reactor (SCWR, shown in Figure 2.1) is the sixth candidate of the advanced, fourth generation nuclear reactor concepts proposed by the "Generation IV International Forum (GIF)" [18] a consortium of thirteen member countries that lays the groundwork for the fourth generation of nuclear energy systems. Operating with water at pressures higher than the thermodynamic critical pressure, SCWRs are expected to have superior thermodynamic efficiency.

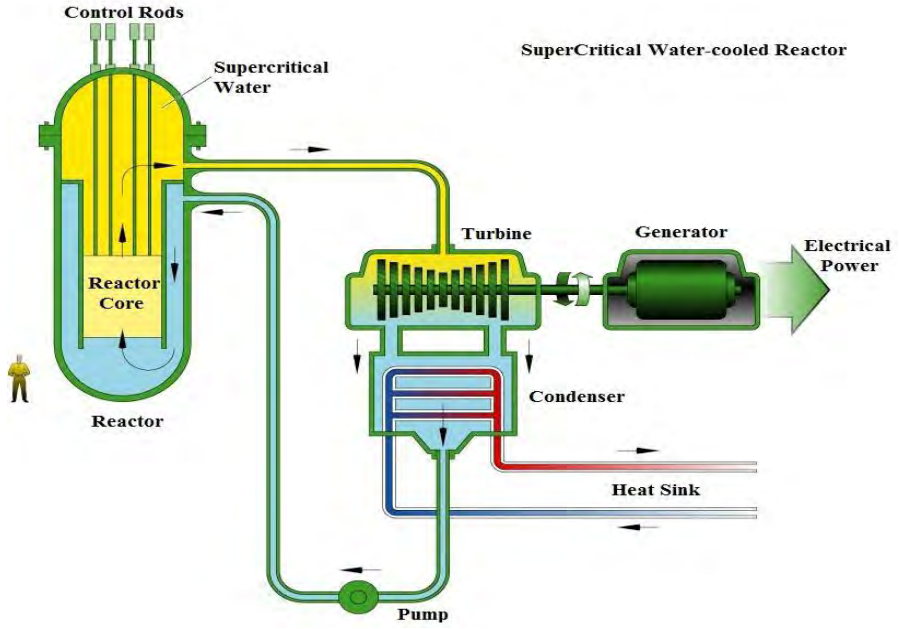

Figure 2.1: Pressure-Vessel Super Critical Water-cooled Reactor (PV SCWR) NPP concept [19]

Once constructed, they will be able to produce safe and clean energy at reduced cost compared with the current generation of nuclear reactors. Since its inception in January 2000, GIF has been overseeing a large amount of research and development (R&D) activities conducted in its member countries.

The primary aim of GIF is to complete R&D of the SCWR by 2020 and deploy it commercially around 2030 [20].

2.1 Development status and progress of SCWRs

As reported in the Generation IV International Forum (GIF) Annual Report [18], development of proposed concepts for SCWR by the following GIF Member States namely Japan, EURATOM and Canada have been completed successfully, reviewed by international peers and their viability assessed. Currently, these Member States are working on R&D to improve confidence on the developed concepts. The proposed concepts for SCWR plants are illustrated in Figure 2.2. The general information about the SCWR is presented in Table 2.1.The Japanese and EURATOM's core concepts are pressure vessel (PV) type, while the Canadian one is pressure tube (PT) type. The developed core concepts for both EURATOM and Canada are thermal spectrum. In contrast, two core concepts developed by Japan are one with a fast spectrum and the other with thermal (both having the same plant concept) [18].

Moreover, China and Russia Federation have continued to work on the development and completion of their PV-type core. Nonetheless, a thermal spectrum configuration is being developed by China while the Russian Federation is developing and working on a fast spectrum core concept. Plans by Peoples Republic of China to host a review of their concept with international peers is scheduled to take place in the year 2018 [18].

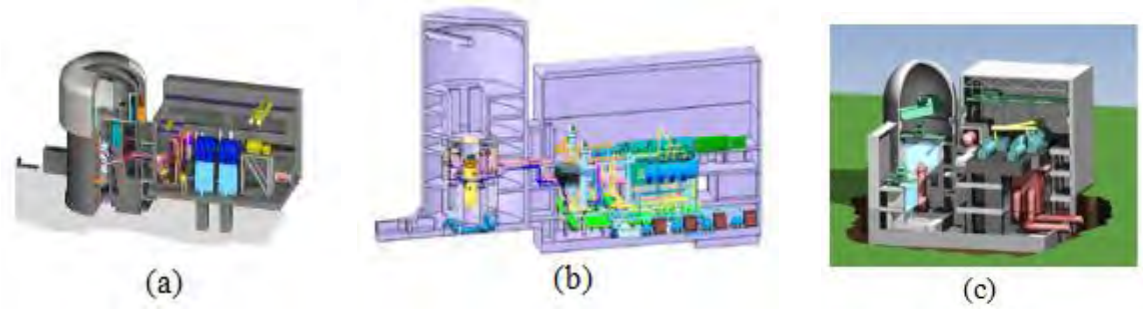

Figure 2.2: Proposed concepts for the SCWR plant [Canada (a), EURATOM (b) and Japan (c)] [18]

A generation capacity of 1000 MW power has been proposed for all the developed core concepts for SCWR except for a super-fast reactor by Japan, this has been considered to be excessive especially for small communities in remote areas. Interests to developing small SCWR concepts with a capacity ranging from 10-300 MW in electric power has increased due to the adjustment of the core of SCWR being flexible. Establishment of the project plan to pursue the success of the development is ongoing. As Pioro et al. [21] indicated, data that has been obtained for FFFPPs (Fossil Fuel Fired Power Plants) can be useful in the heat transfer prediction of supercritical water (SCW). Code validation for fuel bundles with complex geometries if available needs to be done with bundle experiments. An upgrade including supercritical water and a safety feature of depressurizing transients' conditions to subcritical conditions has been done on Codes for analyzing transient safety in systems [21]. Numerical studies on stability of the flow in the core has also been done. Equally in BWRs, using suitable inlet orifices in fuel assemblies flow stability can be ensured.

Table 2.1: SCWR Concepts Key Parameters

Countries	**Canada**	**China**		**EU**	**Japan**		**Russian Federation**
Type	PT	PV	PV	PV	PV	PV	PV
Spectrum	Thermal	Thermal	Mixed	Thermal	Thermal	Fast	Fast
Pressure (MPa)	25	25	25	25	25	25	24.5
Inlet Temp. (˚C)	350	280	280	280	290	280	290
Outlet Temp (˚C)	625	500	510	500	560	501	540
Thermal Power (MW)	2540	2300	3800	2300	3794	1602	3830
Efficiency	48	43	44	43.5	46	44	45
Active Core Height (m)	5	3	4.5	4.2	4.2	2.4	4.07
Fuel	Pu-Th(UO_2)UO_2	UO_2	UO_2/MOX	UO_2	UO_2	MOX	MOX
Moderator	D_2O	D_2O	H_2O	H_2O/–	H_2O	-/ZrH	–
# of Flow Passes	1	2	2	3	1⁄2	1⁄2	1⁄2

2.2 Previous related work on the One-eighth Fuel Assembly

Extensive research and development (R&D) activities covering a broad range of the SCWR development have been carried out in recent past years, the “High Temperature Supercritical-Pressure Light Water Reactor” (SCLWR-H) and the Super Light Water Reactor (Super LWR) were proposed in Japan [15, 22]. The square arranged fuel assembly with single row of fuel rods between water rods was used in these proposed designs. Neutron moderation in these designs was improved by the water rods. However, these same water rods also causes heterogeneous moderation. Similarly, the square fuel assembly has

been used in the HPLWR design studies [6, 23]. As for this assembly (sq), two rows of fuel rods surrounds one water rod in the center. In overcoming heterogeneous moderation, fuel rods having lower enrichment are strategically placed in the corner of the fuel assembly. Another solution of addressing moderation problem is a fuel assembly having a double row of fuel rods with a central moderator box double as recommended by Zhao [24], Liu and Cheng, [25]. Their finding was obtained from a square assembly. In addition, a more uniform moderation was achieved on a double-row-rod assembly as compared to the one-row-rod assembly [26]. A number of research works to achieve maximum power in both PWRs and BWRs has been conducted by many researchers as observed by Schulengberg et al. [7]. This was done by optimizing the geometrical parameters of their annular fuel assemblies.

Furthermore to study and analyze the performance of heat transfer (effects, behaviour) in the proposed design of a fuel assembly for high performance light water reactor proposed by Hofmeister et al. [16]. STAR CCM+ CFD code was used. However, from the previous related work coupled STAFAS with MCNP codes were used in the analysis of Coupled Neutronics/Thermal-hydraulics analysis of HPLWR by Waata [17]. Details of the fuel assembly analyzed are presented in the subsequent sections.

The fuel assembly configuration comprises of a 7 × 7 fuel pin arrangement with a central moderator box, the lattice is square as illustrated in Figure 2.3. The fuel pins have 8 mm as an outer diameter with 0.15 mm being the gap between the fuel pellet and cladding, and 0.5 mm thickness of the cladding. As reported by Waata [17], 1.15 was considered and taken to be the pitch-to-diameter ratio (P/D). An active axial length of 4.2 m was considered and modelled while the inactive part of 0.255 m of the fuel rod bundle in this study was

not included. Table 2.2 shows the design parameters of the fuel rod bundle. Taking advantage of the symmetry capabilities, modelling for the test analysis was only done for one-eighth section of the square fuel bundles.

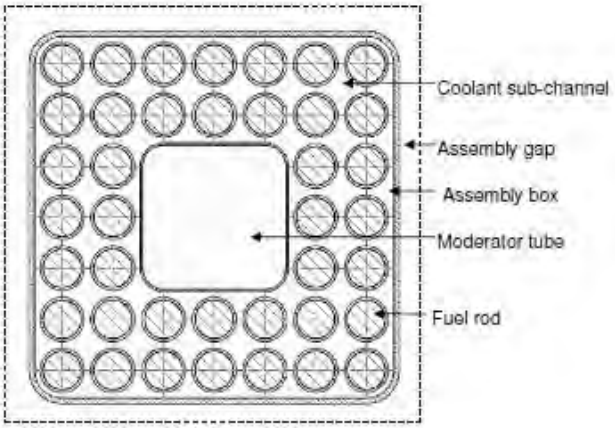

Figure 2.3: The HPLWR Fuel assembly design [26]

Details of the 1/8th fuel assembly is illustrated in Figure 2.4. The assumption of symmetry decreases the number of sub-channels to 9 and that of fuel pins to 7 as labeled in Figure 2.4.

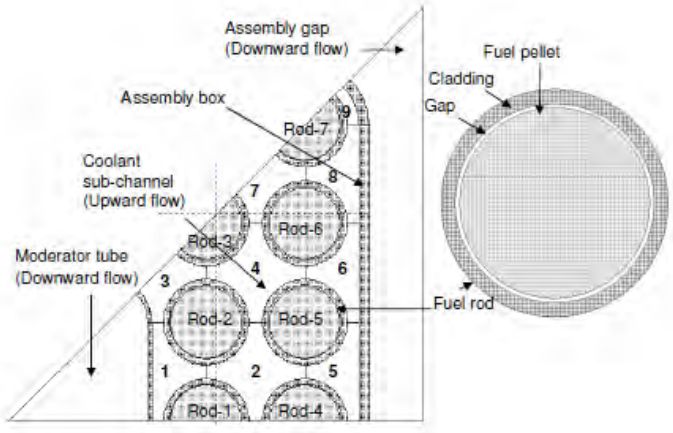

Figure 2.4 : A one-eighth symmetrical square fuel assembly labelled 9 with sub-channel and 7 fuel rods [25]

Table 2.2: Geometry data for a fuel assembly

Parameters	**Values**
Outer diameter of a fuel rod (mm)	8.0
Thickness of Cladding (mm)	0.5
Pitch/Diameter ratio (P/D)	1.15
Active axial length (m)	4.2
Inactive part below and above the active part (mm)	255
Moderator box length (mm)	26
Half gap around one fuel assembly (mm)	5.0
Gap between fuel rod and box wall (mm)	1.0

As proposed by Bittermann et al. [27] the downward flow of the moderator water was considered and maintained in Waata's work. As shown in the Figure 2.5, the flow path of the coolant through the core in the RPV.

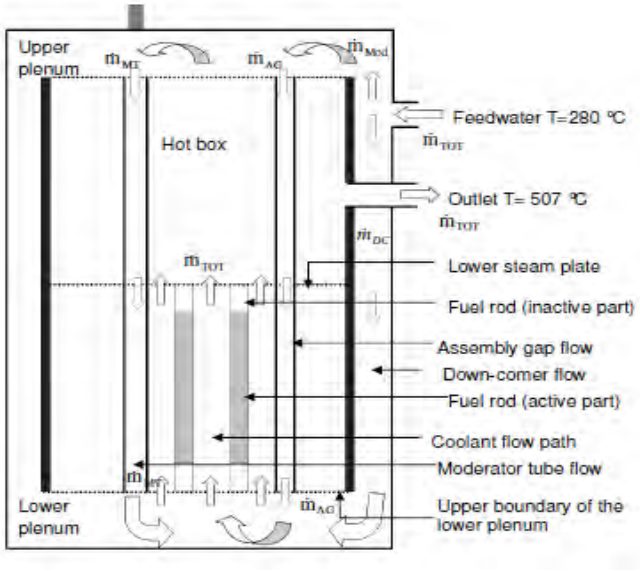

Figure 2.5: The main flow path feed water in the RPV for HPLWR [17]

The feed water enters into the RPV at an inlet temperature of 280 ˚C, where it was split into two parts. The assumption made for the analysis of sub-channels was that 75% of the feed water m_{TOT} was supplied to the lower plenum via down-comer and the remaining 25% flowing downwards served as the moderator water m_{Mod} to the upper plenum. The moderator boxes were provided with a flow split of one-third of the moderator water m_{Mod}, and in order to get an equivalent mass flux in all the moderator systems the assembly gaps m_{AG} were supplied with the remaining fraction of two-third. All feed water m_{TOT} and moderator water m_{Mod} via the down-comer was mixed ideally in the assembly foot piece as illustrated in Figure 2.5. The mean average coolant outlet temperature value of 500 ˚C at the exit of the reactor pressure vessel was assumed [17].

2.2.1 The Power Used and Implemented

A total mass flow rate of 0.167 kg/s and the total power of 327.5 kW was assumed for the test analysis for the one-eighth fuel assembly, from the average outlet temperature of the

coolant was numerically evaluated. Based on these assumptions, Waata calculated a total thermal power of 2620 kW [17]. A core configuration with 88 clusters and 9 fuel rod assemblies per cluster having a square fuel assembly design was proposed (Hofmeister et al. [5]). Consequently, 2075 MW as total thermal power was obtained translating into 9% less than that proposed by Bittermann et al. [27]. The average rod power of 15.6 kW/m and 104 MW/m^3 as an average power density, was evaluated for this FA configuration. The energy generation per unit volume of the core is similar to that of a typical PWR.

Using STAFAS a sub-channel code for the thermal-hydraulics analyses of coolant properties beyond the critical point with separate moderator channels, the parameters presented in Table 2.3 were taken into account.

Table 2.3: Parametric data for the one-eighth square FA

Parameters	**Values**
Coolant exit temperature (˚C)	507
Average rod power (kW/m)	15.6
Power density (MW/m^3)	104
Total power of the 1/8th FA (kW)	327.5
Average coolant mass flux (kg/m^{2}s)	890.3

MCNP was used to calculate the distribution of power in each individual fuel rod, which was subsequently imported into STAFAS to get the equivalent thermal-hydraulic conditions in each individual sub-channel [28]. Furthermore, the coupled system code was tried on a proposed HPLWR fuel assembly.

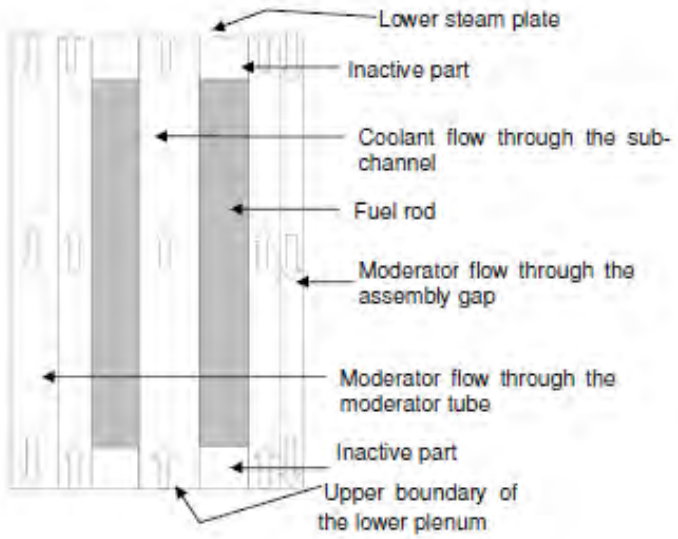

Figure 2.6: Cross-section of one-eighth vertical FA

Figure 2.6 shows the vertical cross section of the FA. The convergence was achieved by introducing an under-relaxation. Satisfactory convergence was obtained with the test results having a value of 0.2 as an "under-relaxation factor". Test analysis results obtained indicated that the power profile in the axial direction of the fuel rod bundle for HPLWR had two peaks. As illustrated in Figure 2.7, due to strong moderation from the coolant in the lower part a stronger peak is observed and a weaker one in the upper part triggered by the moderator water. In an effort to reduce hot spot streaks at the corner walls of the rod bundle and also obtain a power profile with a uniform distribution, a 5% uniform UO_2 was assumed for all the inner most fuel pins, while the corner rod was enriched to only 4%. Temperature with uniform distribution in any cross section was also realized. The local maximum cladding temperature of the fuel assembly was found to be within the allowable limit of 620 ˚C [17].

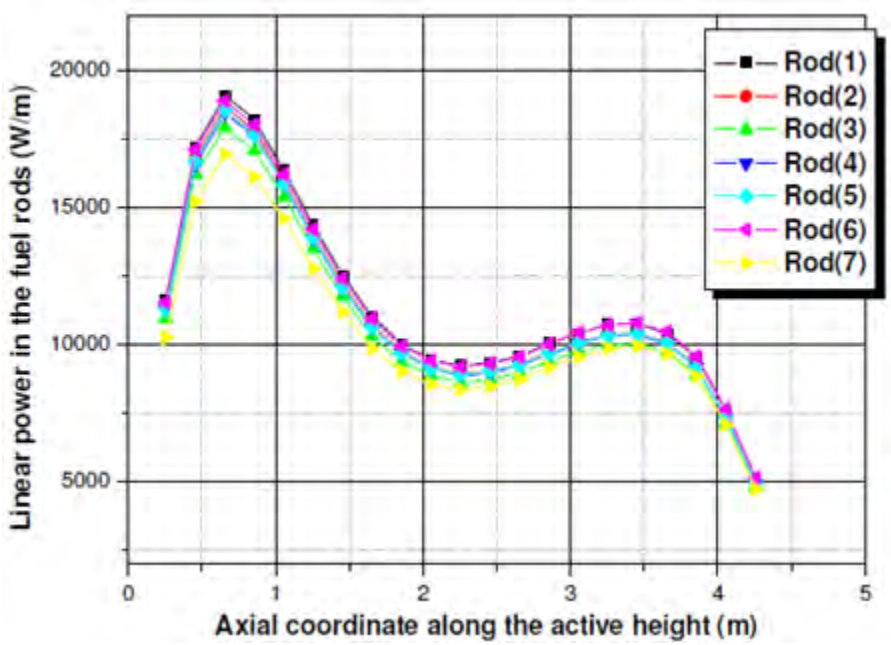

Figure 2.7: Axial power profiles of the fuel pins in a "sq2.1 assembly" [17].

2.2.2 Temperature Profiles in the Sub-channels

The graph in Figure 2.8 presents the distribution of coolant temperatures of individual sub-channels along the total height of the fuel assembly obtained by Wataa [17]. The average exit temperature of 507 ˚C was evaluated for this assembly which is within the design set outlet temperature.

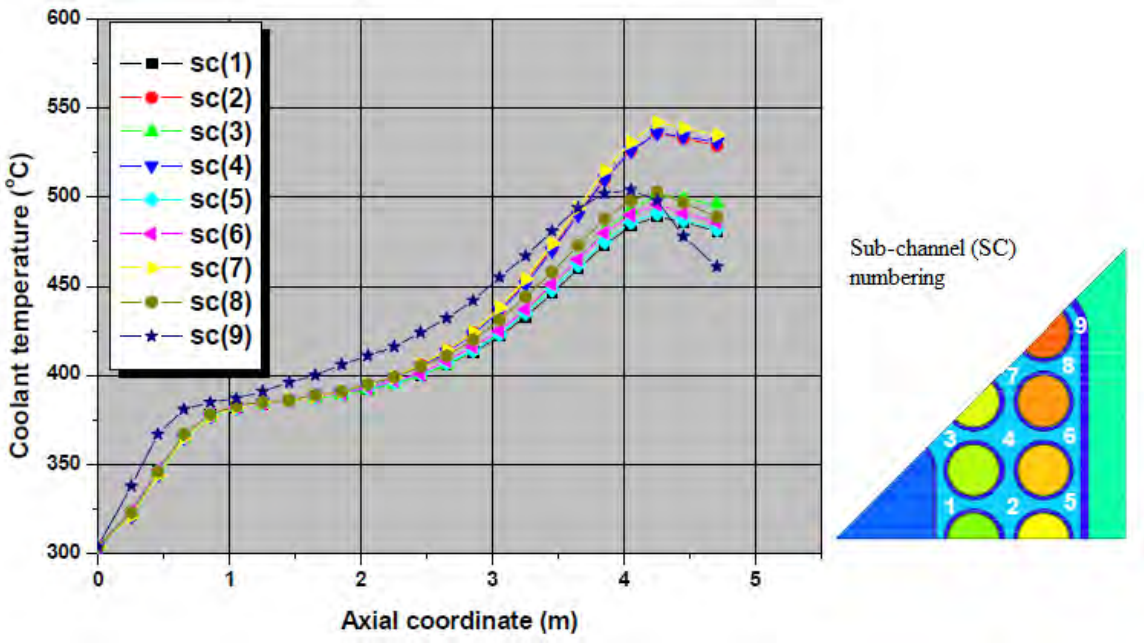

Figure 2.8: Coolant profiles of a coupled neutronic/thermal hydraulic analysis [19].

2.3 Experimental Studies conducted so far

Studies on the characteristics heat transfer in the 2 × 2 fuel rod bundle with and without the wire-wrapped spacers have been conducted by CNL in collaboration with Xi'an Jiaotong University. Gu et al., [29] observed that the wall temperature in the circumference was not uniformly distributed in the heated rods. This was attributed to the wall temperatures dependence on the flow conditions. The heat transfer enhancement observed in the fuel bundle was however, relatively small. Examinations of the effect of spacer configuration on heat transfer has been investigated in a three-rod bundle using carbon dioxide at supercritical pressures as coolant.

Generally, the difference in wall temperatures between grid spacers and wire-wrapped spacers is minimal. However, the wall temperature variation at several points of the heated

rod for the wire-wrapped spacer is smaller than that of the grid spacers at subcritical temperature region. This is due to the improved mixing of the coolant between sub-channels of the wire-wrapped spacer. Hence, the flow and enthalpy imbalances are reduced. Another observation made was on the occurrence of localized HTE at the grid spacer locations but decayed over a short distance from the spacer.

2.4 The two Main types of SCWR concepts

Basically, SCWR concept can be classified into two types, pressure vessel type and a pressure tube type, the reactor core for these designs can either have a fast or thermal neutron spectrum. Even though the thermal spectrum type has a low density of superheated steam an additional water as moderator is required. This water is supplied via water rod inside the fuel bundles and in the gaps between the fuel rod bundles [30]. Furthermore, SCWR can also be classified in terms of the flow pattern, as illustrated in Figure 2.9 (a) a single pass design with a single heat-up process similar that of the conventional nuclear reactors. A two-pass design (Figure 2.9 (b)) in which the coolant flow is downward utilizes the two-step process in the peripheries of the core region to reduce the coolant peak temperature inside the core. This is accompanied by an ideal mixing of the coolant in the lower plenum of the core and a second heat-up in the inner core region. Oka et al. [31] applied such a technology in their superlight water reactor concept. However, as for a three-pass core design (Figure 2.9 (c)), better coolant mixing to eliminate hot streaks between each step is achieved with the evaporator being the first heat-up in the inner region of the core, encircled with a first super-heater with downward flow and a second super-heater with upward flow [30].

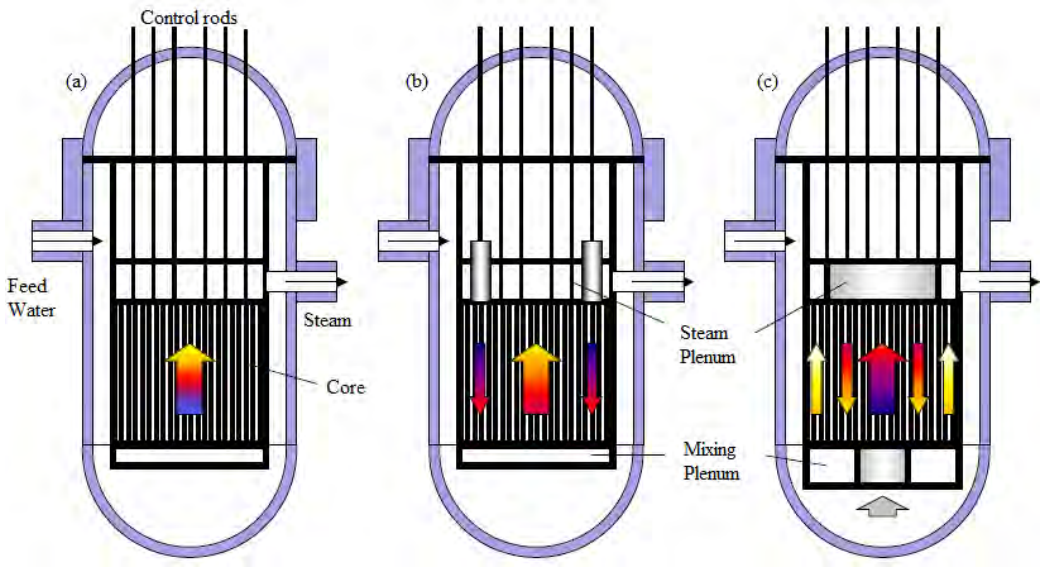

Figure 2.9: SCWR core design with different options for heating-up steps. (a) One-pass design, (b) Two-pass design, and (c) Three-pass design. [32]

More heat-up steps increase the complexity of the core design. This means that the fuel assemblies in the clusters depending on how they are welded to the upper plenum, will be difficult to reshuffle and replace during the scheduled time of 1 year. Consequently, the coolant temperature peak will decrease at a predicted average outlet temperature of the core.

2.4.1 Pressure Vessel Concept

A design concept of a PV-type with a thermal neutron referred to as High Performance Light Water Reactor (HPWR) has been worked on by a consortium comprising of twelve organizations from eight countries in Europe from 2006-2010 [6]. The core of this reactor is designed to be cooled and moderated with SCW at 25 MPa while the exit temperature has been set at 500 ˚C. Design features coupled with the design concept analyses has been summarized by Schulengberg and Starflinger [32]. This reactor is designed to be operated

at a thermal power equal to 2300 MW, with an overall efficiency of 43% of the steam cycle which in turn translates into a net value of electric power equal to 1000 MW. With 500 ˚C as a target exit temperature of coolant, the superheated steam is insulated thermally from the RPV, maintaining it below 350 ˚C. Figure 2.10 displays a three pass core.

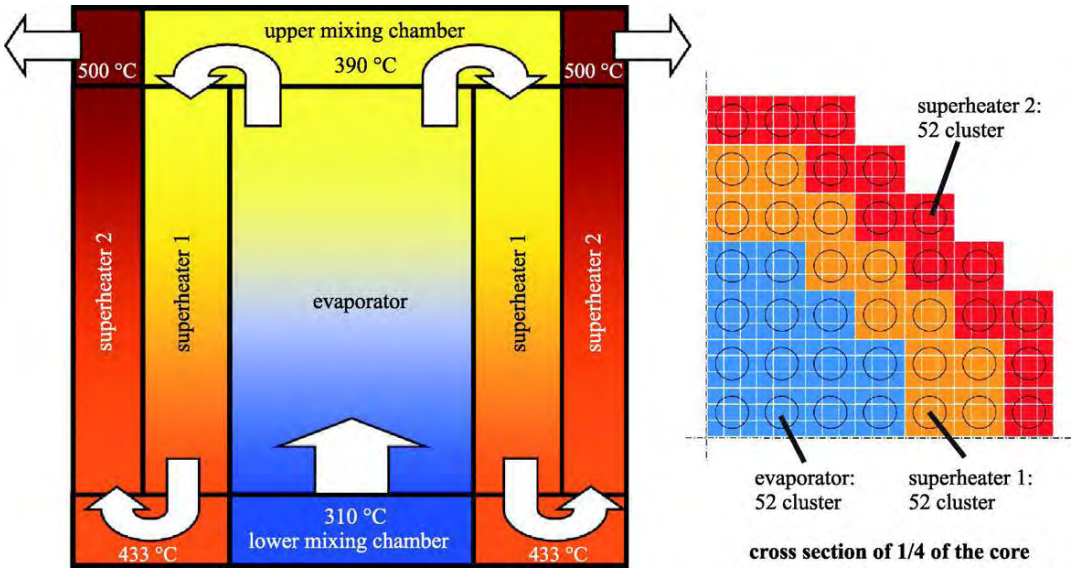

Figure 2.10: Pressure vessel type of the HPLWR with a three-pass core

[21]

The three-pass flow regime is applied in the HPLWR core design concept (Figure 2.8 (c) and Figure 2.10), and the peak coolant temperature is maintained below 600 ˚C via the mixing mechanisms in both the upper and lower plena of the core. The CRs are introduced from the top similar to that of the PWR, while guide tubes are used for the control rod alignment in the top half of the RPV. The fuel rod bundles of the reactor core are erected on the thick core support plate of the core barrel, suspended in the reactor flange. The steam plenum along with the mixing plenum are flexible in design, and ease the fuel reshuffling and replacement that is conducted on a yearly basis. They can also be removed without difficulties after extracting steam from the hot steam pipes. In an event where the line

supplying feed water breaks, the resultant coolant loss has been addressed and minimized by the four back limiters that supplies feed water to the RPV. The top half of the RPV is being purged by half of the feed water supplied, this water which is inside of the water channels of the fuel bundles (flows through the gaps between the assembly boxes) serves as moderator water. Subsequently, water serving as moderator is mixed with the feed water residual underneath the lower mixing plenum of the core immediately after cooling the radial core reflector. The orifices in the lower mixing plenum are used to adjust the mass flow split.

2.4.2 Pressure tube concept

As indicated by Yetisir et al. [33], the evolution of Canadian SCWR emanated from the well-established PT-type CANDU reactor. The adopted thermodynamic cycle of the Canadian SCWR is similar to that of the improved and latest turbine configuration of the fossil power plants currently in operation and using supercritical water. The moisture steam separator (MSR) between the intermediate pressure (IP) and low pressure (LP) turbines is included in the adopted cycle. The function of the MSR is to separate moisture from the steam and to reheat the steam to ensure that the moisture content is within the acceptable amounts at the low pressure turbine outlet. Four LP condensate heaters are included in the cycle along with a deaerator and four HP feed-water heaters.

According to this design, SCW at high-pressure is directly fed into the SCW turbines. Similarly, the conventional BWRs also uses this adopted direct cycle at lower pressures and temperatures [7]. However, the implementation of high temperatures and pressures is facilitated by the cycle being direct. This in turn leads to the simplification of the system and elimination of steam generator and its associated components useful for the energy

transfer. The thermodynamic cycle of the Canadian SCWR is designed for high-pressure turbines operating at a pressure of 25 MPa and temperature of 625 ˚C. Feed water enters the core at a temperature of 315 ˚C and a mass flow rate of about 1,176 kg/s while thermal power is about 2540 MWth. The calculated gross value of 1,255 MWe as electrical output, gives 49.4% as the gross thermal efficiency of the reactor [30].

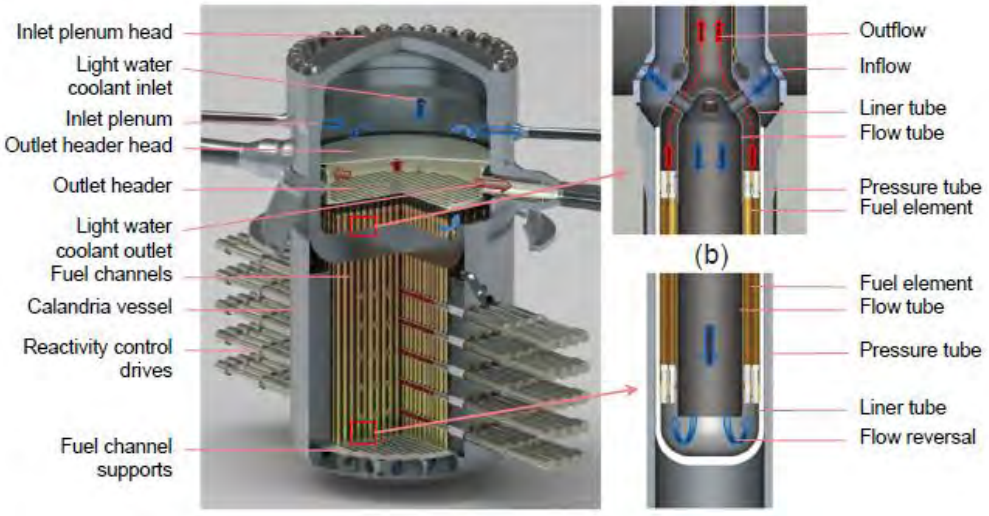

Figure 2.11: Canadian SCWR core concept.

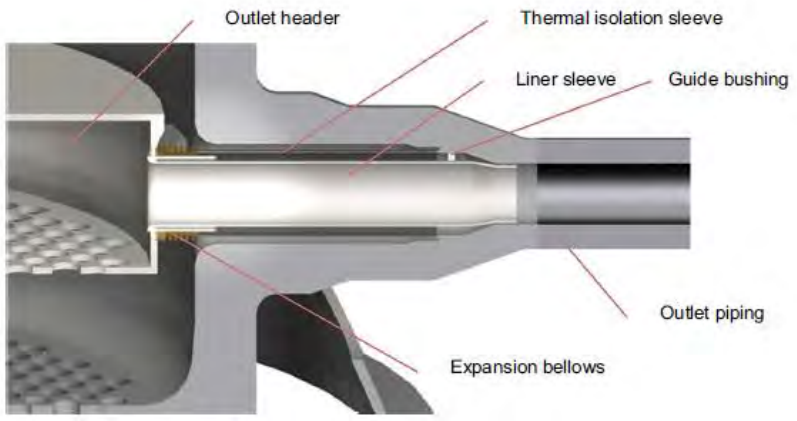

Figure 2.12: View of the cutaway outlet sleeves

Figure 2.11 shows the Canadian SCWR core concept which comprises of 336 fuel channels attached to a common outlet header, a pressurized inlet plenum, and an LP calandria vessel containing heavy water as moderator. As a safety measure, the adoption of counter flow in the fuel channel is to completely avoid a coolant loss in the reactor in case of an entire break of either the pipe inlet or outlet. In a bid to increase the moderation of the neutrons near the inside of the rings of the fuel rods a central flow passage without fuel is introduced at the center. Nevertheless, radial power is uniformly distributed across the fuel channel and throughout the burn-up cycle a desirable negative coolant void reactivity due to central flow channel feature is achieved. The coolant supplied in this case flows through the inlet plenum, close to the outer part of the header outlet (blue arrows in Figure 2.11), then flows subsequently into the extension of the PT via a series of slots, and finally into the fuel rod bundle via a crossover piece (a). Then again flows via (a) downwards central tube of the bundle, then flows backwards up via the fuel pins (b), and finally leaves through the header outlet.

Even though the inlet plenum is classified as a pressure vessel, its constituents are not bound by high neutron fields; thus, damage in relation to irradiation is not a major concern. Owing to the operating temperature of approximately 315 ˚C, the following material composition of SA 508 grade 4N, 3-4 wt% nickel of a pressure-vessel steel has been selected. In addition, the internal surface of the vessel may be coated with stainless steel (308 or 309) further corrosion inhibition. While Alloy 800H (Fe-Ni-Cr alloy) has been selected as the material for the head and outlet header because of an excellent demonstration of the following properties, corrosion resistance, strength and toughness at high temperatures.

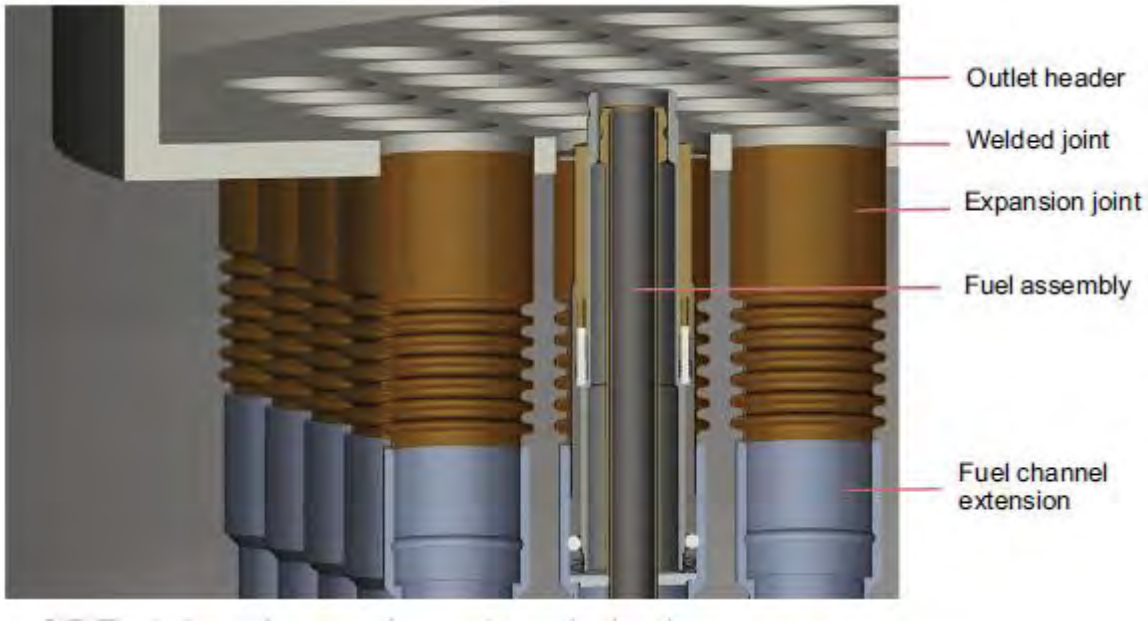

Figure 2.13: Connection of a fuel channel to the outlet header.

Owing to the pressure difference conditions being low at the inlet through to the outlet, the possible generation of stresses or forces is low; hence the design requirements are comparatively light. Isolation of the sleeve as illustrated in the Figure 2.12 by utilizing thermal flexibility is used to decouple the outlet sleeves from the plenum inlet. The fuel channel made up of a pressure tube that extends into the moderator and an extension that connects the pressure tube to the outlet header (see Figure 2.13). The bellows expansion joint eases the differential movement between the outlet header and the channel. This flexibility in the design configuration eases the replacement of a single channel, if need be. Nevertheless, due to the low absorption of neutrons heavy water has been chosen over light water as moderator at low pressures. Additional moderator around the core is included to act as a shield and neutron reflector. The location of the tube sheet of the inlet plenum is at 0.75 m on the top part of the core, ensuring the plenum material is protected from damage by radiation. The reactivity control mechanisms strategically positioned on the sides of the

core are shielded, at a minimum, with an equivalent amount of moderator water and increasing amount at the reactor centerline as a result of the curvature of the calandria vessel. A recirculation pumping system is used to pump the moderator water which operates at subcooled temperature conditions, however in case of power failure at a station, a flashing-driven natural circulation loop is used to passively remove core decay heat. The location of the inlet and outlet nozzles for these safety systems are just above the core, this is to ensure that the calandria does not drain due to a pipe break.

2.5 Fuel assembly concept

The density of the coolant decreases to less than 200 kg/m^3 above 390 ˚C, hardly enough for the production of a thermal neutron continuum. Consequently, a moderator required for a thermal neutron continuum, can either be supplied as feed water flowing through moderator boxes within the fuel assemblies and also between the gaps of the assembly boxes or separately as heavy water in case of a PT-type concept [30].

2.5.1 Fuel assembly concept for a HPLWR

The fuel assemblies in a typical HPLWR concept are designed with a central moderator box surrounded by 40 fuel rods arrayed into two rows. This design arrangement provides also a substantial small thickness of the walls of both the assembly and moderator boxes, as illustrated in Figure 2.14. Based on the recommendations made by Schulenberg and Starflinger [32], nine assemblies have been grouped into a cluster having common head and foot pieces, as displayed in Figure 2.15. The dimensions of the fuel pins are 8 mm as outer diameter with a wall thickness of 0.5 mm and 1.18 as P/D. A wire-wrap having a thickness of 1.44 mm around each individual rod serves as a spacer grid and also as an

effective mixing device. To minimize the heat-up of the moderator water in the fuel assemblies, a thermal insulation between two sheets made of stainless steel is inserted between the moderator box and assembly box. Control rods, packed with boron carbide, are introduced inside five of the nine inner boxes of a cluster [30].

The heated (active) length of the fuel assembly is 4.2 m. To minimize the increase in pressure during burn-up, a fission gas plenum of length 0.5 m is used on top of the fuel pellets. The windows in the head piece of the fuel assembly cluster are designed to discharge and supply steam to the steam plenum. The C-rings are used to seal windows against any ingress of moderator water into the generated steam.

For a 3-pass reactor developed to generate 2300 MW as its thermal power, comprises of 52 clusters of fuel assemblies which makes up an evaporator in which the coolant flows upwards. The evaporator is surrounded by 52 clusters which serve as the first superheater with a downward flow of coolant in them [30]. The power density is relatively low in the 52 clusters (serving as the second superheater) located at the periphery of the core, thereby maintaining temperature of the cladding surfaces below 650 ˚C. The computed average power density of the core in HPLWR is analogous to that of the BWR, and the evaporator has a power density of about 100 MW/m^3, similar with that of a PWR [30].

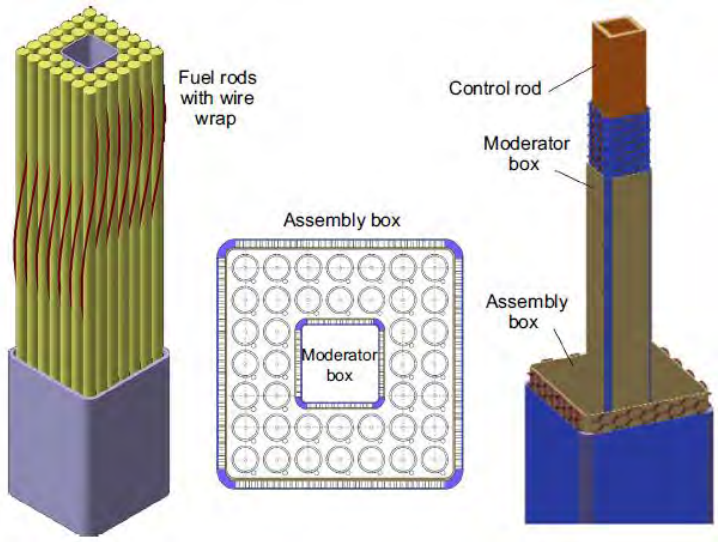

Figure 2.14: A typical Fuel assembly design of the HPLWR.

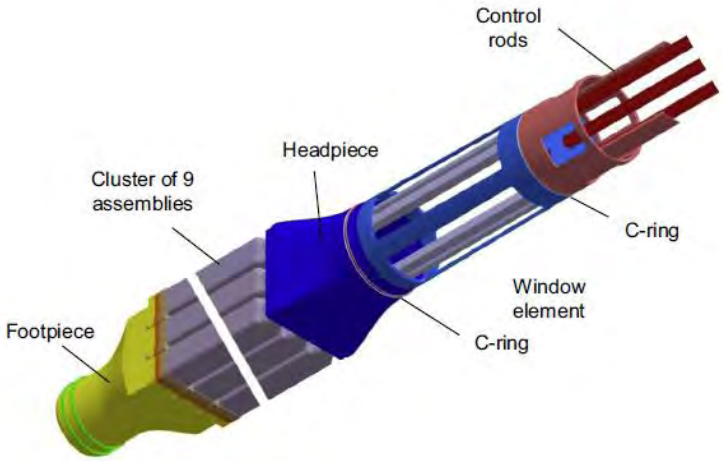

Figure 2.15: Cluster design of the HPLWR assembly comprising of Foot piece, head piece; CRs inserted in 5 moderator boxes from the top. [25].

Replacement of the fresh fuel assembly cluster in the evaporator and reshuffling of fuel assembly clusters from the peripheries of the core into the central part is scheduled to take place once in a year, “mainly from the evaporator then to the first superheater and from

there to the second superheater". Four rods per fuel assembly consisting of a mixture of fuel and gadolinia pellets are used at the beginning of each burn-up cycle [30]. Accordingly, boric acid, is not used in SCWR due to a drastic change of its solubility issue in SCW immediately after the coolant reaches pseudocritical region (384.9˚C at 25 MPa). However, the only second safety alternative or option proposed to be used in emergency situations (i.e. emergency shut-down mechanism) is the injection of boric acid [30].

2.5.2 Fuel assembly concept in the Canadian SCWR

The fuel proposed to be used in the Canadian SCWR concept is analogous to the current conventional CANDU reactor, in that the produced heat from the ceramic pellets is transferred via the metallic cladding to the primary coolant [30].

The fuel assembly is comprised of the fuel rods, flow tube centrally located, encapsulated insulator, top and down part supports of the fuel rods, flow exchanger of the inlet/outlet, and exit flow tube. Figure 2.16 illustrates the cross sectional arrangement. Inlet plenum is used to transfer the coolant at the inlet to the fuel assembly initially runs through the outer parts of the assembly design [30]. A flow exchanger on top of the fuel elements and support of the upper fuel element, is used to transfer the coolant entering through the inlet to the flow tube which is centrally located. The outlet coolant is transferred from the outwards of the FA to the outlet flow tube where it proceeds to the outlet header using the same flow. The Inlet coolant flow according to the design is downwards through the "central flow tube" to the lower part of the fuel rod bundle. The direction of the coolant is reversed at the bottom of the FA and flows upwards in the periphery of the FA over the fuel elements to the flow exchanger-outlet flow tube. The FA concept comprises two rings (inner and outer), each having 32 fuel elements in ring and 64 fuel rods in total (see Figure 2.17 for

the “cross-sectional view”). The dimensions of an individual fuel element are as follows, 9.5 mm as the outer diameter for the inner ring and 10 mm for the fuel elements in the outer ring. Each individual fuel element has a total length of 6.5 m, in which the fuel pellets are housed, the inner filler tube located within the plenum area prevents the element from collapsing due to external pressure, while the spring holds the fuel pellets in place but allows the pellet to expand. The fuel element has an active length of 5 m. The two ends of the element are closed with and end plug, which is welded to the cladding tube. The wire wrap in spiral arrangement is used as a spacer between fuel rods, inner-ring elements and the flow tube in the centre, also to maintain the spacing between outer-ring elements and the inner insulator liner. Furthermore, to keep on maintaining the gaps, these wires relatively reduce the vibration of each rod and improves heat transfer from the cladding wall to the coolant. Experimental investigations conducted so far using tubes, annuli, and bundles, have shown the efficacy of wire-wrapped spacers on improved or enhanced heat transfer. Fretting caused by wire-wrapped spacers on the fuel cladding has been identified as one of the concerns. Taking into account the flow which is relatively low in the channel, fretting may not be an issue, as anticipated. However, an experiment is required in this instance to confirm this phenomena. [30].

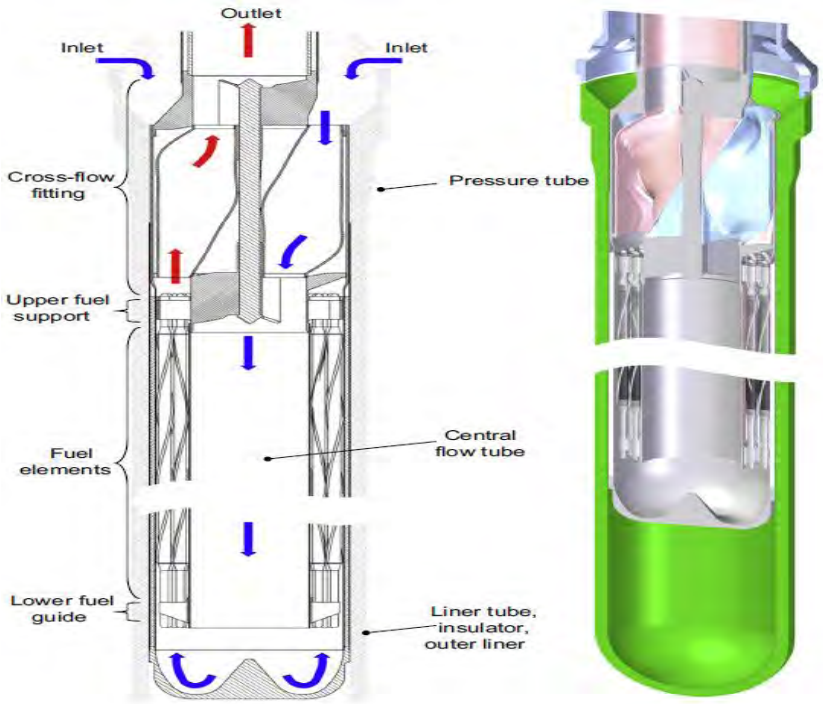

Figure 2.16: SCWR fuel assembly Cross-sectional views

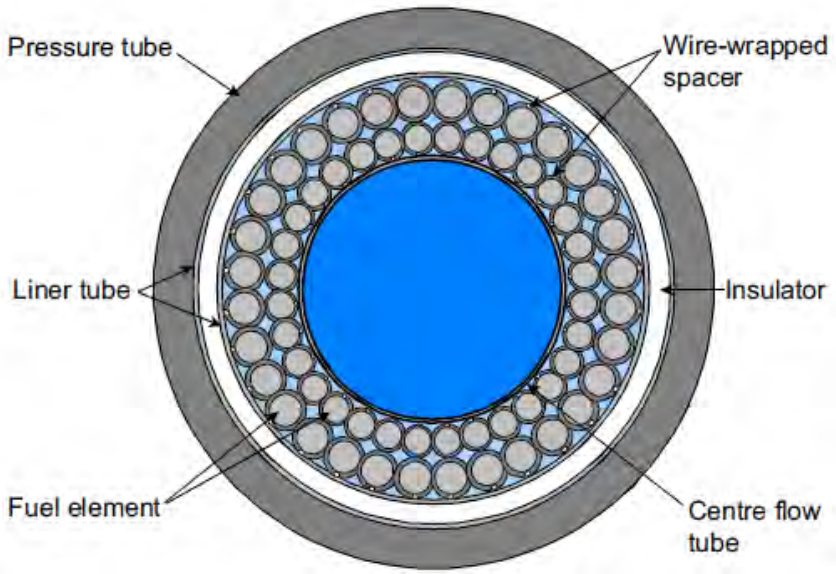

Figure 2.17: A 64-element fuel assembly cross-sectional view inside of the

of a PT-type concept

2.5.3 Fuel assembly concept of a Fast reactor (FR)

The fuel assembly design appears to be simpler and flexible for a core of a reactor having a spectrum with fast neutrons. The fissile plutonium contained in the seed assemblies of hexagonal fuel assembly design type proposed by Oka et al. [31], is nearly 25%, and is dependent on the size of the core, mixed with the blanket fuel assemblies with pure 238U in a non-uniform configuration. The flow of the coolant can either be downward or upward, and this is dependent on the headpiece, in which windows may not be included in the design towards the steam plenum on top of the core. According to Figure 2.18, the concept may be characterized by a design of either a two-pass or one-pass having a flow path that is flexible. The fingers of the control rod are introduced from the top to the inner parts of thimble tubes similar to that of a PWR.

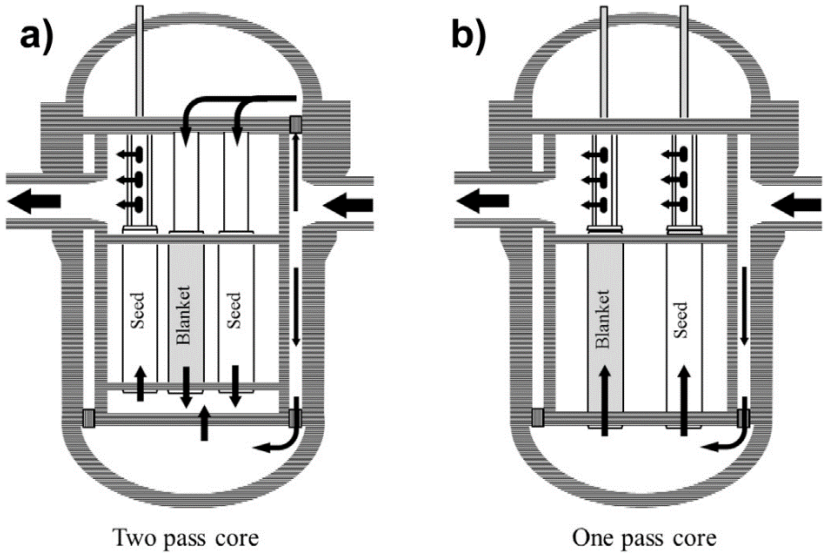

Figure 2.18: Alternative flow patterns for Super-Fast Reactor, a) two pass core, b) one pass core

The cladding material of the fuel elements in the fuel assemblies of FR is made of stainless steel and each individual rod has a design outer diameter of 7 mm and 8.12 mm as the

pitch. Accordingly, a mean power density of 158 MW/m^3 of the core which is "high" is facilitated by this tight hexagonal arrangement. For having a thermal power of the core of 1 650-MW along an active height of 3 m, 126 seed assemblies and 73 blanket assemblies would be needed.

A rise in the reactivity of the core with a decrease in the density of the coolant for a fast neutron spectrum has been identified as one of the general problem of such a FR concept. This problem can be addressed by keeping the local void reactivity and adding a moderator which is solid throughout the full burn-up cycle, in this instance zirconium hydride (ZrH) as well as stainless steel is used to surround the blanket fuel assemblies, which increases the leakage of neutrons and in turn softens the spectrum. Figure 2.19 presents this concept. However, the drawback of this concept, is that more plutonium is consumed in this reactor as compared to the degree of breeding, which may not be ideal for the sustainability of nuclear energy concept.

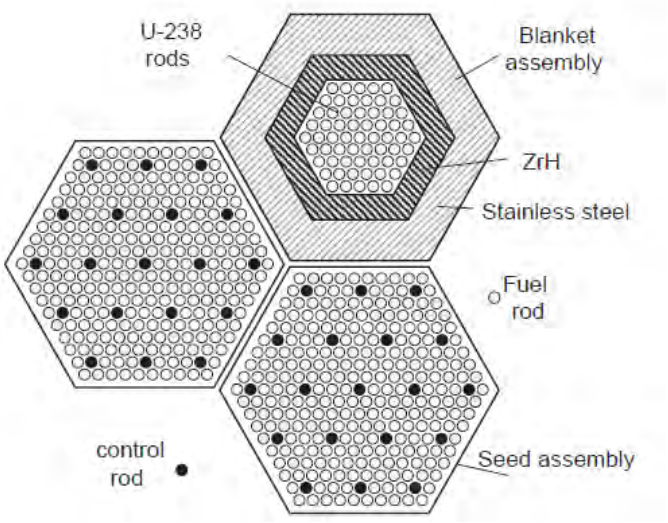

Figure 2.19: Design of a fast reactor core FA with fast neutron spectrum [29].

2.6 The SCWR safety system concept

Defense-in-depth is defined as a safety philosophy that guides the design, construction, inspection, operation, and regulation of all nuclear facilities. In these advanced light water reactors is taken into consideration and applied to mitigate any possible form of accident. Thus, the following save the power plant operation measures shall be ensured to [30]:

Operating systems shall be used as safeguards during normal operation. Additionally, the basis of a power plant will be on

- conservative design coupled with high availability and reliability and
- Verified and tested technology and quality assurance.

Operating occurrences of rare events ($<10^{-2}$/year) shall be controlled and limited by

- Inherent safety and nuclear stability and
- Monitoring and diagnostics

The following enlisted safety systems shall be employed to control and possibly avert accidents within the design basis having a probability of $<10^{-5}$/year, these include

- “redundancy and train separation”,
- “protection against internal and external hazards”,
- “qualification against accident conditions”,
- “Automation”, plus
- “Autarchy of the safety systems”.

Several failure scenarios (e.g., LOCA, station blackout, and total loss of water) and severe external events (e.g., military invasion due to war or large commercial aero plane crash) have been accounted for in the safety design of extension events which must be safe guarded by

- Diversity of systems and
- Able to withstand the occurrence of any external loads.

If accidents that are severe should still occur, the protection of supercritical water reactor will be effected by

- features mitigation and
- Preventing the early premature severe damage of the containment due to energetic consequences emanating from (eg, direct heating of the containment, the explosion of steam and the detonation of global hydrogen).

2.6.1 Safety systems implemented in a PV-type SCWR concept

Enlisted below are some of the common requirements in terms of safety for the design of a PV-type supercritical water reactor, which have been taken from LWR designs (BWR or PWR) with little modifications [34, 30]:

- limiting the steam pressure using the pressure relief valves
- the shut-down system of a reactor in which CRs are used or boron is injected as a second alternative, “divers shut-down system”,
- automated depressurization system of the steam lines into a pool inside of the containment via the spargers to close the coolant loop inside the containment in an event of the isolation of the containment
- containment isolation by both active and passive isolation valves in each individual line penetrating through the containment to close the third barrier in case of an accident,
- A residual heat removal system for long-term cooling of the containment.

Figure 2.20 shows a typical example of a HPLWR containment safety system which is compact in design with inner diameter and height of 20 m and 23.5 m respectively [32]. The containment which is cylindrical shaped from pre-stressed concrete is able to with stand 0.5 MPa internal pressure according to the design. It comprises of the RPV, a suppression annular pressure pool with 900 m^3 of water and 500 m^3 of nitrogen, four upper pools with a total water volume of 1121 m^3, and a drywell gas volume of 2131 m^3. Four feed-water lines with check valves and four steam lines with containment isolation valves, each inside and outside of the containment, connect the reactor with the steam cycle. These valves are designed with a stroke time of 3 s, actively and passively closing. Four automatic depressurization systems (ADSs), each equipped with two safety relief valves and two depressurization valves, open a flow cross section of 110 cm^2 each to eight spargers in the upper pools [30].

Below the pressure suppression pool, four extra components not strictly necessary for functioning and separate low pressure coolant injection pumps, having an exit pressure of no less than 6 MPa with a maximum flow rate of 180 kg/s each, supplying coolant from the pressure suppression pool through a mechanism of heat exchange for residual heat extraction and through a check valve to the feed-water line. The coolant loop in the containment is closed by overflow pipes from the top part of the pressure suppression pool. The drywell is connected to the pressure suppression pool by sixteen vent tubes in the containment [30]. Four emergency condensers are connected with the four steam lines and feed-water lines hanging from the top in the upper pools.

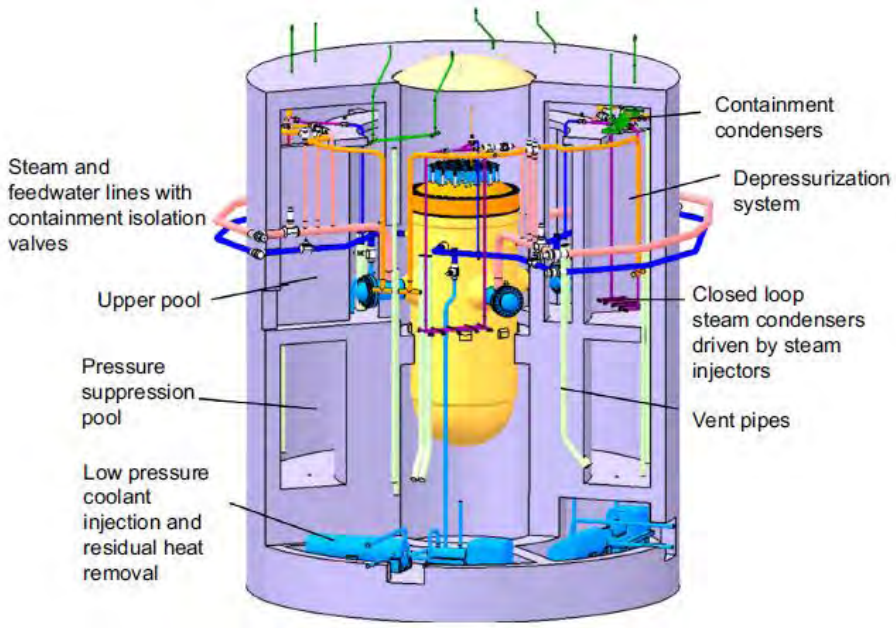

Figure 2.20: HPLWR containment and safety system [22]

Furthermore, the four containment condensers mounted at the drywell of the ceiling, are joined to pools above the containment on their secondary side. To facilitate the condensation of the steam once the saturation temperature has been attained in the pools and as the pressure of the containment starts to rise their secondary side has been opened permanently, in the unlikely instance where the "heat sink of the residual heat removal system" is unavailable. Open connecting pipes from the ceiling to the pressure suppression pools enable a discharge of hydrogen from the drywell. In turn, the pressure suppression pool can be vented to the stack through aerosol and iodine filters". The lines of the feed-water together with the two pumps are connected to the boron poisoning injection system with a10 m^3 tank containing 20-25% concentration of B-10 located outside on the top part of the containment. This serves as an additional safety feature in shutting down the system [34].

2.6.2 Safety systems envisaged in a PT-type SCWR concept

The safety systems adopted in Canada's supercritical water reactor concept is that of more advanced heavy water reactors which incorporate multiple levels of independent and different safety systems used to improve the reliability by strengthening defense-in-depth and passive safety systems. The enhancement of safety to significantly prevent the damage of core and mitigate the releases of radioactive materials into the environment is one of the key developmental goals of Canada's SCWR concept.

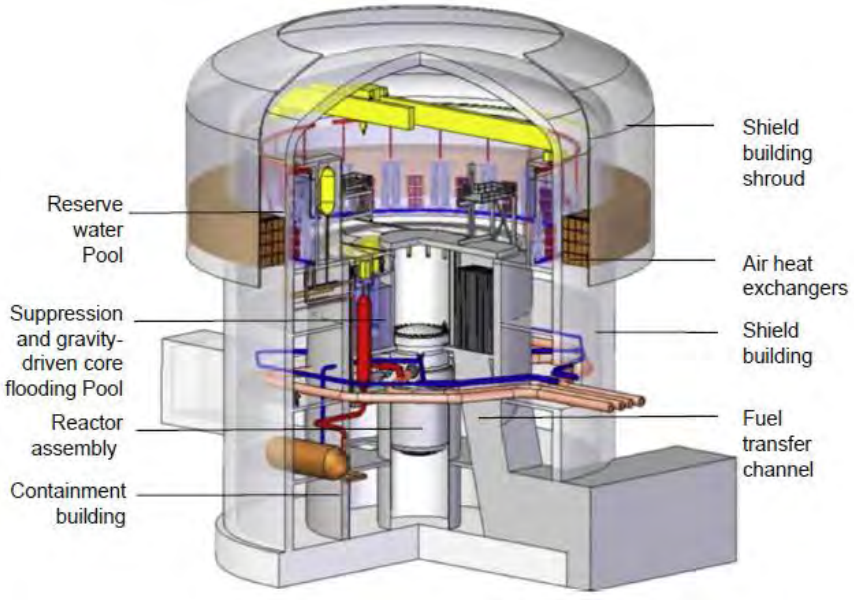

Figure 2.21: The Canadian safety system concept

Moreover, there is a transformative enhancement in the risk of core damage by the inclusion of additional passive decay heat removal passageway in emergency situations. This ability is possible through a combination of a natural circulation-driven moderator cooling system, the fuel rod assembly and fuel channel concepts, and the transfer of direct radiation heat from the fuel to the insulator liner. The safety concept that has been adopted for Canada's supercritical water reactor concept is described by Novog et al. [35], and

Yetisir et al. [33] and Gaudet et al. [36] gives a detailed description safety system designs. Figure 2.21 displays the inside part safety system features of the reactor building. More details of safety systems can be found in report prepared by Schulengberg and Leung [30].

2.7 STAR-CCM+ Simulation

2.7.1 Background

STAR-CCM+ is a mathematical idealization (representation) of real materials such as solids, fluids and gases. Continuum mechanics is concerned with the behaviour of such representations. It is based on laws of conservation of mass, energy, momentum, moment of momentum and entropy, and is aided by a mathematical apparatus specifically developed for it [37].

2.7.2 Principle of Operation

STAR-CCM+ is based on numerical solution of equations governing fluid flow by the finite volume method. This entails transforming the governing equations into a system of non-linear algebraic equations, whose subsets approximate each conservation equation [37]. Time, space and equations relating values of dependent variables are treated as basic unknowns at a finite number of locations (grid-points) in the calculation domain. Continuous information contained in the exact solution of differential equations is replaced with discrete values for the distribution of dependent variables. This process is called discretization and the algebraic equations involving unknown values of the dependent variables at each grid point are referred to as discretization equations.

Time discretization entails subdivision of a given time interval into a number of smaller subintervals or time steps. Space discretization consists of defining a numerical mesh

consisting of a finite number of computational points, thus replacing the continuous functions by their values at those points. Replacement of individual terms in the governing equations by algebraic expressions connecting nodal values on a numerical mesh is called equation discretization [37]. An illustration of the discretization process is shown in the diagram (Figure 2.22).

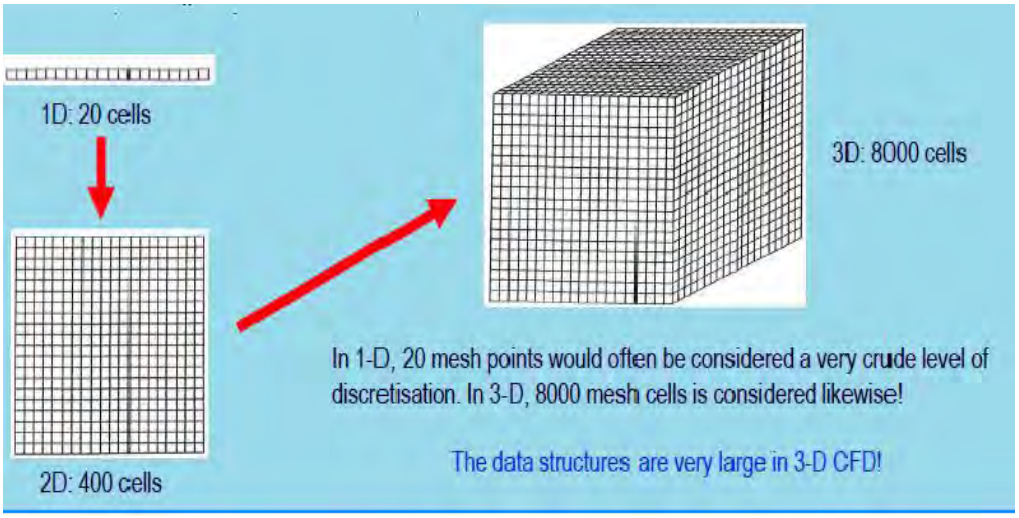

Figure 2.22: Illustration of the finite volume method [36]

STAR-CCM+ is inherently a computational fluid dynamics (CFD) code and hence it comprises three main elements: (i) a pre-processor, (ii) a solver and (iii) a post-processor. Pre-processing entails defining the problem, geometry generation with the aid of inbuilt geometry modeller together with facilities for importation of external computer aided design (CAD) models, mesh generation and physics set-up.

Solvers are mathematical software libraries that take the generic form of the problem and calculate the solution. A discretized version of the transport equations is solved for each cell in a mesh when the solver is run. Velocity and pressure solvers apply the Semi

Implicit Method for Pressure Linked Equations (SIMPLE) algorithm. The discretized continuity equation takes the form of a pressure correction equation and estimated values of its solution are placed at all grid points in a mesh. Tentative values of the coefficients in the discretization equation are then calculated and the equation is discretized into a set of linear algebraic equations. The equations are solved to get the new values of velocity and pressure which are reused to calculate values of the coefficients of the discretization equation. The process is repeated until further repetitions (iterations) cease to produce any significant changes in the values of velocity and pressure. The final unchanging state is called the convergence of the iterations [38]

Energy solvers compute the conservation of energy within each control volume or cell in the mesh. The solver similarly proceeds from an initial guess of the energy distribution in each cell and performs a series of iteration to obtain a converged solution of discretized algebraic equations for the transport and distribution of energy in the domain. The κ-ε turbulent solver computes the solution of transport equations for two scalar properties of the turbulence. It solves κ equation which is a model for the turbulent kinetic energy and the ε-equation which is a model for the dissipation rate of turbulent kinetic energy in the domain. The solution of two convective transport equations namely the specific dissipation rate (ω) and turbulent kinetic energy (κ) in the computational domain is computed by the κ- ω solver.

Data generated by the solver is post processed using various data visualization tools. The Plots node, which has a pop-up menu, is the object manager for all monitor plots and XY plots that have been created in the simulation. It exists even when empty to allow creation of the first plot, but will typically contain a residuals plot, which is created automatically

once you start iterating. The plotting features in STAR-CCM+ allow you to create three kinds of two-dimensional plots:

- **Monitor plots**

Are useful in tracking the solution of the simulation and ensuring that it is converging within each time step. Normally, monitor plots are used to display various types of selected quantities to keep track of the convergence of the solution. Residual plots represent the degree at which the discretized equation is satisfied in each cell. When the solver is run, a discretized version of the transport equations is solved for each cell in the mesh. Residual monitors keep a good track record of this global quantity for each of the transport equations solved in the continua within the simulation. The residual plot is a monitor plot that is automatically created from the active residual monitors on semi-log axes when iterating starts. All active residuals are displayed in the residual plot by default.

- **XY plots**

Based on the solution data from the simulation and/or simulation data.

- **Histogram plots**

Display data typically for particles [39].

2.8 Heat transfer coefficient with wall temperature computed by Wataa.

Wataa [17] used the Bishop correlation [40], to compute and predict the heat transfer correlation which in turn was used to evaluate the wall temperatures in each individual sub-channel. The highest and maximum HTC value evaluated was 65 kW/m^2 obtained in SC

(2), SC (4) and SC (7), as displayed in Figure 2.23 (these sub-channels have also been presented in Figure 2.4). However the maximum peak was first reached in SC (9).

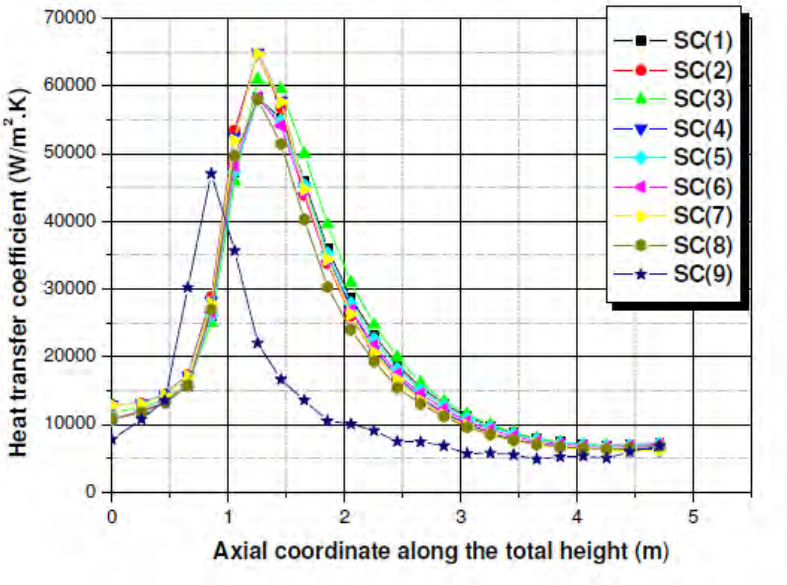

Figure 2.23: Heat transfer coefficients profiles in each SC [17]

The evaluated HTC values in each individual sub-channel were then used to obtain the wall temperatures. The evaluated wall temperatures were found to be within the allowable limit of the design criteria of 620 °C, set for the wall surface temperature of the cladding [17]. The temperature profiles are presented in Figure 2.24.

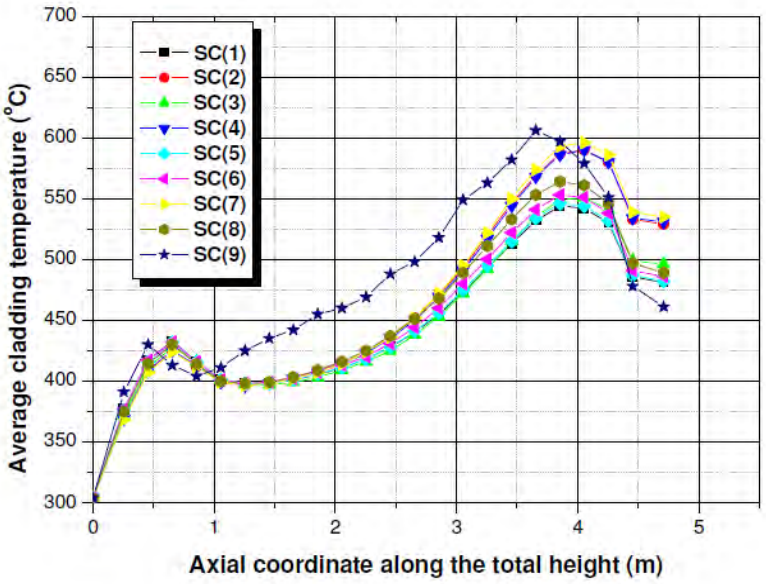

Figure 2.24: Wall temperature profiles in each individual sub-channel [17]

CHAPTER THREE : METHODOLOGY

This chapter gives a detailed insight on the methodology adopted to obtain numerical results in the study of heat transfer performance of the proposed fuel assembly of a SCWR.

3.1 Numerical Data

The numerical data used by Wataa [17] was implemented as input data for modelling 1/8th FA in the STAR-CCM+ code. The fuel rod diameter of 8 mm, P/D ratio of 1.15 and 4.2 m as active height of the heated section of the fuel assembly. The detailed dimensions considered in this present work are presented in Table 3.1. A uniform heat flux of 650 kW/m^2 in the fuel rods was implemented in the code [17]. The feed water temperature to the reactor pressure vessel was set at 280 °C and a total mass flow rate of 0.167 kg/s (601.2 kg/h). Inlet coolant temperature to the fuel assembly was set at 300 °C and in the sub-channels, the distribution was aimed at an average outlet temperature of 500-550 ˚C of this assembly. The in depth details concerning numerical data can be found in Wataa's research work [17]. The water properties from NIST Table [41] was used to calculate physical properties of water applied for the SCW used in this analysis as a coolant. Some of the tools used are presented in Appendix C. The supercritical water is mainly characterized with physical property variations, and this must be cautiously taken into account when solving transport equations of continuity involving mass, momentum and energy.

The obtained SC "(sub-channel)" coolant temperatures by Wataa were used to compare with the ones simulated using the STAR CCM+ code.

3.2 CFD Model Description

3D-CAD a feature-based parametric modeler within STAR-CCM+ was used to generate the one-eighth geometry. Extruding and cutting operations were then executed on the created geometry. Parts and regions were subsequently assigned to the geometry for integration with meshing and simulation process. In this analysis, dimensions used of the model (in mm) were obtained from an extract of the square fuel assembly configuration design proposed by Hofmeister et al., [16] as illustrated in Figure 3.1.

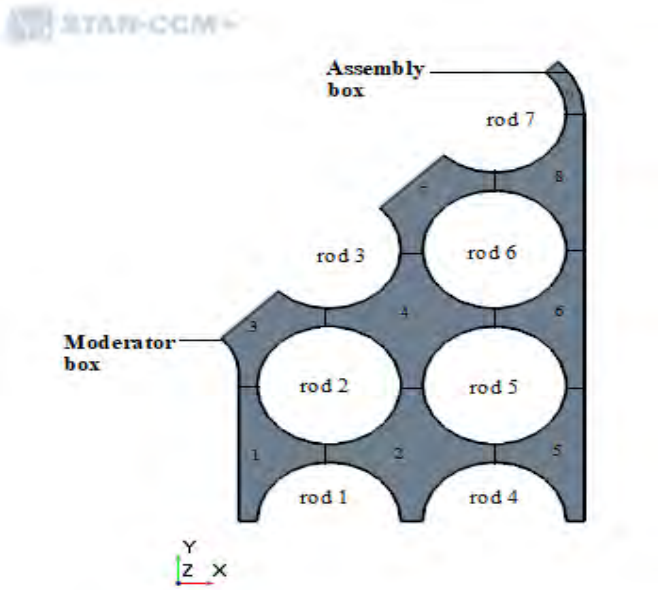

Figure 3.1: A numbering representation of Fuel rods and sub-channels in "1/8 assembly type sq 2.1"created using STAR CCM+ CAD

The fuel assembly "sq. 2.1" comprises of 40 fuel elements, an assembly box having an outer and inner side lengths of 67.2 mm and 65.2 mm respectively. Also a single moderator box having an outer and inner lateral lengths of 26.8 mm and 26.2 mm in the centre.

Detailed dimensions of the 1/8th fuel assembly implemented in STAR CCM + CAD are presented in Table 3.1.

Table 3.1: Dimensions used for creating a 1/8th FA geometry

Square "2.1"Assembly type	Values
Number of moderator boxes per assembly (–)	1
Cladding outer diameter	8 mm
P/D	9.2
Number of fuel rods (–)	40
Active axial heated height	4.2 m
Fuel assembly box	
Length of the inner side	65.2 mm
Thickness of wall	1 mm
Length of the outer side	67.2 mm
Moderator box	
Length of the outer side	26.8 mm
Thickness of wall	0.3 mm
Length of the inner side	26.2 mm

To reduce the computation time and effort for the simulation results of the FA to converge, symmetrical design advantage was utilized. Thus one-eighth (1/8th) the computational domain was considered and simulated. Four turbulence models were implemented and assessed with a view to choosing one turbulence model capable of capturing heat transfer characteristics of the coolant flow near, at and after the pseudo-critical region. Table 3.2 shows the selected turbulence models and their wall treatments.

Table 3.2: Turbulence models

No.	Turbulence model	Type	Wall Treatment
1	Shear-Stress Transport (SST)-Menter's	κ-ω	Low y+
2	Standard Wilcox	κ-ω	Low y+
3	Abe-Kondoh-Nagano (AKN) Low-Re	κ-ε	Low y+
4	standard Lien's Low-Re	κ-ε	Low y+

3.2 STAR-CCM+ CFD code

The STAR–CCM+ v11.06 was used in this study because of its relative easiness in the mesh generation of complex geometries. Podila and Rao [42] have confirmed that the code is suitable for modelling the geometries of fuel rod bundles with or without the complexity of spacers or wire wraps in flows at subcritical and supercritical conditions.

However, in addressing the occurrence of HTE and HTD, recommendations made by several researchers on the onset and possibility of these two heat transfer regimes occurring at normal supercritical operating conditions have been taken into account. Explanation to the performance of heat transfer results obtained from the analysis of one-eighth FA is also based on the account of normal heat transfer (NHT), heat transfer deterioration (HTD) and heat transfer enhancement (HTE).

3.2.2 Mesh Generation

Region-Based Meshing was employed for the 1/8 of a single assembly of the computational domain. This entailed generating a mesh for the 9 sub-channels surrounding all the 7 fuel pins in the 1/8 fuel assembly.

3.2.2.1 Surface Remesher

The surface remesher was used to optimize and improve of the whole quality of the existing surface for the volume mesh models by remeshing the initial surface. It was also used to re-triangulate the surface based on a user defined target edge length. However, in a bid to preserve the original triangulation from the imported mesh, specific surfaces or boundaries can be omitted in the process [39].

3.2.2.2 Trimmer Meshing Model

The trimmer meshing model was chosen and used in the generation of fine mesh due to its flexibility and easiness. “Trimmed” cell meshes provide a robust and efficient method in the production of a high quality grid for both simple and complex mesh generation problems. Trimmer mesher uses the starting input surface to cut or trim the core mesh constructed from the hexahedral cells by utilizing a template mesh. The template mesh contains refinement that is based on the local surface mesh size and local refinement controls. In trimmed cells, automatic feature refinement is included to further optimize the cell distribution [43].

3.2.2.3 Prism Layer Mesher

A prism layer is defined in terms of thickness, number of cell layers, size distribution of the layers and the function that is used to generate the distribution. The prism layer mesh

model is used in conjunction with a core volume mesh to generate orthogonal prismatic cells next to wall surfaces or boundaries. This layer of cells allows the solver to resolve near wall flow accurately, which is critical in determining flow features such as separation together with forces and heat transfer on walls. Additionally, separation affects pressure drop or drag whose accurate prediction depends on resolving the velocity and temperature gradients normal to the wall.

The following meshing models were applied in the mesh generation pipeline:

- surface remesher
- Trimmer mesher
- prism layer mesher

Specifications of the applied meshing models are shown in Table 3.3. The total number of mesh cells generated from these specifications is 1,177,342 cells.

Table 3.3: Meshing Specifications

S/No	Mesh Settings	Specification
1	Base Size (mm)	0.2
2	Prism Layer Thickness (mm)	0.1
3	Near Wall Prism Layer Thickness (mm)	0.1
4	Surface Growth Rate	1.3

The data specification of the mesh generated from Table 3.3 was applied as depicted in Figure 3.2.

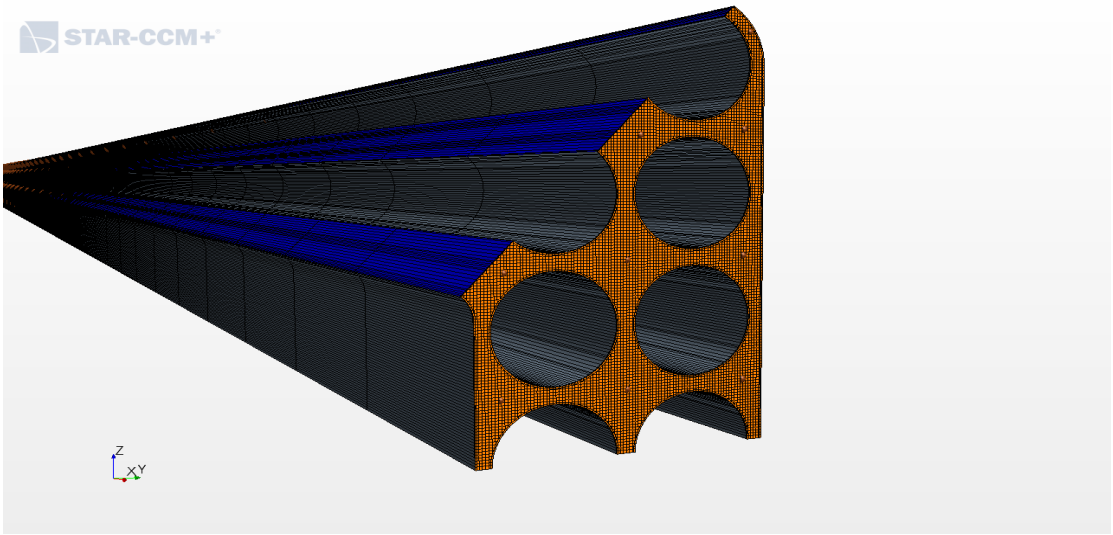

Figure 3.2: Mesh Scene of the Computational Geometry

3.2.3 Physics Modelling

Table 3.4 and Table 3.5 display the relevant initial conditions, physics models and boundary conditions respectively employed in the present work.

Table 3.4: Initial Conditions

S/No	Initial Conditions	Specification
1	Reference Pressure	25.0 MPa
2	Temperature	300 ˚C
3	Turbulence Intensity	0.01
4	Reference Density	743.01 kg/m^3

Initial conditions employed mimicked the actual operating environment of the SCWR. These conditions allowed the system to start up and stabilize thus enabling acquisition of simulation data by the code.

Table 3.5: Physics and Boundary Specifications

S/No	Physics Model	Specification
1	Space Model	3-Dimensional
2	Time Model	Steady State
3	Material	Water
4	Energy of State Model	Polynomial Density
5	Flow Model	Segregated Flow
6	Energy Model	Segregated Fluid
7	Viscous Regime Model	Turbulent
8	Turbulence Model	K-Omega
9	Wall Function	Low y^+ Treatment
10	Convection Scheme	2^{ND} Order Upwind
11	Inlet	Mass Flow
12	Outlet	Pressure
13	Wall Surface	Heat flux

3.3 Governing Equations of Flow in the STAR-CCM+

In this sub-channel computational fluid dynamics analysis, finite volume method was used to first discretize and then numerically solve the equations of Reynolds Averaged Navier-Stokes (RANS) and turbulence model simultaneously with the equations of continuity and temperature form of the energy balance in STAR CCM+. The continuity, momentum, energy and turbulence model equations are presented and discussed below regarding their impact on prediction of the sub-channel coolant temperatures, wall temperatures, outlet

temperatures. However, it must be noted that these equations are standard and their use does not depend on the choice of models by a CFD user.

The adopted notations in the equations are ρ, P, μ, μ_e, g which represents density, pressure, molecular viscosity, effective dynamic viscosity and gravity respectively.

The continuity, momentum and the energy equations are presented in the subsequent sections, equations 3.1 to 3.4.

3.3.1 Continuity equation

In general, variation of fluid properties is accounted for by employing formulas in a separate module. All the flow variables appearing in the continuity equation and in all the other transport equations are considered as mean flow, time- (or ensemble-) averaged ones, as shown in equation 3.1 [43].

$$\frac{\partial \rho}{\partial t} + \frac{\partial (\rho U)}{\partial x} + \frac{\partial (\rho V)}{\partial y} + \frac{\partial (\rho W)}{\partial z} = 0 \qquad 3.1$$

where U, V and W are components of velocity corresponding to x, y and z planes respectively, ρ = density, x, y *and* z are the coordinates and t is the time.

In the momentum equations, the Reynolds stresses that result from the process of averaging of the instantaneous Navier-Stokes equations are modelled using the Boussinesq approximation, i.e., assuming that they are proportional to mean rates of deformation, with the turbulent viscosity μ_t as the proportionality "factor".

3.3.2 U-momentum equation

Similarly, the equations 3.2, 3.3 and 3.4 represent the turbulent momentum equations [43]:

$$\frac{\partial(\rho U^2)}{\partial t} + \frac{\partial}{\partial x}\left(\rho U^2 - \mu_e \frac{\partial U}{\partial x}\right) + \frac{\partial}{\partial x}\left(\rho UV - \mu_e \frac{\partial U}{\partial x}\right) = -\frac{\partial P}{\partial x} + \rho g_x \quad (3.2)$$

3.3.3 V-Momentum equation is given by

$$\frac{\partial(\rho V)}{\partial t} + \frac{\partial}{\partial x}\left(\rho UV - \mu_e \frac{\partial V}{\partial x}\right) + \frac{\partial}{\partial y}\left(\rho V^2 - \mu_e \frac{\partial V}{\partial y}\right) = -\frac{\partial P}{\partial y} - \frac{\partial}{\partial z}\left(\rho VW - \mu_e \frac{\partial V}{\partial z}\right) + \rho g_y \quad (3.3)$$

3.3.4 W-Momentum equation is given by

$$\frac{\partial(\rho W)}{\partial t} + \frac{\partial}{\partial x}\left(\rho UW - \mu_e \frac{\partial W}{\partial x}\right) + \frac{\partial}{\partial y}\left(\rho VW - \mu_e \frac{\partial W}{\partial y}\right) = -\frac{\partial P}{\partial y} - \frac{\partial}{\partial z}\left(\rho W^2 - \mu_e \frac{\partial W}{\partial z}\right) + \rho g_z \quad (3.4)$$

where, ρ is the density of the fluid, P is the pressure, and τ is the viscous stress.

3.3.5 Energy Balance equation

Supercritical fluid properties vary dramatically as a function of temperature in the vicinity of the pseudo-critical temperature. These sharp variations can give rise to numerical instabilities that make convergence difficult [43].

$$\rho \frac{DE}{Dt} = -div(PU) + \left[\frac{\partial(U\tau_{xx})}{\partial x} + \frac{\partial(U\tau_{yx})}{\partial y} + \frac{\partial(U\tau_{zx})}{\partial z} + \frac{\partial(V\tau_{xy})}{\partial x} + \frac{\partial(V\tau_{yy})}{\partial y} + \frac{\partial(V\tau_{zy})}{\partial z} + \frac{\partial(W\tau_{zx})}{\partial x} + \frac{\partial(W\tau_{zy})}{\partial y} + \frac{\partial(W\tau_{zz})}{\partial z}\right] + div(kgradT) + S_E \quad (3.5)$$

3.4 Turbulence Modelling

Computational modelling plays a vital role in improving the understanding of the physics of convective heat transfer to fluids at supercritical pressures and assist with the development of correlation for engineering application. Reynold's-Averaged Navier-Stokes (RANS) approach which uses time average quantities and has the advantage to shorten computing time was used. The two types of turbulence models used in this work were the κ-ε and the κ-ω turbulence models. The ε is the energy dissipation rate of κ, while the ω is the specific heat dissipation rate by Wilcox in 1998 [44, 45].

Four turbulence models were selected and tested for this study to predict the heat transfer flow performance in the one-eighth FA and any occurrence of HTD and HTE, namely; κ-epsilon Abe-Kondoh-Nagano turbulence model (AKN), standard low-Reynolds turbulence model, κ-ω Shear-Stress Transport turbulence model (SST) and the Standard Wilcox - omega turbulence model with the basic transport equations of the four different turbulence models, their terms as well as their constants are discussed below:

3.4.1 Standard low-Reynolds κ-ε turbulence model

This model has identical coefficients to the Standard κ-ε model, but provides more damping functions. These functions are applicable in the viscous-affected regions near walls. It includes transport equation for turbulent kinetic energy and its dissipation rate ε. The transport equations are suggested by Durbin [46] with the coefficients suggested by Jones and Launder [47]. Some additional terms have been added to the model in STAR-CCM+ to account for effects such as buoyancy and compressibility.

Turbulence Equation for standard low-Reynolds turbulence model

- The κ term for standard low-Reynolds is given by equation 3.6:

$$\int_v \frac{\partial \rho \kappa}{\partial t}[G_k - G_b + \rho(\varepsilon - \varepsilon_0)\gamma_M - S_\kappa]dV = \int_v \left[\left(\mu + \frac{\mu_t}{\mu_\kappa}\right)\nabla\kappa - \rho\kappa(v - v_g)\right]da \quad (3.6)$$

Where S_κ, μ_κ, v, ρ, v_g, ε, ε_0, μ, μ_t, κ are source term, velocity, turbulent kinetic energy, density, velocity of gas, rate of dissipation of κ, ambient turbulence value, viscosity, turbulent viscosity, kinetic energy respectively. The following terms G_b,G_k, da, dV are production term, kinetic energy production term, change in area, change in volume respectively.

- The ε term for standard low-Reynolds is given by equation 3.7:

$$\int_v \frac{\partial \rho \kappa}{\partial t} - \frac{1}{T}\left[C_{\varepsilon_1}(G_k - G_{n_1} - G' - C_{\varepsilon_3}G_b) + C_{\varepsilon_2}f_2\rho(\varepsilon - \varepsilon_0) - pY - S_\kappa\right]dV = \int_v \left[\left(\mu + \frac{\mu_t}{\sigma_\kappa}\right)\nabla\rho\varepsilon - \rho(v - v_g)\right]da \quad (3.7)$$

S_κ and S_ε are the user-specified source term, ε_0 is the ambient turbulence value in the source term that counteract turbulence decay and G' is an additional term, while, f_1, f_2 and f_3 are damping functions.

$$G = Df_2\left(G_k + 2\mu\frac{k}{y^2}\exp(-ERe_y^2)\right); f_2 = 1 - CexpRe_T^2, Re_y = \sqrt{\frac{ky}{v}}, Re_t = \frac{k^2}{\varepsilon v}$$

3.4.2 Abe-Kondoh-Nagano (AKN) κ-ε Turbulence Model

The AKN model [55] works well for wide range of complex flows. It has different coefficients than standard low-Reynolds model and uses different damping functions than standard low-Reynolds number. This model is a good choice for applications such as compact heat exchangers, where the Reynolds numbers are low but the flow is relatively complex.

3.4.3.1 Turbulence Equation for AKN Turbulence Model

- The κ term for AKN is given by equation 3.8:

$$\int_v \frac{\partial \rho \kappa}{\partial t}[G_k - G_b + \rho(\varepsilon - \varepsilon_0)\gamma_M - S_\kappa]dV = \int_v \left[\left(\mu + \frac{\mu_t}{\sigma_\kappa}\right)\nabla\kappa - \rho\kappa\left(v - v_g\right)\right]da \quad (3.8)$$

- The ε term for AKN is given by equation 3.9:

$$\int_v \frac{\partial \rho \varepsilon}{\partial t} - \frac{1}{T}\frac{\varepsilon}{k}\left[C_{\varepsilon_1}(G_k - C_\varepsilon G_b) + C_{\varepsilon_2} - \rho(\varepsilon - \varepsilon_0) - pY_y - S_\varepsilon\right]dV = \int_A \left[\left(\mu + \frac{\mu_t}{\sigma_k}\right)\nabla k - \rho k\left(v - v_g\right)\right] \quad (3.9)$$

Where S_k and S_ε are user-specified source term , $\varepsilon_0$is the ambient turbulence value in source terms that counteract turbulence decay and $f_2$is a damping function and is given by

$$f_2 = \left[1 - exp\left(\frac{-Re_\varepsilon}{3.1}\right)\right]^2\left\{1 - 0.3exp\left[-\left(\frac{Re_t}{6.5}\right)^2\right]\right\}, Re_t = \frac{(v\varepsilon)^{1/4}}{v}$$

3.4.3 Shear-Stress Transport (SST) *κ-ω* Turbulence Model

The Shear-Stress-Transport (SST) *κ-ω* model developed by Menter [48], was designed to produce the best satisfying behavior of the *κ-ω* model formulated by Wilcox. In the same vein sensitivity problem has also been addressed. Basically, the original *κ-ω is* utilized by Menter's model in the "near wall region" (sub and log layer) and steadily shifts to the standard *κ-ε* model in the "fully turbulent" region far away from the wall. The blending function is used to facilitate this switch. The transport equations for the SST *κ-ω* turbulence model are presented in the following subsections.

3.4.3.1 Turbulence Equation for SST Turbulence Model

- The *κ* term in the SST model is given by equation 3.10:

$$\int_v \left[\frac{\partial \rho \kappa -}{\partial t} - \gamma_{eff} G_\kappa + YP\beta^* f_{\beta^*}(\omega\kappa - \omega_0 k_0) - S_\kappa - \rho\omega\right] dV = \int_A \left[\left(\mu + \frac{\mu_t}{\sigma_\kappa}\right)\rho\kappa\left(v - v_g\right)\right] da \quad (3.10)$$

- The *ω* term for SST model is given by equation 3.11:

$$\int_v \left[\frac{\partial \rho\omega}{\partial t} - G_w + \rho\beta F_\beta(\omega^2 - {\omega_0}^2) - D_w - S_w\right] dV = \int_A [(\mu + \sigma_\omega \mu_t) - \rho\omega\left(v - v_g\right)] da \quad (3.11)$$

where S_κ and S_w are the user-specified source term, k_0 and ω_0 are the ambient turbulence source terms that counteract turbulence decay, γ_{eff} is the intimacy provided by the Gamma, Re Theta Transitional model $\gamma = min[\max(\gamma_{eff}, 0.1), 1]$, D_ω= cross-derivation term.

3.4.3 Standard Wilcox Turbulence Model

Wilcox has revised his original model twice in 1998 and 2008, to address the perceived deficiencies that the original version (1988) had.

The revisions made include the following:

- A set of revised coefficients of the model
- Two corrections to account for sensitivity to free-stream / inlet conditions both were based on products of $\Delta\kappa$ and $\Delta\omega$. The first model introduced in 1998 is a modification of the turbulent kinetic energy equation. The most recent revision [49] is the introduction of cross-diffusion term that is similar to that used in the SST
- A correction to improve the free shear-stress-flow spreading rates of the model
- A compressibility correction
- Low-Reynolds number corrections that allow the K-Omega model to be better applied in the prediction of low-Reynolds number or transitional flows

3.4.3.1 Basic Standard K-Omega Model Transport Equations

The transport equations for the standard K-Omega model are:

- The κ term in the SST model is given by equation 3.12,

$$\frac{d}{dt}\int_V \rho\kappa dV + \int_A \rho\kappa(v - v_g)\cdot d\boldsymbol{a} = \int_A (\mu + \sigma_k\mu_t)\nabla\kappa\cdot d\boldsymbol{a} + \int_V \left[G_\kappa - \rho\beta^* f_{\beta^*}(\omega\kappa - \omega_0 k_0) + S_\kappa\right]dV \quad (3.12)$$

The ω term in the SST model is given by equation 3.13,

$$\frac{d}{dt}\int_V \rho\omega dV + \int_A \rho\omega(\boldsymbol{v}-\boldsymbol{v}_g)\cdot d\boldsymbol{a} = \int_A (\mu+\sigma_\omega\mu_t)\nabla\omega\cdot d\boldsymbol{a} + \int_V \left[G_\omega - \rho\beta F_\beta(\omega^2-{\omega_0}^2) + S_\omega\right]dV \quad (3.13)$$

Where S_k and S_ω are the user-specified source terms. k_0 and ω_0 are the ambient turbulence values in source terms that counteract turbulence decay.

3.4.3.2 Model Coefficients

Without the low-Reynolds number modifications, the coefficients defining the model have the following values:

$$\beta^* = 0.09\,,\quad \beta = \frac{9}{125}\,,\quad \alpha = \frac{13}{25}$$
$$\alpha^* = 1\,,\quad \sigma_k = 0.5\,,\quad \sigma_\omega = 0.5$$

Model constants are given as;

Turbulence model constants for κ-ε –models

Model	C_μ	C_{ε_1}	C_{ε_2}	σ_κ	σ_ε
AKN	0.09	1.5	1.9	1.4	1.4
V2F	0.09	1.4	1.9	1	1.3
Standard low-Re	0.09	1.44	1.92	1	1.3

C_{ε_3} depends on the literature reference and is meant to be used only with P_b term.

3.5 Heat transfer coefficient in STAR CCM+ code

The STAR CCM+ provides two methods of computing the heat transfer coefficients, using the correlation and the field function. In using a field function, heat transfer coefficient method allows $\boldsymbol{h}$ to be specified directly with a scalar field function $\boldsymbol{f}$ (equation 3.14).

$$\boldsymbol{h = f} \tag{3.14}$$

The heat transfer correlation expression that comes with STAR CCM+ code is the Ranz Marshall correlation supplied by a field function. It is activated only when the continuous phase is viscous [50]. The correlation is formulated and expressed as presented by equation (3.15):

$$Nu_p = 2\left(1 + 0.3Re_p^{1/2}\, Pr^{1/3}\right) \tag{3.15}$$

Where $Re_p \simeq 5000$ and Pr is Prandtl number of the continuous phase.

The heat transfer coefficient in STAR CCM+ is computed using Nusselt number from the Ranz Marshall correlation:

$$Nu_p = \frac{h\, D_p}{k} \tag{3.16}$$

Or expressed as shown in equation (3.16) by making h as the subject of the formula:

$$h = \frac{Nu_p\, k}{D_p} \tag{3.17}$$

where D_p is hydraulic diameter, k is the thermal conductivity of continuous phase, h is the heat transfer coefficient and Nu_p is the Nusselt number and is computed using the Ranz Marshall correlation [50].

3.6 Heat Transfer Correlation Assessment

Twelve different heat transfer correlations were considered and implemented in this work. This was to analyze their effects on the prediction of wall temperature in the proposed fuel

assembly using STAR-CCM+ computer code. The heat transfer correlations applied in this study are shown in Tables 3.6, 3.7 and 3.8.

Heat transfer correlations can be categorized into three types for supercritical fluids. The first category which performs well in the prediction of heat transfer in single phase fluids at subcritical conditions and is derived from the expression based on the Dittus and Boelter correlation [51]. For the second category, a frictional factor has been added to the developed correlation equations for heat transfer in supercritical fluids that have been developed by Russian researchers. Most of the heat transfer correlations in the last category have been developed in recent years based on the "mechanisms of heat transfer at supercritical pressures". With a view to increasing an in-depth knowledge on the mechanisms of heat transfer enhancement and deterioration phenomena, some researchers [52, 53, 54] have deduced that buoyancy and thermal acceleration plays dominant and significant roles in the prediction of wall temperatures. The HTC in the supercritical water must be addressed prior to, and during the formulation and development of new empirical correlations.

As can be seen in the tables below (Table 3.6, Table 3.7 and Table 3.8), amid the 12 selected heat transfer correlations, only the Dyadyakin and Popov correlation [55] was developed for rod bundle while the remaining 11 correlations were principally proposed and recommended for tubes. In this analysis, 12 correlations were implemented and their prediction capabilities of heat transfer for supercritical water based on the wall temperatures and heat transfer coefficients assessed in the proposed fuel assembly. For the applicability range of the twelve selected heat transfer correlations are presented in Appendix B.

Table 3.6: Heat transfer correlations derived from Dittus-Boelter equation.

References	Correlations	Flow Geometry
Dittus and Boelter [51]	$Nu_b = 0.023 Re_b^{0.8} Pr_b^{0.4}$	Tubes
Griem [56]	$Nu_b = 0.0169 Re_b^{0.8356} Pr_b^{0.432}$	Tubes
Shitsman [57]	$Nu_b = 0.023 Re_b^{0.8} Pr_{min}^{0.8}$	Tubes (D = 7.8, 8.2 mm)
Bishop et al. [40]	$Nu_b = 0.0069 Re_b^{0.9} \overline{Pr}_b^{0.66} \left(\frac{\rho_w}{\rho_b}\right)_x^{0.43} \left(1 + 2.4 \frac{D_{hy}}{x}\right)$	Tubes (D = 2.5, 5.1 mm)
McAdams et al. [58]	$Nu_b = 0.023 Re_f^{0.8} Pr_f^{0.33} \left(1 + 2.3 \frac{D_{hy}}{l}\right)$	Tubes
Ornatsky et al. [59]	$Nu_b = 0.023 Re_b^{0.8} Pr_{min}^{0.8} \left(\frac{\rho_b}{\rho_w}\right)^{0.3}$	Tube (D = 3 mm)
Dyadyakin and Popov [55]	$Nu_b = 0.021 Re_b^{0.8} \overline{Pr}_b^{0.7} \left(\frac{\rho_w}{\rho_b}\right)_x^{0.45} \left(\frac{\mu_b}{\mu_{in}}\right)^{0.2} \left(\frac{\rho_b}{\rho_{in}}\right)^{0.1} \left(1 + 2.5 \frac{D_{hy}}{x}\right)$	Bundles (D_{hy} = 2.15–2.77 mm)
Mokry et al. [12]	$Nu_b = 0.0061 Re_b^{0.904} \overline{Pr}_b^{0.684} \left(\frac{\rho_b}{\rho_w}\right)^{0.564}$	Tube (D = 10 mm)
Gupta et al. [60]	$Nu_b = 0.0061 Re_w^{0.94} \overline{Pr}_w^{0.76} \left(\frac{\mu_w}{\mu_b}\right)^{0.4} \left(\frac{\rho_b}{\rho_w}\right)^{0.16}$	Tube (D = 10 mm)

Table 3.7: Heat transfer correlations with frictional factor incorporated.

References	Correlation	Flow Geometry
Petukhov et al. [61]	$St = \frac{Nu}{Re \cdot Pr} = \frac{(\xi/8)}{12.7\sqrt{(\xi/8)}(\overline{Pr}_b^{2/3} - 1) + 1 + \frac{900}{Re}}$, $where\ \xi = \frac{1}{(1.82logRe_b - 1.64)^2}\left(\frac{\rho_w}{\rho_b}\right)^{0.4}\left(\frac{\mu_w}{\mu_b}\right)^{0.2}$	Tubes, upwards, downwards and horizontal (D= 8 mm, L= 1.67 m)
Krasnoshchekov-Protopopov [62]	$Nu_b = Nu_o\left(\frac{\mu_b}{\mu_w}\right)^{0.11}\left(\frac{\lambda_b}{\lambda_w}\right)^{0.3}\left(\frac{\bar{C}_p}{C_{p_b}}\right)^{0.35}$, $Nu_o = \frac{(\xi/8)Re_b\overline{Pr}}{12.7\sqrt{(\xi/8)}(\overline{Pr}_b^{2/3} - 1) + 1.07}, where$ $\xi = (1.82logRe_b - 1.64)^2$	Tubes (D = 1.6–20 mm)

Table 3.8: Heat transfer correlations taking into account buoyancy and thermal acceleration.

References	Correlation	Flow Geometry
Cheng et al. [52]	$Nu_b = 0.023Re_b^{0.8}Pr_b^{0.33}F, where$ $F = \min(F_1, F_2), \quad F_1 = 0.85 + 0.766(\pi_A \cdot 10^3)^{2.4}$ $F_2 = \frac{0.48}{\left(\pi_{A_{pc}} \cdot 10^3\right)^{1.55}} + 1.21(1 - \frac{\pi_A}{\pi_{A_{pc}}}\ and\ \pi_A = \frac{\beta_b q}{GC_p}$	Tubes (D = 10, 20 mm)
Chen and Fang [63]	$Nu_b = 0.46Re_b^{0.16}\left(\frac{Pr_w}{Pr_b}\right)^{0.1}\left(\frac{\nu_w}{\nu_b}\right)^{-0.55}\left(\frac{\bar{C}_p}{C_{p_b}}\right)^{0.88}\left(\frac{Gr_b^*}{G_r}\right)^{0.81}$	Tubes (D = 6–26 mm)

CHAPTER FOUR : RESULTS AND DISCUSSION

This chapter presents the simulation results and discussions of the performance of heat transfer in the proposed 1/8th fuel assembly based on the assessment of the four selected turbulence models (presented in Table 3.2), twelve heat transfer correlations (presented in Table 3.6 Table 3.8) compared with Wataa's numerical data [17] and the parametric analysis based on the influence of parameters such as mass flow rate, pressure and gravity.

4.1 Convergence Criteria

To ascertain that the simulations have converged, both the residuals and bundle average outlet temperature monitor were used as illustrated in Figure 4.1 and Figure 4.2 respectively. The simulations were run until convergence by monitoring residual plots to achieve a stabilised value over an acceptable continuous period. A typical converged simulation is illustrated in the Figure 4.1.

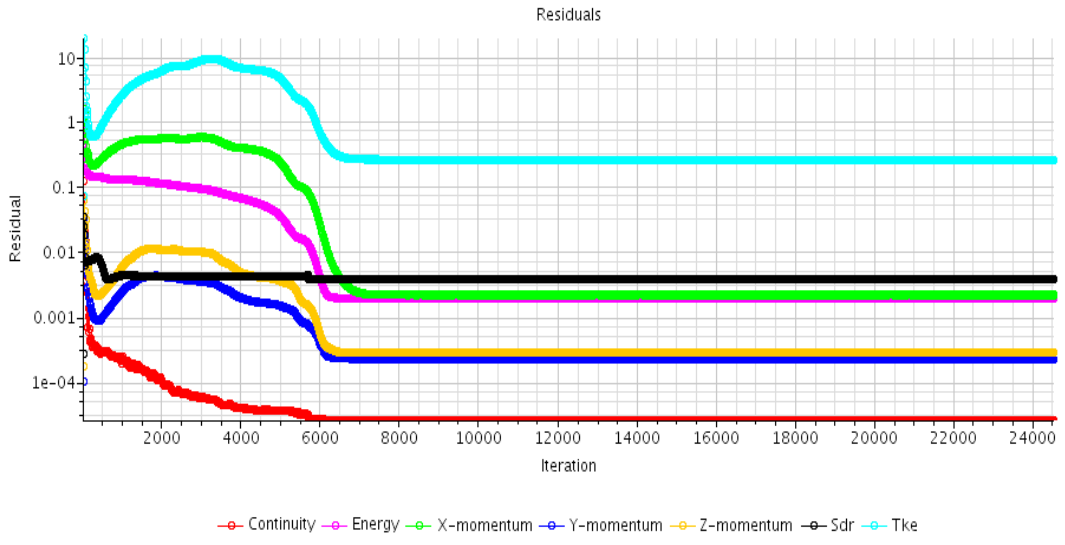

Figure 4.1: Residual Plot of a Converged Simulation

NB: Sdr is specific dissipation rate and Tke is turbulent kinetic energy monitors

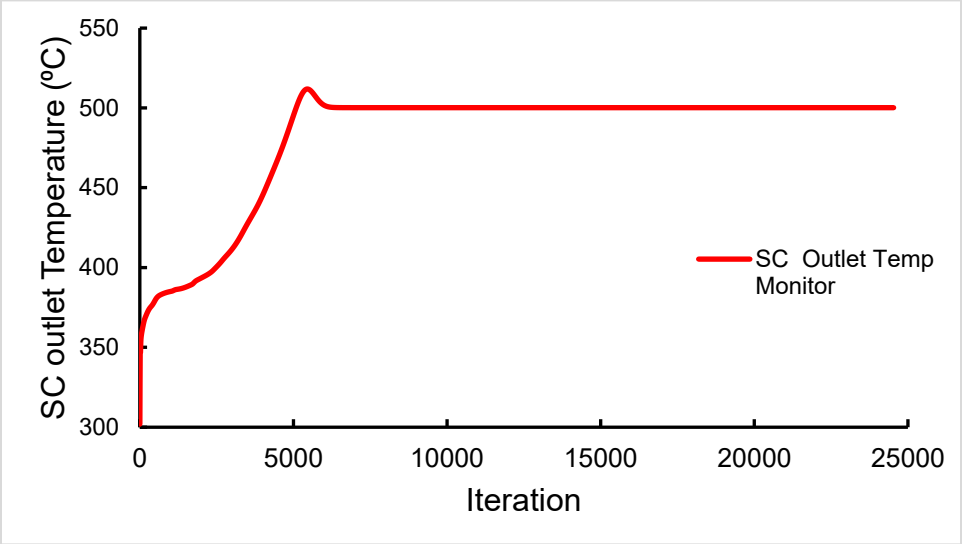

Figure 4.2: Sub-channel Outlet temperature monitor of the 1/8th FA

Results obtained in the following subsections depicts the performance of the four turbulence models, assessment of the heat transfer correlations and the parametric sub-channel analysis. The system pressure was set at 25 MPa and 23 MPa for parametric analysis. The mass flow rates were set at 0.1670 kg/s (601.2 kg/h) and 0.1599 kg/s (561.2 kg/h), inlet sub-channels' temperature of 300 °C, 650 kW/m^2 as heat flux and mass fluxes depicted in Table 4.1.

Table 4.1: Mass fluxes for nine individual sub-channels

Sub-channel Label	1	2	3	4	5	6	7	8	9
G₀ (kgm²s)	790.5	1003.2	894.3	1003.2	790.5	790.5	997.5	790.5	510.7

4.2 Turbulence Model Prediction Analysis

The governing equations were numerically solved using a STAR CCM+ CFD solver. Several turbulence models (Standard (Wilcox) and SST (Menter's) κ-ω Models, Low-Re

(Liens) *κ-ε* and AKN *κ-ε)* with low-y+ wall treatment have been studied for the heat transfer performance and the prediction of temperatures in the sub-channels. The results of the simulations have been compared with Wataa's numerical data. It was found that the standard (Wilcox) and SST *κ-ω* Models **(**with low-y+ wall treatment) were to an extent able to capture qualitative trends of the sub-channel coolant temperature results observed in the Wataa data. The Low-Re (Lien)-*κ-ε* Model **(**with low-y+ wall treatment) provided the least prediction results in all the nine sub-channels modelled.

The working pressure for the FA was set at 25 MPa, inlet temperature at 300 °C, and the mass flow rate and heat flux at 0.167 kg /s (601.2 kg/h) and 650 kW/m^2 respectively. Figure 4.3, shows the sub-channel wall and coolant (fluid center-line) temperatures distribution predicted by four different turbulence models against Wataa's data.

4.3 Comparison of obtained numerical results with Wataa's numerical data

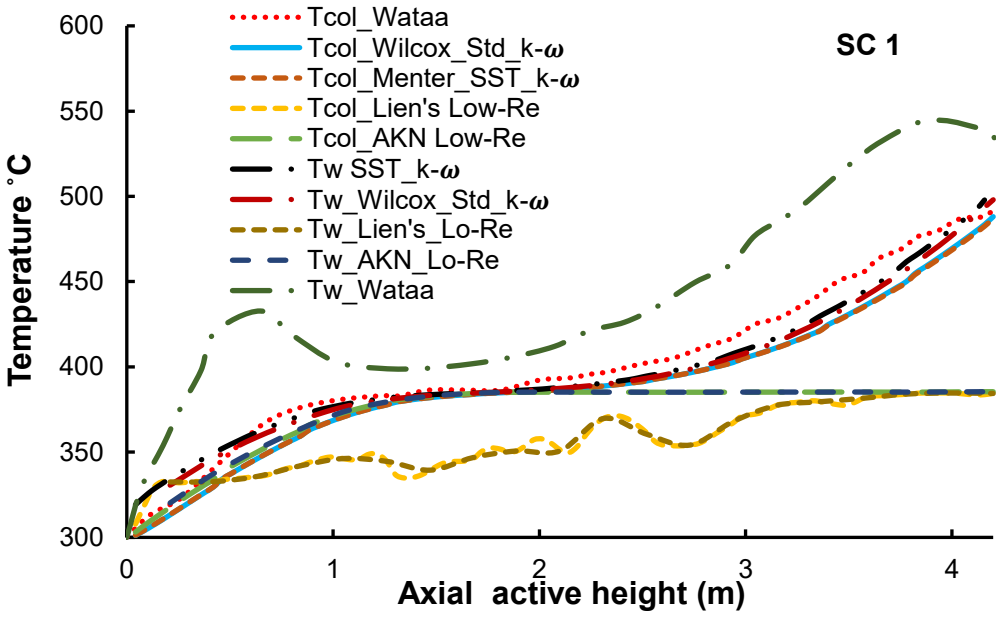

Figure 4.3: Temperature profiles in SC 1 of a square 2.1 fuel assembly

It was observed that the κ-ω SST (Menter's) and κ-ω STD (Wilcox) turbulence models were in agreement with each other and gave similar temperature values for both the wall and coolant. However, as it can been seen in Figure 4.3, the two κ-ω models closely captured the temperature trend in SC (1) obtained by Wataa. The Lien's standard Lo-Re κ-ε turbulence model under predicted the coolant temperature distribution along the active height. It was also observed that the coolant temperature trend predicted by Lien's κ-ε model was below the pseudo-critical temperature in SC (1) except towards the outlet of the sub-channel where temperature reached the pseudo-critical temperature. A similar trend was observed as well, in sub-channels 2 to 9 (See Figure 4.4 to Figure 4.11).

In a case of the wall temperatures, it was observed that the wall temperatures predicted by all the four turbulence models was below that of Wataa's numerical data (in all the three heat transfer regions), in the Normal Heat Transfer (NHT) region the Lien's wall temperature was far below the Wataa's temperature while that of the Wilcox and SST κ-ω models was slightly close to the Wataa's in sub-channels 1 and 2 as displayed in Figure 4.3. In the enhanced heat transfer region, the wall temperature trends predicted by the three turbulence models (AKN, SST and Wilcox κ–ω) were closer to that of Wataa's data between 1.2 m and 2 m. In addition, the AKN wall temperature flattened in the NHT region up to the outlet of the sub-channel. Deteriorated heat transfer region was only observed for the two κ-ω turbulence models (Menter's SST and standard Wilcox), similarly the predicted temperatures by the two turbulence models was below that of Wataa's data.

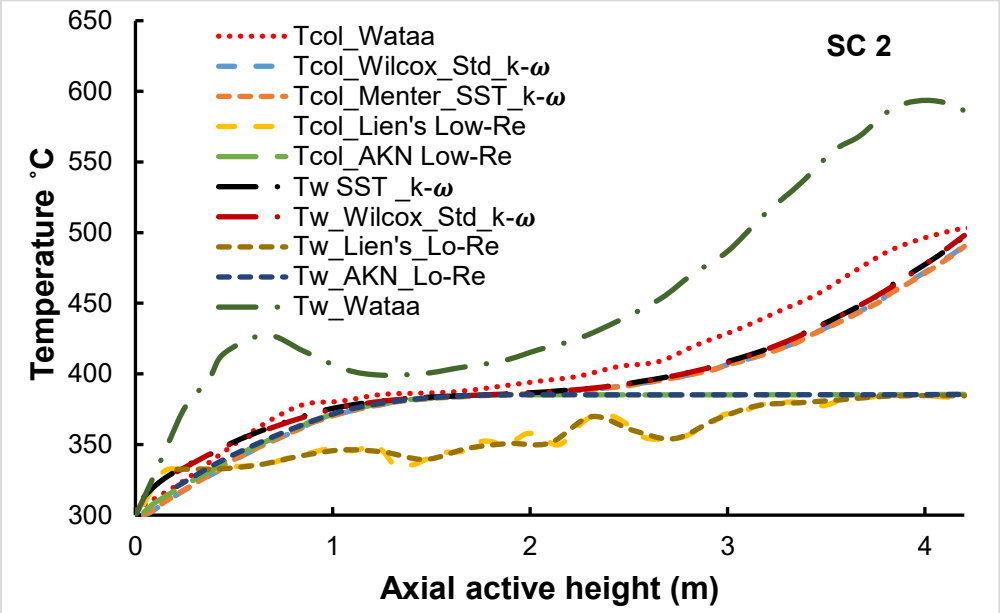

Figure 4.4: Temperature profiles in SC 2 of a square 2.1 fuel assembly

Figure 4.4 to Figure 4.11 (SC 2 to SC 9), similarly presents the coolant temperature and wall temperature distributions of each individual sub-channel predicted by four different turbulence models. For the coolant temperature trends, the sub-channel coolant (fluid centre-line) temperature increases from the sub-channel inlet up to the sub-channel outlet as observed in all the sub-channels. The pseudocritical temperature for the three (3) turbulence models namely κ-ω SST, standard Wilcox κ-ω and AKN) was reached at 1.7 m in sub-channels 1 to 8, except in sub-channel 9 where it was first reached at 1.05 m (see Figure 4.11) by the two κ-ω models. The pseudocritical temperature for AKN turbulence model prediction also occurred at 1.7m.

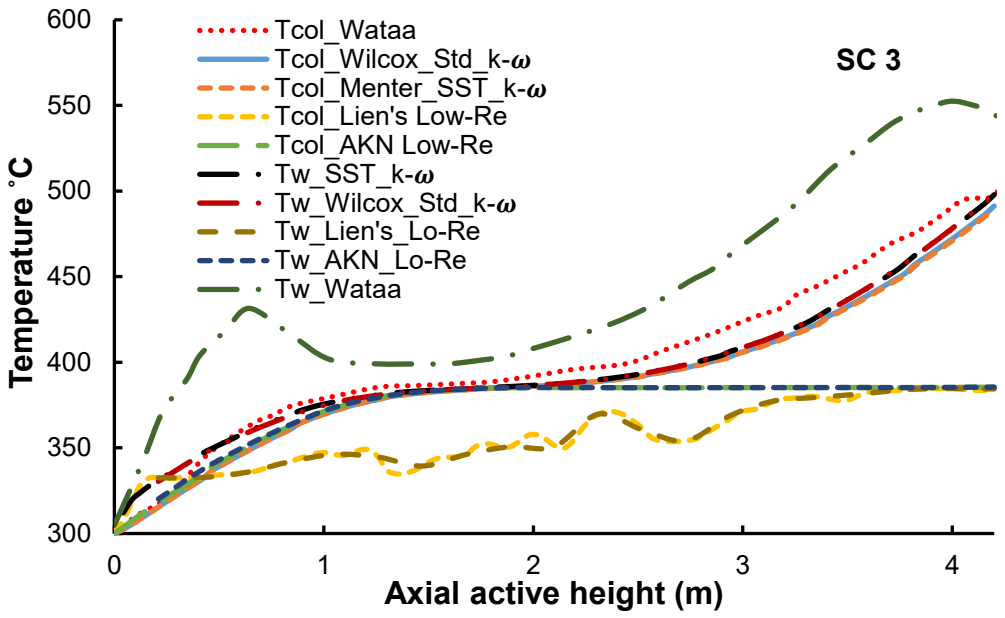

Figure 4.5: Temperature profiles in SC 3 of a square 2.1 fuel assembly

It was observed that, the trends and values of the wall and coolant temperatures predicted by κ-ω SST (Menter's) and standard (Wilcox) κ-ω turbulence models were nearly the same in all the sub-channels except in sub-channels 8 and 9 where the wall temperatures predicted by κ-ω SST were larger than that of the standard (Wilcox) κ-ω in the deteriorated heat transfer region (Figure 4.10 and Figure 4.11). Similarly, the coolant temperatures predicted by κ-ω SST were larger than that of the standard Wilcox κ-ω above the pseudo-critical region. This significant observation made, can be due to the simple form of κ-ω model which makes it to be superior to others (κ-ε models) especially with regard to numerical stability. In addition, κ-ω solves specific dissipation rate equation and also does not involve damping functions as compared to the κ-ε model.

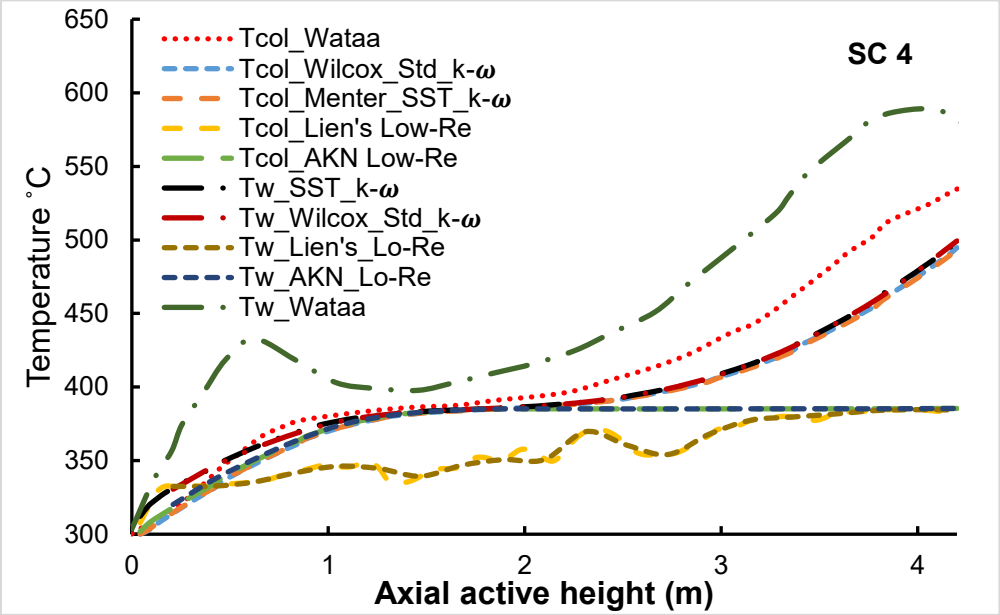

Figure 4.6: Temperature profiles in SC 4 of a square 2.1 fuel assembly

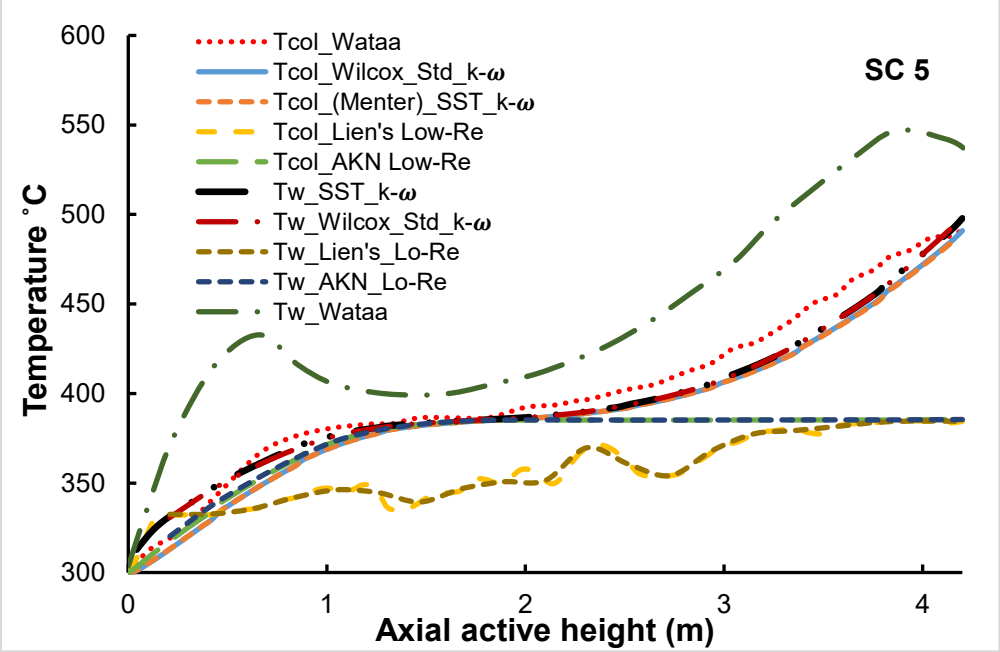

Figure 4.7: Temperature profiles in SC 5 of a square 2.1 fuel assembly

Furthermore, it was observed that AKN κ-ε and Lien's Lo-Re κ-ε turbulence models under predicted the coolant temperature distributions in sub-channels 2 to 9.

Accordingly, the coolant flow temperatures in sub-channels (4) and (7) predicted by the two κ-ω turbulence models (SST and standard Wilcox) were slightly below that of Wataa, especially in the upper part along the active height of the sub-channels (above pseudo-critical region) as illustrated in Figure 4.6 and Figure 4.9 respectively. However, the two κ-ω models closely captured the temperature trends obtained by Wataa in sub-channels 3, 5 and 6, as presented in Figure 4.5, Figure 4.7 and Figure 4.8 respectively. A similar trend was observed in sub-channel 8 (Figure 4.10).

On the other hand, the two κ-ε models especially the Lien under predicted the temperature trends obtained by Wataa, as displayed from Figure 4.3 to Figure 4.11. It was also observed that the Lien's κ-ε turbulence model did not yield favorable prediction results, this is due to the fact that the same temperature values in all the nine sub-channels were obtained (see Appendix F 3).

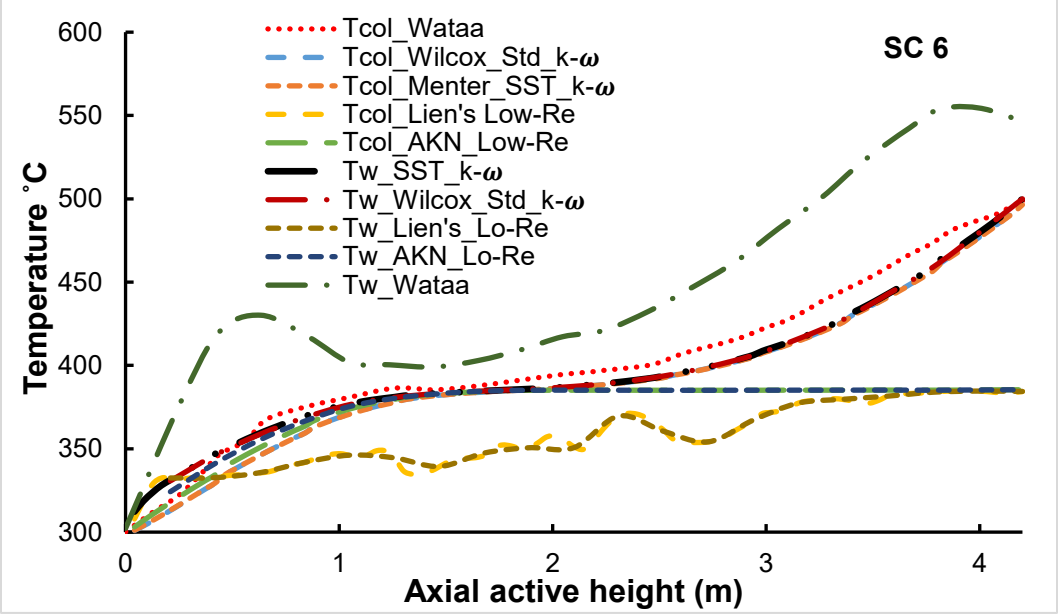

Figure 4.8: Temperature profiles in SC 6 of a square 2.1 fuel assembly

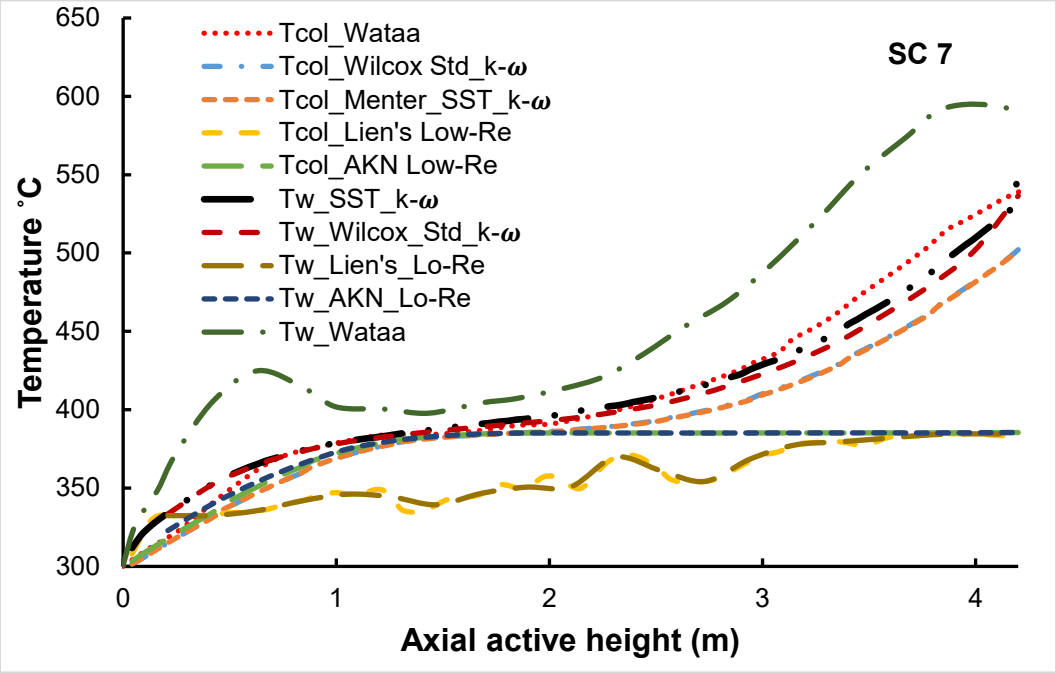

Figure 4.9: Temperature profiles in SC 7 of a square 2.1 fuel assembly

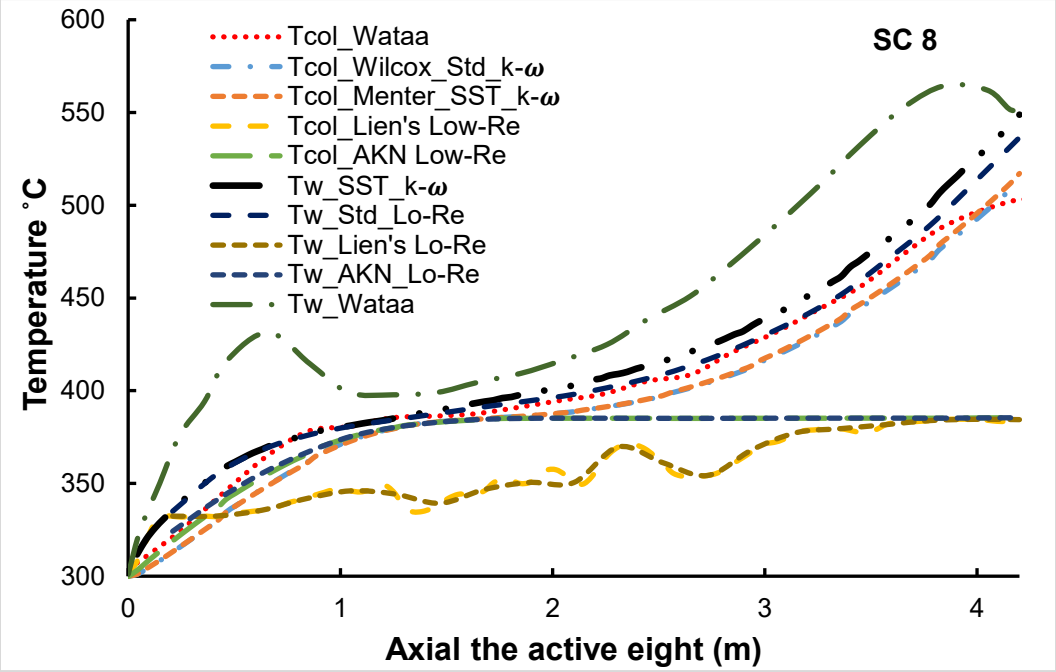

Figure 4.10: Temperature profiles in SC 8 of a square 2.1 fuel assembly

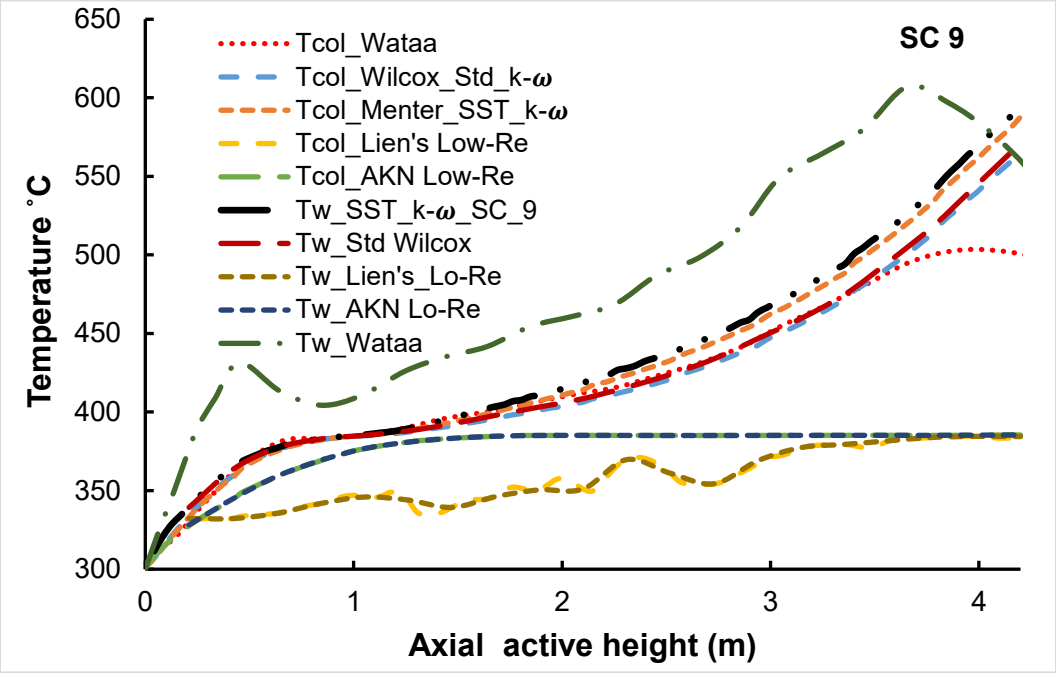

Figure 4.11: Temperature profiles in SC 9 of a square 2.1 fuel assembly

Figure 4.11 equally shows the temperature profiles in sub-channel 9 which is located in corner part of the fuel assembly. Accordingly, the coolant temperature obtained by Standard Wilcox κ-ω model closely predicted Wataa's coolant temperature from the entrance of the sub-channel to about 3.78 m (below, in and above the pseudo-critical regions). A similar trend was observed for the κ-ω SST only up to 2.1 m. However, there was a coolant temperature spread of 60 °C and 88 °C in sub-channel 9 for the Standard Wilcox κ-ω and κ-ω SST respectively (See also Appendix F 6 and 8), this was due to a low mass flux in sub-channel 9.

With a case of wall temperature, trends of wall temperatures were produced by the four turbulence models for NHT, HTE (Heat Transfer Enhancement) and HTD (Heat Transfer Deterioration) regions in sub-channel 1, trends were nearly obtained in sub-channels 2 to 9 (from Figure 4.4 through to Figure 4.11). However, in sub-channels 7, 8 and 9 the wall

temperature obtained by the κ-ω SST were closer to the wall temperatures obtained by Wataa in the HTE and HTD regions. It was also observed that the temperature difference between the average wall temperature and the coolant (fluid centre-line) temperature was small in all the sub-channels (predicted by the code). This was attributed to the fact that the sub-channel flow area of coolant absorbing heat from the heated walls was relatively small, hence the small observed temperature difference.

The following were deduced from the assessment of the turbulence models in terms of the predicted fluid temperatures:

- For the two κ-ω models (SST and Standard Wilcox), the pseudo-critical temperature of 384.9 °C was reached at 1.7 m in SCs (1) to (8), (see Figure 4.3, Figure 4.4 through to Figure 4.10 except in sub-channel 9 (Figure 4.10) where it was first reached at 1.08 m close to the entrance as compared to 1.0 m in all the 9 sub-channels reported by Wataa [20]. An average outlet temperature of approximately 500 °C was evaluated for the SST κ-ω and Standard (Wilcox) κ–ω Turbulence model.
- For AKN κ-ε turbulence model's temperature trends, the pseudo-critical temperature of 384.9 °C was reached at 1.7 m in all the nine sub-channels. Beyond 1.7 m the temperature trend flattened (did not exceed 386 °C) and was far below that of the Wataa's prediction (see also Appendix F1).
- In case of Lien's Lo-Re κ-ε Turbulence Model, the predicted temperature in all nine sub-channels is same and equal in value. However, it was observed that the temperatures along the axial active length are also lower than 384.9 °C pseudo-

critical temperature except at outlet end of the sub-channels (see also Appendix F 3).

From the assessment results of the turbulence models obtained, it can be inferred that the most suitable turbulence models capturing the coolant temperature obtained by Wataa in this analysis were found to be κ-ω SST (Menter's) and standard (Wilcox) κ-ω. Nevertheless, SST κ-ω (Menter's) turbulence model was selected due to its widely usage and recommendations given by several researchers [42, 54, 64] who have carried out analysis on heat transfer behaviour at supercritical conditions in SCWRs. Hence, the SST κ-ω (Menter's) turbulence model with a low y+ wall treatment was used to carry out the numerical simulations in this work. Using the selected SST κ-ω (Menter's), the temperature profiles in all the sub-channels were visualized at 0.25 m, 2 m and 4 m as illustrated in appendix E check the hottest and coldest sub-channels. In addition the density variation was also evaluated along the active height (see appendix D).

4.4 Assessment of heat transfer correlations

Numerical data and SST κ-ω turbulence model were used to analyze the effect of the heat transfer correlations on the wall temperature prediction of HPLWRs $1/8^{th}$ fuel assembly. The operating pressure was 25 MPa, inlet temperature of 300 °C, 0.1670 kg/s (601.2 kg/h) as mass flow rate, a uniform heat flux of 650 kW/m^2 for the FA. The red and dark blue dotted lines on the wall temperature graphs are fluid centre-line (coolant) temperatures.

Figure 4.12 through to Figure 4.28 show the comparisons of average wall temperatures and heat transfer coefficients predicted and computed (in each individual sub-channel) by the twelve (12) different heat transfer correlations namely Bishop [40], Mokry [12], Cheng

et al. [52], Dyadyakin and Popov [55], Onatsky [59], Shitsman [32], Dittus Boelter [51], McAdams [58], Griem [56], Kranoshchekov and Protopopov [62], Gupta [60] and Petukhov [61] with Wataa's numerical data of wall temperatures and heat transfer coefficients (HTCs).

It should be noted that the average wall temperatures and heat transfer coefficients obtained by Wataa were computed using the Bishop Heat transfer correlation [40] based on the Dittus Boelter equation [51] (as shown in Figure 2.23 chapter 2).

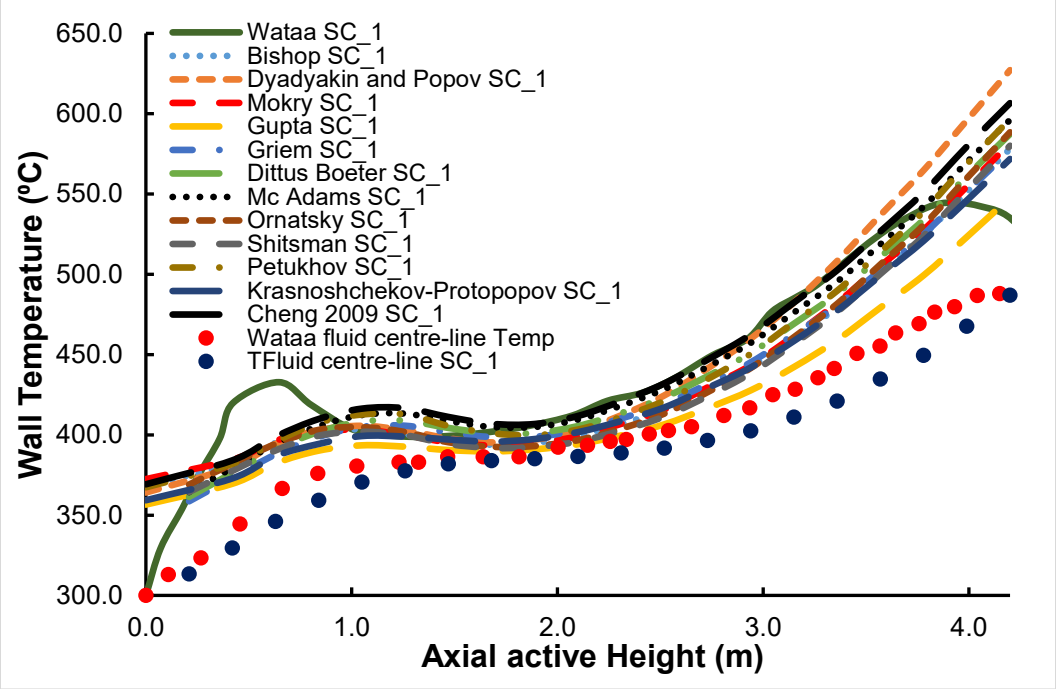

Figure 4.12: Simulation results for selected heat transfer correlations showing the wall temperature profiles in SC 1

Figure 4.12 and Figure 4.13 show comparisons of the wall temperatures and HTCs computed using the twelve selected correlations with that of Wataa's data respectively. In Figure 4.12, it was observed that in the NHT region all the twelve correlations did not closely capture the wall temperatures obtained by Wataa. However, in the enhanced heat

transfer region, most of the correlations closely captured the temperature obtained by Wataa except the Cheng et al., McAdams and Petukhov which slightly overestimated the Wataa's wall temperature.

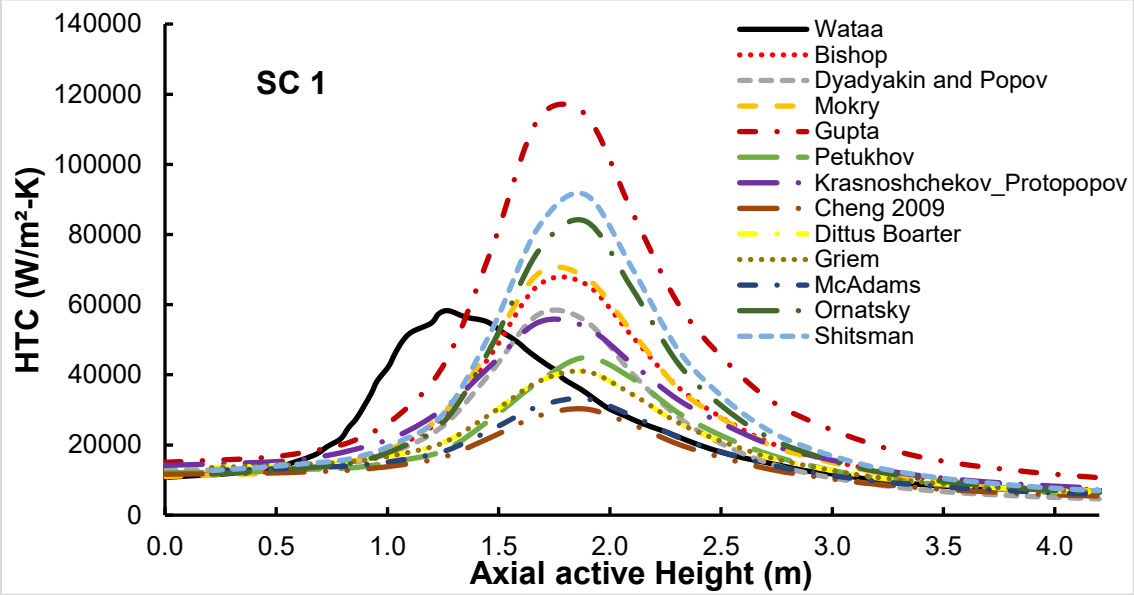

Figure 4.13: Simulation results for selected heat transfer correlations showing the HTC profiles in SC (1)

In the deteriorated heat transfer region the Cheng et al. correlation followed by the McAdams and Dyadyakin and Popov correlations captured closely the Wataa's wall temperature, from 1.7 m to about 3.8 m, except towards the outlet of the sub-channel where wall temperatures obtained by 12 correlations were more than that of Wataa's (Figure 4.12). On the other hand, the Gupta correlation under estimated the wall temperature obtained by Wataa, this was followed by the Shitsman and Onatsky correlations in the HTD region.

In the case of HTCs (Figure 4.13), most of the correlations closely captured the HTC computed by Wataa at the entrance part of the sub-channel. However, there was a shift in

the location of the maximum peaks (between 1.68 m and 2m) for the twelve correlation compared to the HTC computed by Wataa (1.3 m) along the active length of the sub-channel. Beyond 2 m, the Cheng et al. closely captured the Wataa HTC, followed by the McAdams, Dittus Boelter, Griem and Dyadyakin and Popov correlations. The Gupta correlation over-estimated the HTC as observed in Figure 4.13.

The following set of graphical results presents the rest of comparisons of the wall temperature profiles computed by the 12 selected correlations with the wall temperatures obtained Wataa in sub-channels 2 to 9, thus from Figure 4.14 to Figure 4.21.

Figure 4.22 to Figure 4.29 presents also the rest of the comparisons of HTC profiles computed using the 12 selected heat transfer correlations with that of Wataa's in sub-channels 2 to 9.

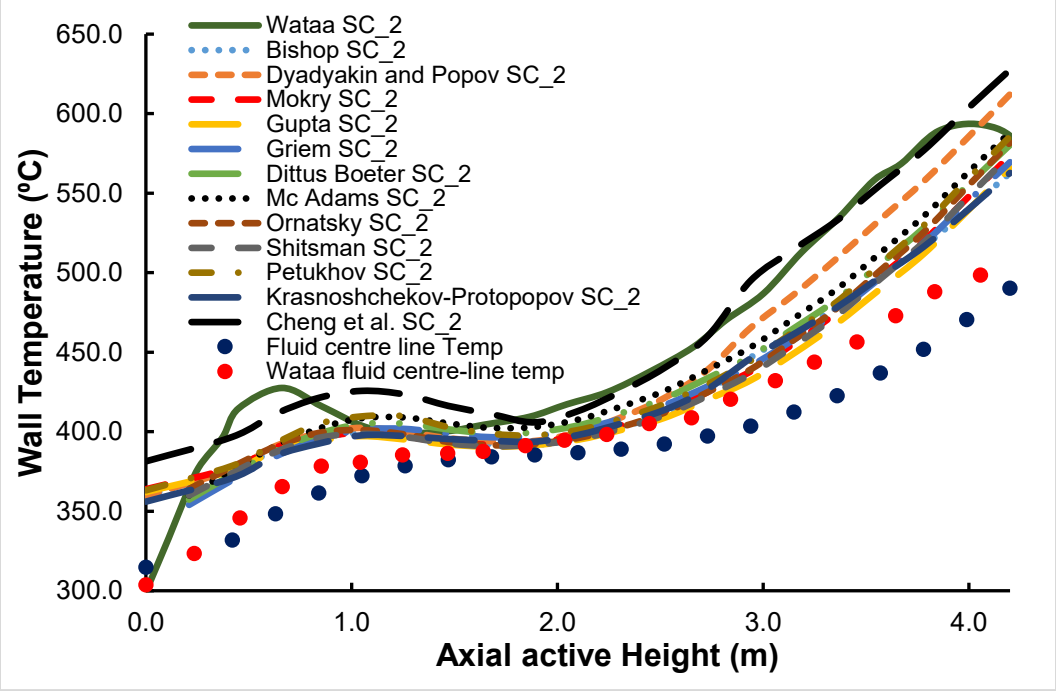

Figure 4.14: Simulation results for selected heat transfer correlations showing the wall temperature profiles in SC 2

Accordingly, it was observed that in all the 9 sub-channels analyzed, the wall temperatures computed by the Cheng et al. correlation [52] consistently and closely captured Wataa's obtained wall temperature in the HTD region from 2.0 m to about 3.8 m along the active length. In sub-channel 2 the Cheng et al. correlation was followed by the Dyadyakin and Popov, McAdam's and Petukhov correlations (Figure 4.14). A similar trend of the estimation of the wall temperatures obtained by Waata by the correlations was also observed in sub-channel 4, however towards the outlet of the sub-channel only the wall temperatures computed by the Cheng et al. and Dyadyakin and Popov correlations were above that of Wataa's in both sub-channel 2 and 4 (Figure 4.14 and Figure 4.16).

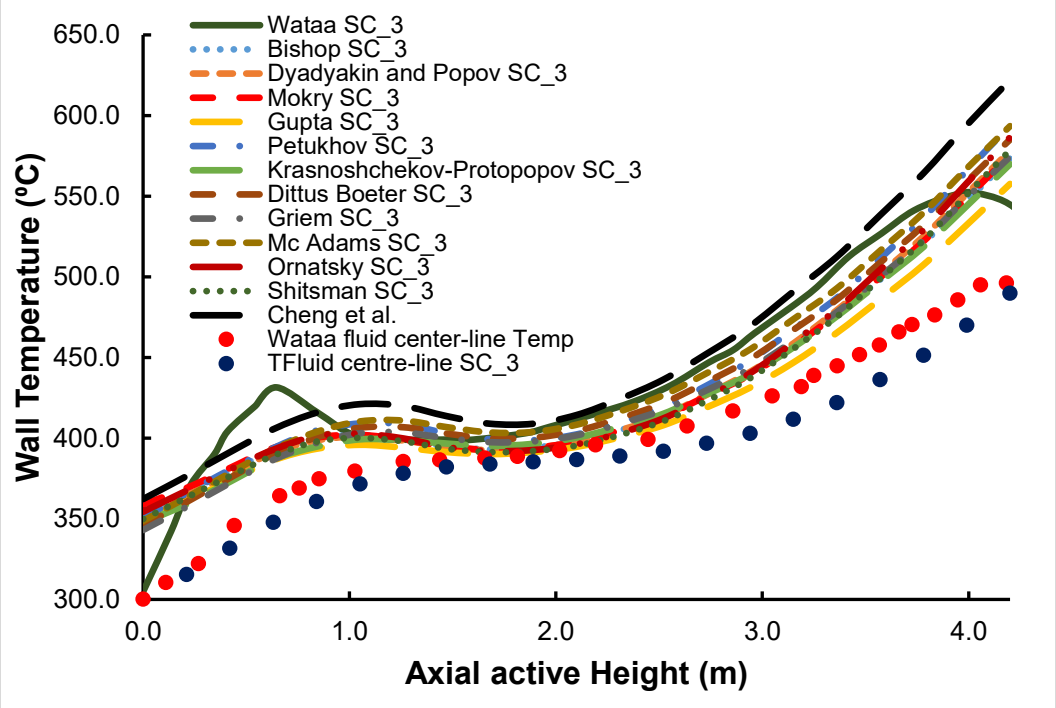

Figure 4.15: Simulation results for selected heat transfer correlations showing the wall temperature profiles in SC 3

In addition, it was also observed that the Cheng et al. correlation overestimated the wall temperature obtained by Wataa in the HTE region, in sub-channels 2, 3 and 4. In sub-

channel 5 (HTE region), the Petukhov and Cheng correlation slightly overestimated the wall temperature obtained by Wataa. Similarly, in sub-channel 6 (HTE region) the Gupta correlation overestimated the wall temperature obtained by Wataa from 1 m to 2.5 m, but under-estimated it in the HTD region (Figure 4.18).

The Gupta, Shitsman, Mokry, Krasnoshchekov and Protopopov correlations under-estimated the wall temperature obtained by Wataa (in the HTD region) in sub-channels 2 and 3. A similar trend was observed in sub-channel 4, except for the Gupta correlation which closely estimated the wall temperatures obtained by Wataa as shown in Figure 4.16.

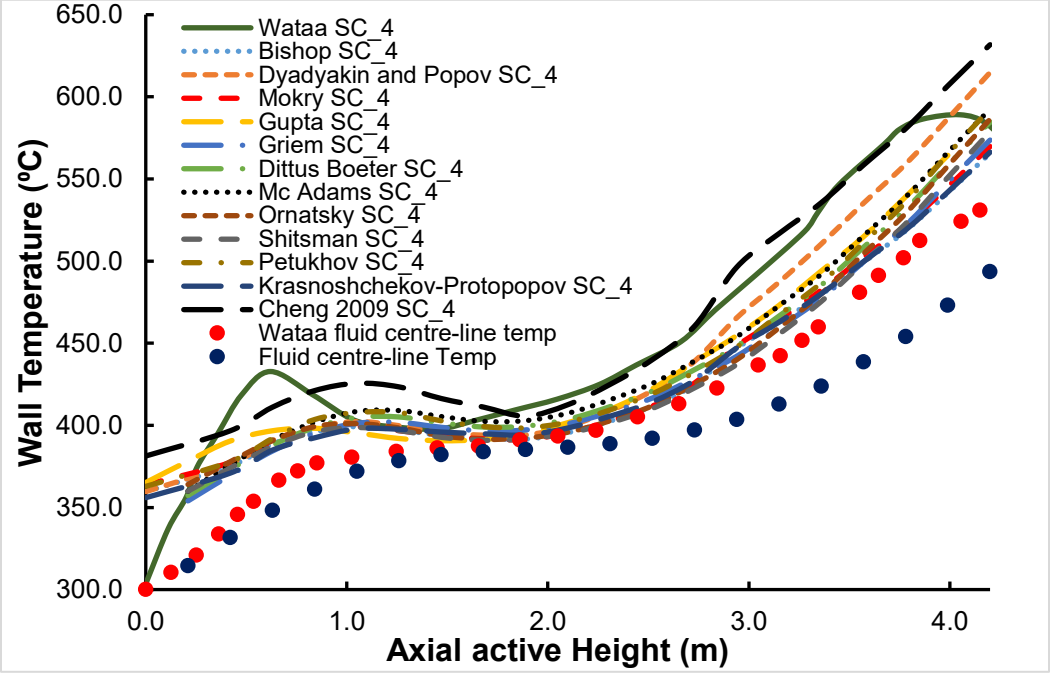

Figure 4.16: Simulation results for selected heat transfer correlations showing the wall temperature profiles in SC 4

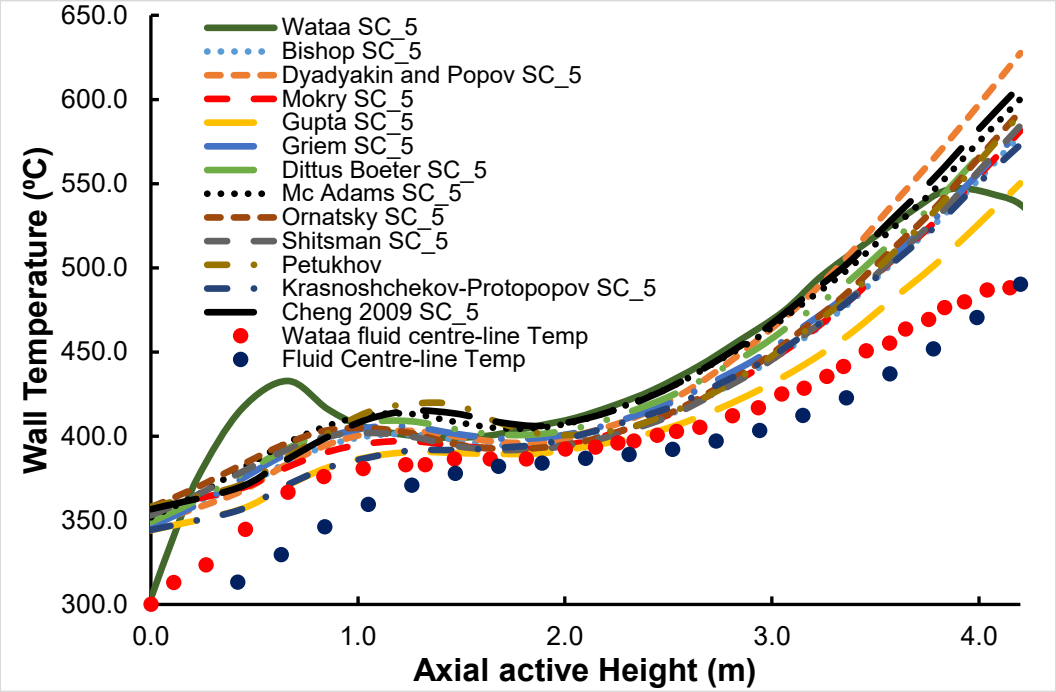

Figure 4.17: Simulation results for selected heat transfer correlations showing the wall temperature profiles in SC (5)

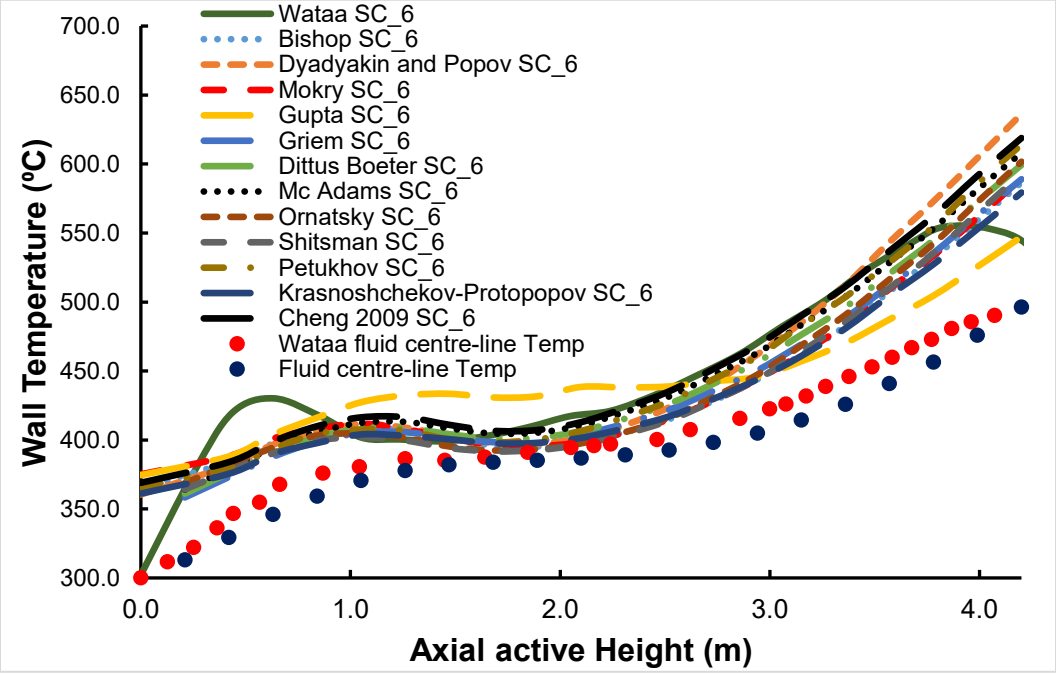

Figure 4.18: Simulation results for selected heat transfer correlations showing the wall temperature profiles in SC 6

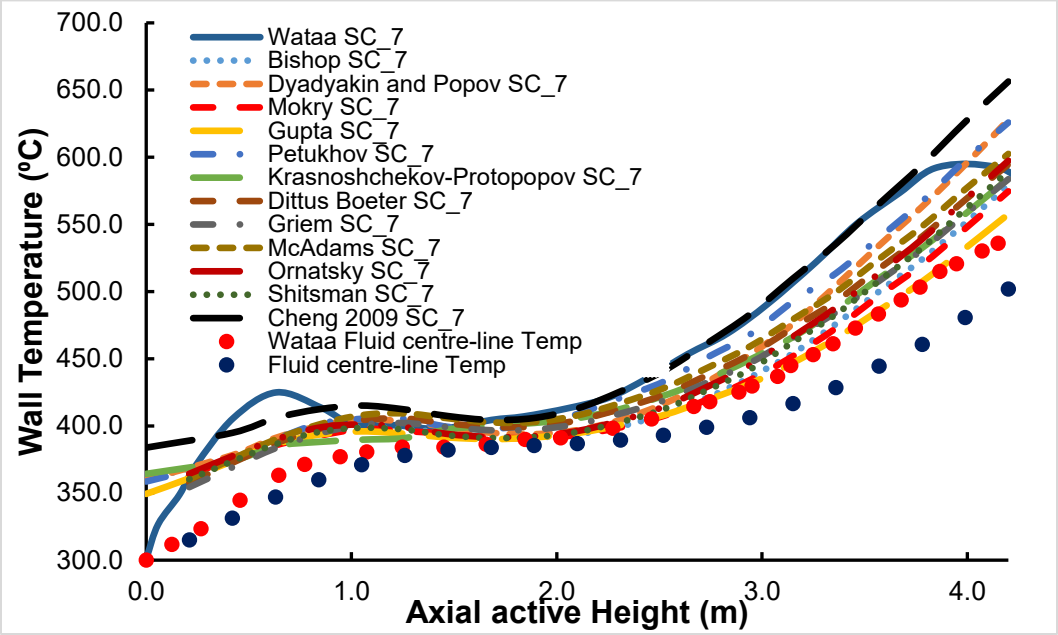

Figure 4.19: Simulation results for selected heat transfer correlations showing the wall temperature profiles in SC 7

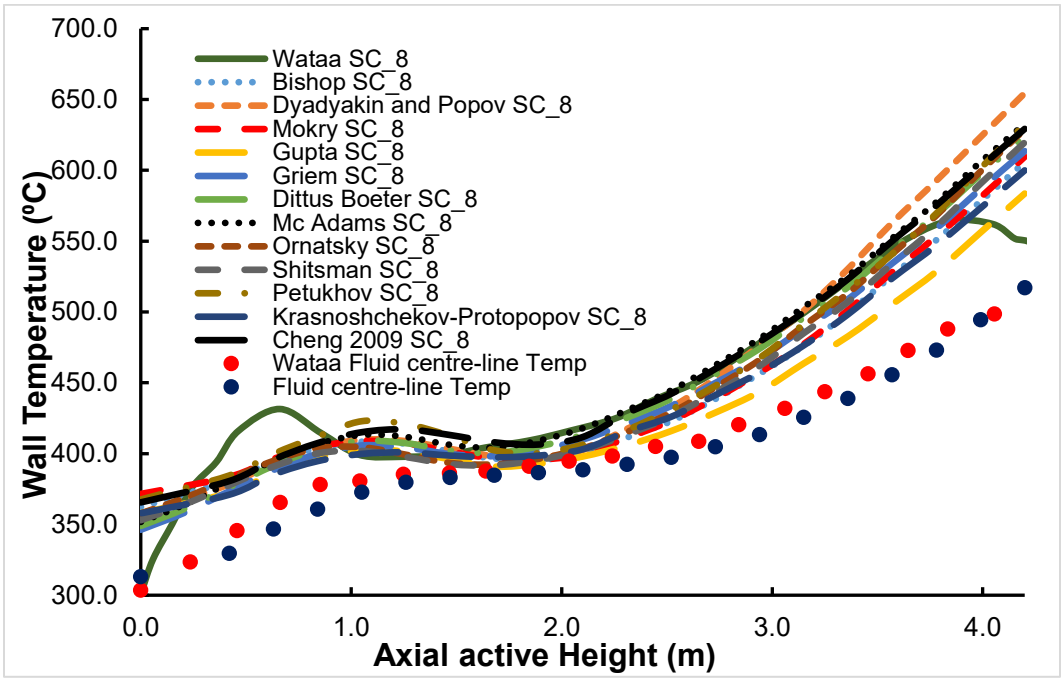

Figure 4.20: Simulation results for selected heat transfer correlations showing the wall temperature profiles in SC 8

In sub-channels 7 and 8, as observed in the other sub-channels the Petukhov and Cheng et al. correlations slightly overestimated the wall temperature obtained by Wataa in the HTE region in sub-channel 7. In the HTD region the result of Cheng et al. correlation agreed with the Wataa's data, from 1.68 m to 3.78 m in sub-channel 7 (see Figure 4.19). However, in sub-channel 8, both the results of Cheng et al and McAdams correlations were in agreement with the Wataa's data in the HTD region (see Figure 4.20). Moreover, in the upper part of the sub-channel, all the wall temperatures computed by the 12 selected correlations in sub-channel 8 were above the wall temperature obtained by Waata. Nevertheless, in sub-channel 7 only the Petukhov, Cheng et al. and Dyadyakin and Popov were above Wataa's wall temperature.

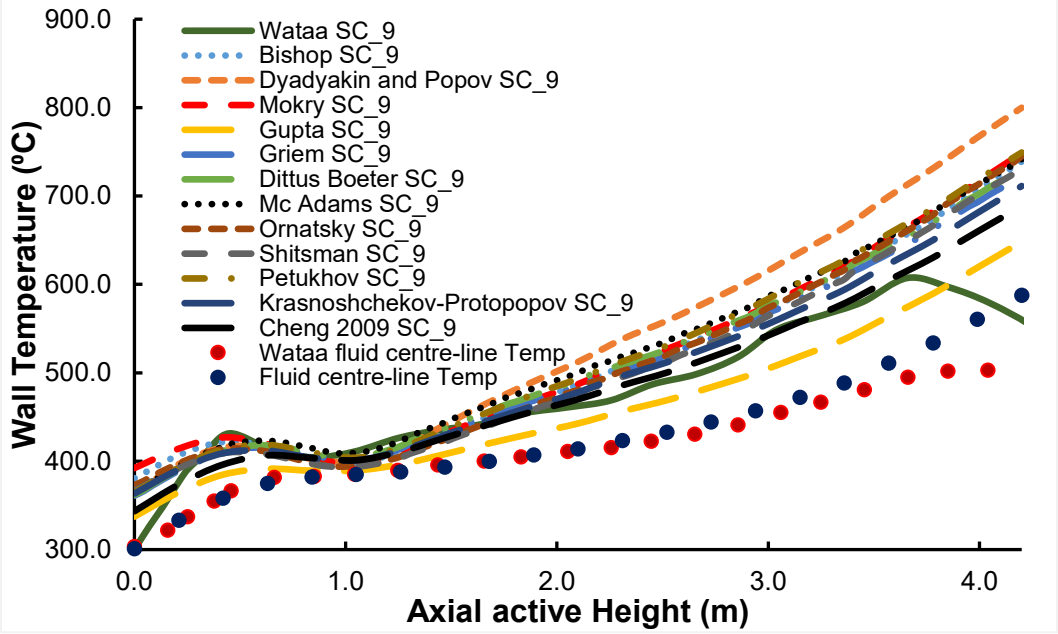

Figure 4.21: Simulation results for selected heat transfer correlations showing the wall temperature profiles in SC 9

Furthermore, for all the nine sub-channels in the NHT region, it was observed that the twelve correlations did not favorably estimate the wall temperature obtained by Wataa. In

sub-channel 9 (HTE region), almost all the correlations captured the wall temperature trend obtained by Wataa, except the Gupta correlation which slightly under-estimated it.

Nevertheless, from the entrance of the sub-channels along the total active height the three heat transfer regimes namely; Normal Heat Transfer (NHT), Heat Transfer Enhancement (HTE) and Heat Transfer Deterioration (HTD) were observed. The normal heat transfer phenomenon was observed from SCs inlet up to 0.8 m near the pseudo critical point, while from 0.8 m to 2.1 m above pseudo-critical point HTE was observed. Beyond 2.1 m along the active height HTD is observed. This phenomenon was attributed to the rapid changes in coolant fluid thermal dynamic physical properties (such as heat capacity, viscosity, density, heat conductivity and enthalpy), displayed in Figure 4.12 and Figure 4.14 through to Figure 4.21. In effect when the wall temperature decreases, the heat transfer coefficient increases, a maximum value of HTC is obtained in the HTE region. Beyond the HTE region heat transfer coefficient tends to decrease.

In general, it was observed that the maximum wall temperature computed slightly exceeds the design allowable limit of 620 °C by an average of 10 °C in SC (2) to SC (6), as captured from Figure 4.12, Figure 4.14 through to Figure 4.21. In sub-channels 7 and 8, the allowable limit temperature was exceeded by 35 °C, while in sub-channel 9 (the hottest SC) the deviation was more than 150 °C as observed in Figure 4.21.

The results for the HTCs in sub-channel 2 to 9 are presented in Figure 4.22 to Figure 4.29. From the beginning of the heated section where the HTC increases gradually is called the NHT region. The region after the NHT region along the heated section where a sharp rise in HTC is observed is called the HTE region. The HTC increases up to its peak in the HTE

region. After the HTE region, the HTC decreases sharply and then gradually after reaching its peak value. The region along the heated section where the HTC decreases is called the HTD region

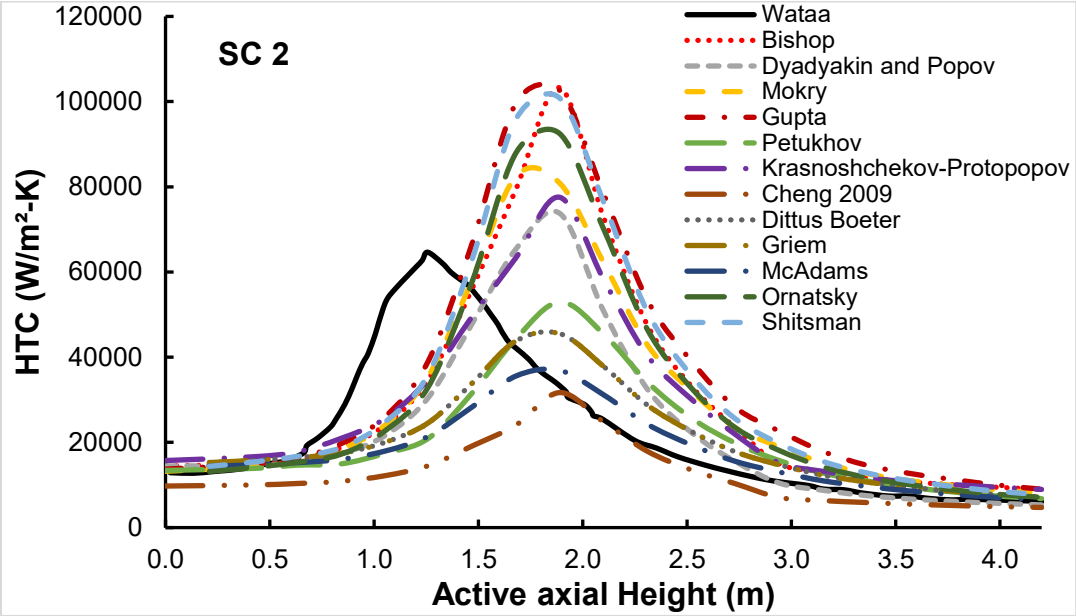

Figure 4.22: Simulation results for selected heat transfer correlations showing the HTC profiles in SC (2)

In sub-channel 2 (Figure 4.22), most of the correlations estimated closely the HTC obtained by Wataa at the inlet part of the sub-channel except the Krasnoshchkov and Protopopov and Cheng et al correlations. In the half part of the sub- channel towards the outlet, the Cheng et al., McAdams and Dyadyakin and Popov correlations closely estimated the HTC obtained by Watta. It was observed that there was a shift in the location of the maximum peak (between 1.7 m and 2 m) for HTCs computed by the twelve different correlations, compared to that of Wataa's (1.2 m). The Cheng et al. had a lowest peak while the Shitsman, Bishop and Gupta correlations had the highest peak in sub-channel 2. The peak

of the Dyadyakin and Popov as well as that of Krasnoshchkov and Protopopov correlations was close the HTC's peak obtained by Wataa.

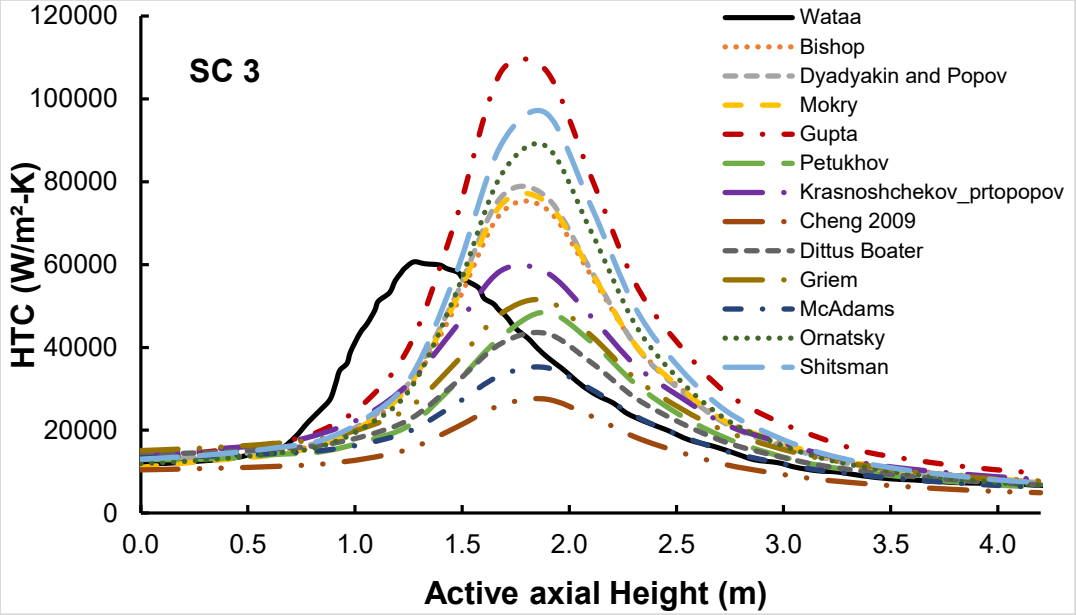

Figure 4.23: Simulation results for selected heat transfer correlations showing the HTC profiles in SC (3)

Accordingly, a similar trend of HTC profile is observed in Figure 4.23 (sub-channel 3), except that the McAdams correlations showed a good agreement with Wataa's computed HTCs at 2 m to 4 m. The Gupta correlation had the highest peak and only the Krasnoshchkov and Protopopov had the same peak height as that of the one obtained by Wataa but at a different location. Figure 4.24 (sub-channel 4) shows a similar trend of results obtained in sub-channel 2, except that the Mokry had a highest peak along with Gupta and Bishop correlations.

Figure 4.25 also shows a similar trend, except that the Cheng et al. and McAdams correlations showed a good agreement with Wataa's computed HTCs at the entrance of the sub-channel and from 2m to 4.2 m. Similarly, only the Gupta correlation had a highest peak

while the Bishop and Kranoshchekov and Protopopov correlations have the similar peak with the Wataa's computed HTC result.

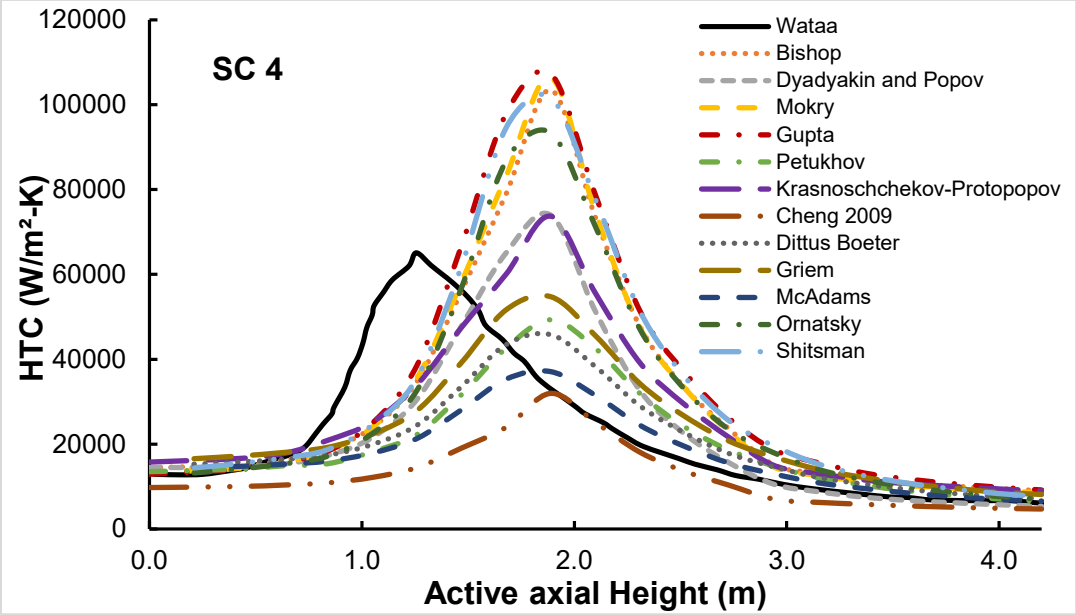

Figure 4.24: Simulation results for selected heat transfer correlations showing the HTC profiles in SC (4)

Figure 4.24 (sub-channel 4) shows a similar trend of results obtained in sub-channel 2, except that the Mokry had a highest peak along with Gupta and Bishop correlations.

Figure 4.25 also shows a similar trend, except that the Cheng et al. and McAdams correlations showed a good agreement with Wataa's computed HTCs at the entrance of the sub-channel and from 2m to 4.2 m. Similarly, only the Gupta correlation had a highest peak while the Bishop and Kranoshchekov and Protopopov correlations have the similar peak with the Wataa's computed HTC result.

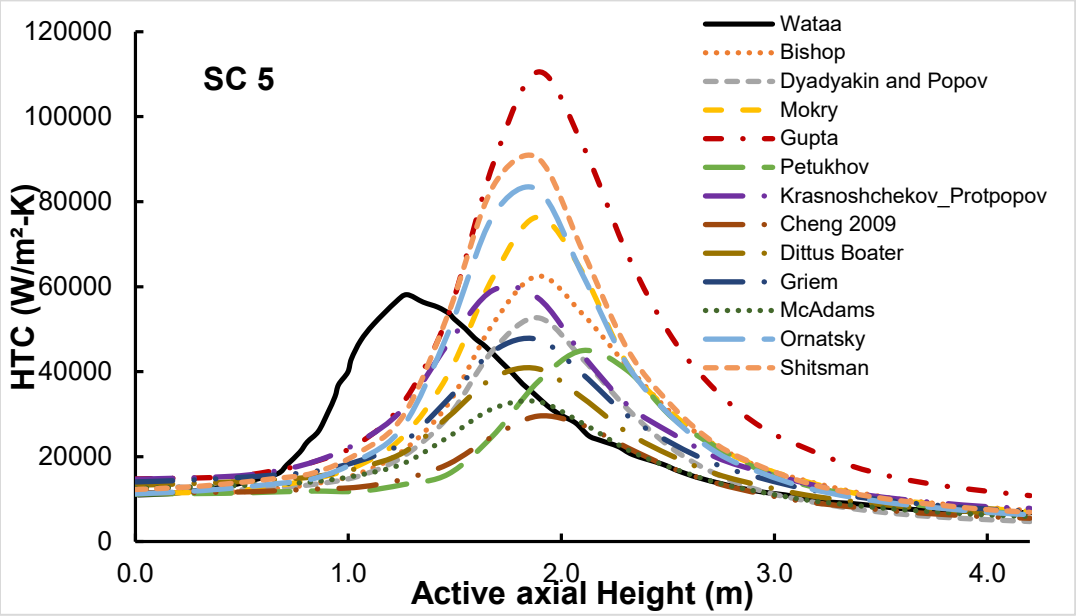

Figure 4.25: Simulation results for selected heat transfer correlations showing the HTC profiles in SC (5)

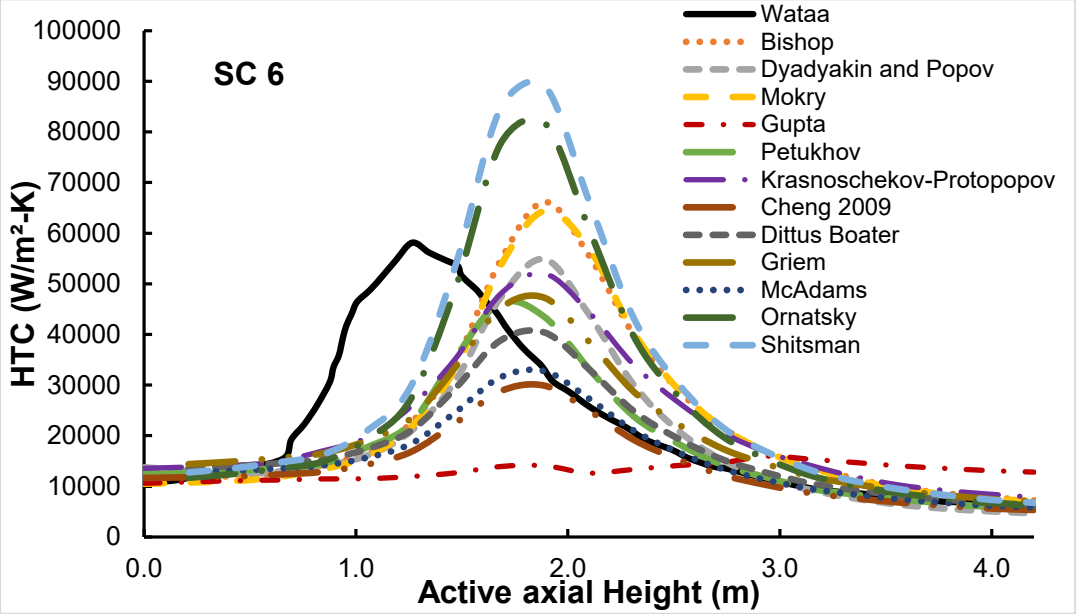

Figure 4.26: Simulation results for selected heat transfer correlations showing the HTC profiles in SC (6)

In addition a similar trend of HTC results was also observed in sub-channel 6 (Figure 4.26) computed using the twelve different correlations and compared with the HTC result obtained by Wataa. The Cheng et al. and McAdams correlations in a similar way, showed a good agreement with HTC result obtained by Wataa at the inlet part of the sub-channel and from 1.8 m to 4.2 m. However, it was observed that the Gupta correlation significantly under estimated the HTC result obtained by Wataa. The Shitsman had the highest peak, while the peak of Dyadyakin and Popov and Kranoshchekov and Protopopov correlations was slightly below that of the one obtained by Wataa but at different locations. The peak of Bishop and Mokry correlations was slightly above the one obtained by Wataa also at a different location.

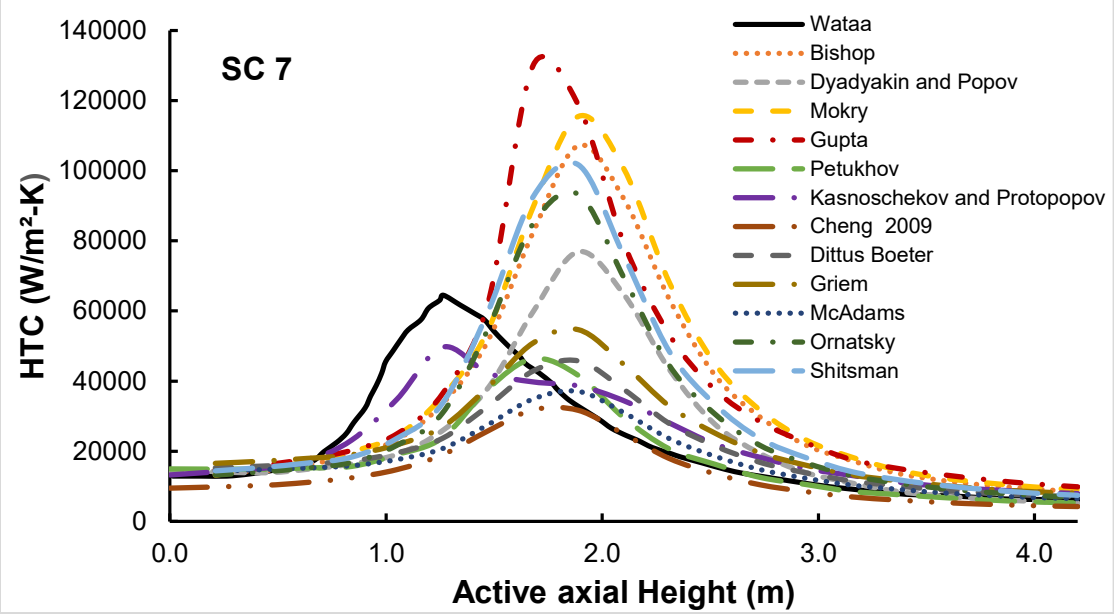

Figure 4.27: Simulation results for selected heat transfer correlations showing the HTC profiles in SC (7)

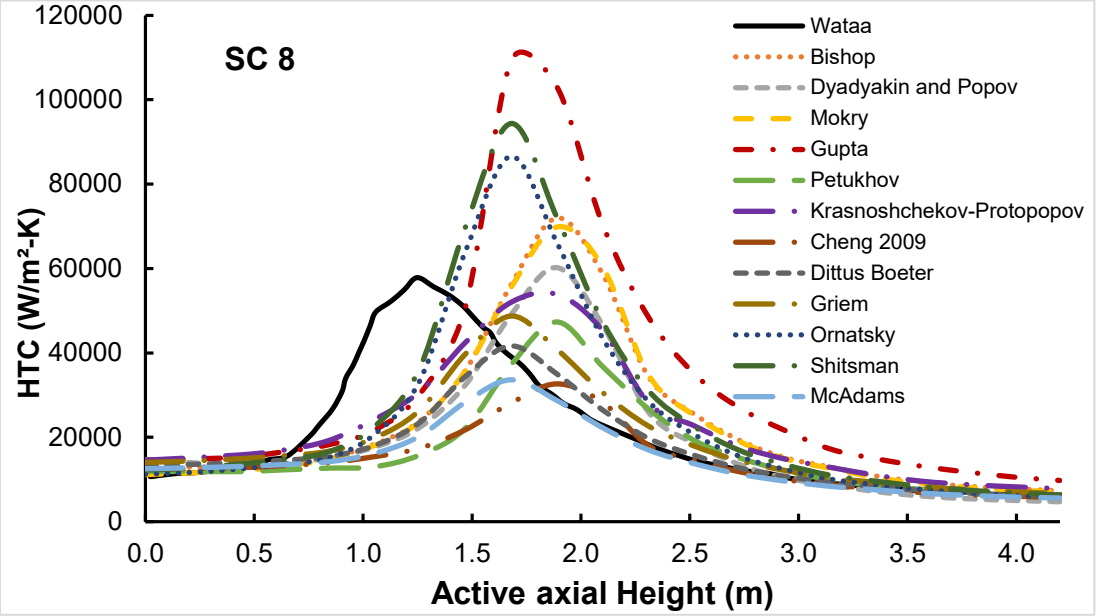

Figure 4.28: Simulation results for selected heat transfer correlations showing the HTC profiles in SC (8)

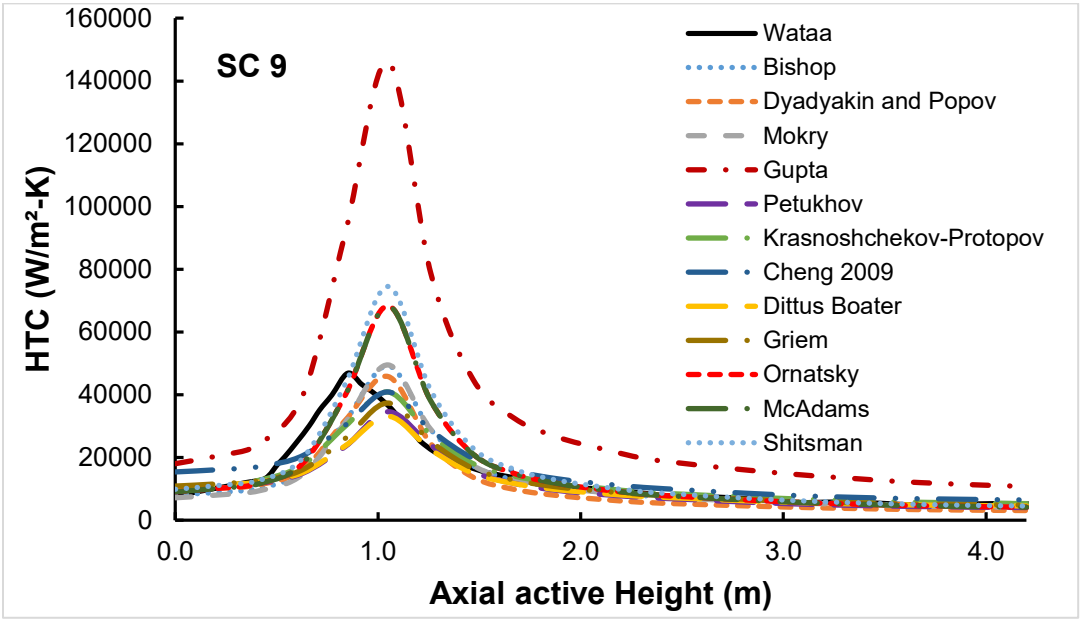

Figure 4.29: Simulation results for selected heat transfer correlations showing the HTC profiles in SC (9)

In Figure 4.27, Figure 4.28 and Figure 4.29 the computed HTC results by twelve (12) different correlations are presented. In Figure 4.27, sub-channel 7 it was observed that the Krasnoshchekov and Proptopopov correlation closely estimated the computed HTC result obtained by Wataa from the entrance of sub-channel up to 1 m. On the other hand, the Cheng et al., Petukhov and McAdams correlation in this sub-channel closely captured the HTC result computed by Wataa at the entrance of the sub-channel and from 2 m to 4.2 m. A similar trend for the Cheng et al. and McAdams correlations was also observed in Figure 4.28 (sub-channel 8), except that Dittus Boelter closely estimated the HTC computed by Wataa from 2 m to 4.2 m. Finally, in sub-channel 9 (Figure 4.29) the Gupta Correlation overestimated the computed HTC result by Wataa. The Dyadyakin and Popov, Bishop and Mokry correlations have a similar peak height with that of the one obtained by Wataa but at different location. Generally, almost the eleven Correlations except the Gupta closely predicted the computed HTC result at higher coolant temperatures above the HTD region (Figure 4.29).

Additionally, there was a shift in the location of the peak for HTCs computed by the twelve different correlations, compared to the Wataa's HTCs. In all the nine sub-channels except in SC (6) the Gupta correlation had the highest peak (see Figure 4.26), this was followed by the Shitsman correlation except in SC (4) (Figure 4.24). The maximum value of the HTC value was 146 kW/m^2 in sub-channel 9 obtained by the Shitsman correlation. It was also observed that the peak location varied between 1.68 m and 2.2 m for 12 selected heat transfer correlations in all the individual sub-channels.

Overall, the Cheng et al. correlation provides the most favorable estimation for the wall temperatures in all the sub-channels and capture closely Wataa's Numerical data. This is

followed by the McAdams correlation, but the Dyadyakin and Popov and the Petukhov also performed well in predicting the numerical data. Dyadyakin and Popov is considered due to the fact that it is specifically designed for the fuel rod bundles, while the Petukhov correlation incorporates the friction factor. The correlations that compared favorably well with the results obtained by Wataa are presented in Table 4.2.

Table 4.2: Chosen Heat Transfer Correlations for Implementation

Reference	Correlation	Flow geometry
Cheng et al. [52]	$Nu_b = 0.023 Re_b^{0.8} Pr_b^{0.33} F, where$ $F = \min(F_1, F_2), \quad F_1 = 0.85 + 0.766(\pi_A \cdot 10^3)^{2.4}$ $F_2 = \frac{0.48}{\left(\pi_{A_{pc}} \cdot 10^3\right)^{1.55}} + 1.21\left(1 - \frac{\pi_A}{\pi_{A_{pc}}}\right) and\ \pi_A = \frac{\beta_b q}{G C_p}$	Tubes (D = 10, 20 mm)
McAdams et al.. [58]	$Nu_b = 0.023 Re_f^{0.8} Pr_f^{0.33} \left(1 + 2.3 \frac{D_{hy}}{l}\right)$	Tubes
Dyadyakin and Popov [55]	$Nu_b = 0.021 Re_b^{0.8} \overline{Pr}_b^{0.7} \left(\frac{\rho_w}{\rho_b}\right)_x^{0.45} \left(\frac{\mu_b}{\mu_{in}}\right)^{0.2} \left(\frac{\rho_b}{\rho_{in}}\right)^{0.1} \left(1 + 2.5 \frac{D_{hy}}{x}\right)$	Bundles (D_{hy} = 2.15–2.77 mm)
Petukhov et al. [61]	$St = \frac{Nu}{Re \cdot Pr} = \frac{(\xi/8)}{12.7\sqrt{(\xi/8)}\left(\overline{Pr}_b^{2/3} - 1\right) + 1 + \frac{900}{Re}}$, $where\ \xi = \frac{1}{(1.82 log Re_b - 1.64)^2} \left(\frac{\rho_w}{\rho_b}\right)^{0.4} \left(\frac{\mu_w}{\mu_b}\right)^{0.2}$	Tubes

To clarify and address the dependence of heat transfer on these effects resulting from the temperature difference between the wall and the core fluid, several dimensionless parameters have been proposed as reported by Wang et al. [65].

Heat transfer coefficient prediction of SCW is challenging due to the steep and non-linear variations in its thermos-physical properties. Near the pseudo-critical point, the density, thermal conductivity and viscosity fall drastically whereas the specific heat experience a sharp peak. It must be noted that due to insufficient and limited data on the most reliable heat transfer correlation providing favorable prediction in the sub-channels, there is still no consistent conclusion on the best performing heat transfer correlation. This leaves room for improvement and modification on the best performing correlations in this analysis.

4.5 Parametric Analysis in Sub-channels 4 and 9 using STAR CCM+ code

Parametric trends for effects of varying the mass flow rate, operating pressure and gravity on the temperature distribution along the active height of the $1/8^{th}$ FA to capture the heat transfer phenomena are evaluated and presented. To perform this analysis the two sub-channels were adopted, SC (4) being the central and having the highest mass flux of 1003.2 $kg/m^2.s$ and SC (9) located at the corner of the fuel assembly with the least mass flux of 510.7 $kg/m^2.s$ (as presented in Appendix A).

4.5.1 The influence of Mass flow rate

The influence of mass flow rate at both 25 MPa and 23 MPa (with pseudo-critical temperatures of 384.9 °C and 377.5 °C respectively) on heat transfer phenomenon are illustrated in Figure 4.30 and Figure 4.31 respectively.

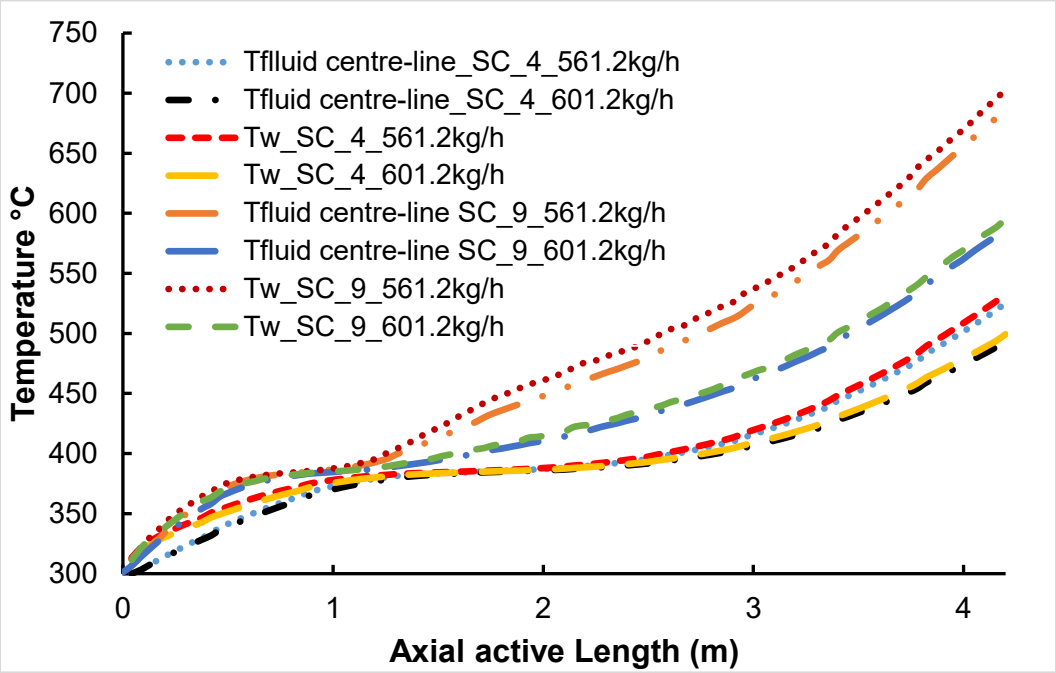

Figure 4.30: Influence of Mass flow rate at P 25 MPa in SCs (4) and (9)

The analysis was carried out at mass flow rates of 0.1670 kg/s (601.2 kg/h) and 0.1559 kg/s (561.2 kg/h), 300 °C as inlet temperature and 650 kW/m^2 heat flux. The profiles of wall temperature values at 25 MPa and 23 MPa were obtained for normal heat transfer, enhanced heat transfer and the deteriorated heat transfer regions in Figure 4.30 and Figure 4.31. In sub-channel 4 (NHT region) the wall temperature values for the 561.2 kg/h mass flow rate were larger than that of the 601.2 kg/h. However, in the enhanced heat transfer region the wall temperature values were almost the equivalent for all the two mass flow rates of the system at 25 MPa and 23 MPa. In the deteriorated region the wall temperature values for 561.2 kg/h mass flow rate were larger than that of the 601.2 kg/h. A similar trend of wall temperature values was observed in sub-channel 9 for the enhanced and deteriorated

heat transfer regions, except for the NHT region where the wall temperature values for all the two mass flow rates at 25 MPa and 23 MPa were almost same.

On the other hand, it was observed that both fluid centre-line temperature values for all the two mass flow rates in sub-channel 4 increased "linearly" below and beyond the pseudo-critical region, while in the pseudo-critical region the fluid centre-line temperature flattened. The fluid centre-line temperature values for the 561.2 kg/h were higher than that of the 601.2 kg/h but almost in the same pseudo-critical region in both sub-channels at 25 MPa and 23 MPa.

The highest wall temperature obtained is 695.86 °C in SC (9) at low mass flow rate (561.2 kg/h) while the least wall temperature is 499.34 °C in SC (4) at high mass flow rate (601.2 kg/h).

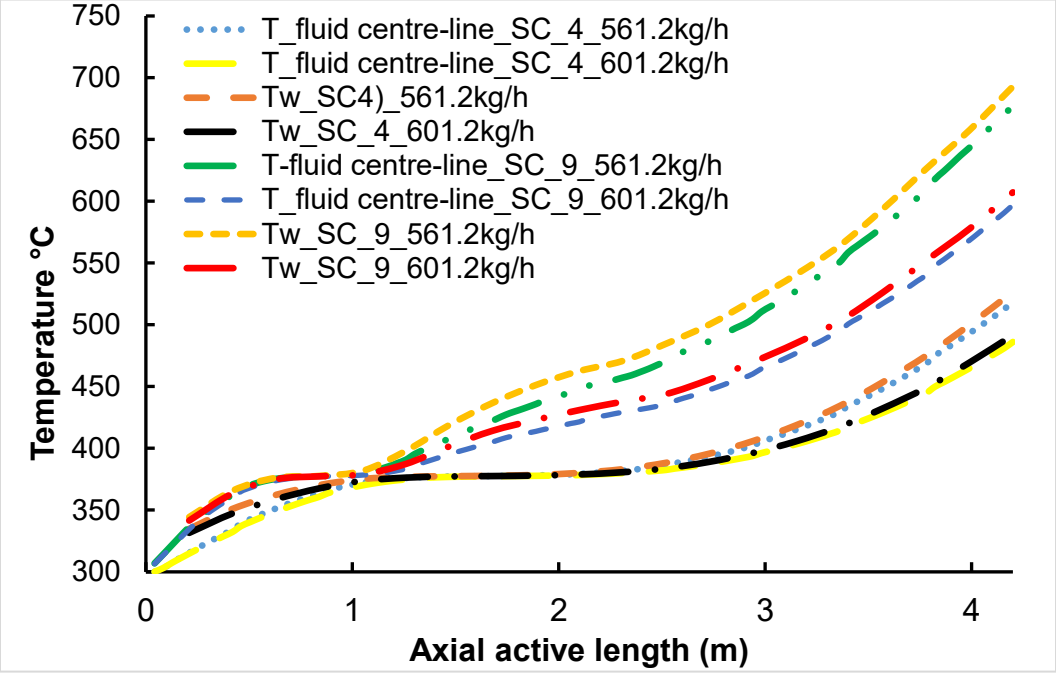

Figure 4.31: Influence of Mass flow rate at P 23 MPa in SCs (4) and (9)

Furthermore, at NHT region the temperature difference between the fluid centre-line temperatures and the average wall temperatures is slightly large in SC (4), very small in the HTE region near the pseudo-critical point and slightly increases beyond the pseudo-critical region, in the HTD. In SC (9), the difference is small at NHT region for both mass flow rates, but increases at low mass flow rate in the HTD region while at a higher mass flow rate the difference is small (see Figure 4.30). A similar trend is also observed at 23 MPa. This can be attributed to the size of an individual sub-channel and strong variations in thermal physical properties of SCW near, at and after the pseudo-critical region.

Figure 4.31 shows the similar trend of the temperature distribution in the two SCs (4) and (9). The highest wall temperature obtained is 692.88 °C in SC (9) at low mass flow rate while the least wall temperature is 491.63 °C in SC (4) at high mass flow rate.

4.5.2 The influence of Pressure

Figure 4.32 and Figure 4.33 respectively show the influence and effect of varying the two system pressures 25 MPa and 23 MPa at the two mass flow rates of 601.2 kg/h and 561.2 kg/h, on heat transfer behaviour in the FA based on the fluid centre-line temperature and wall temperature.

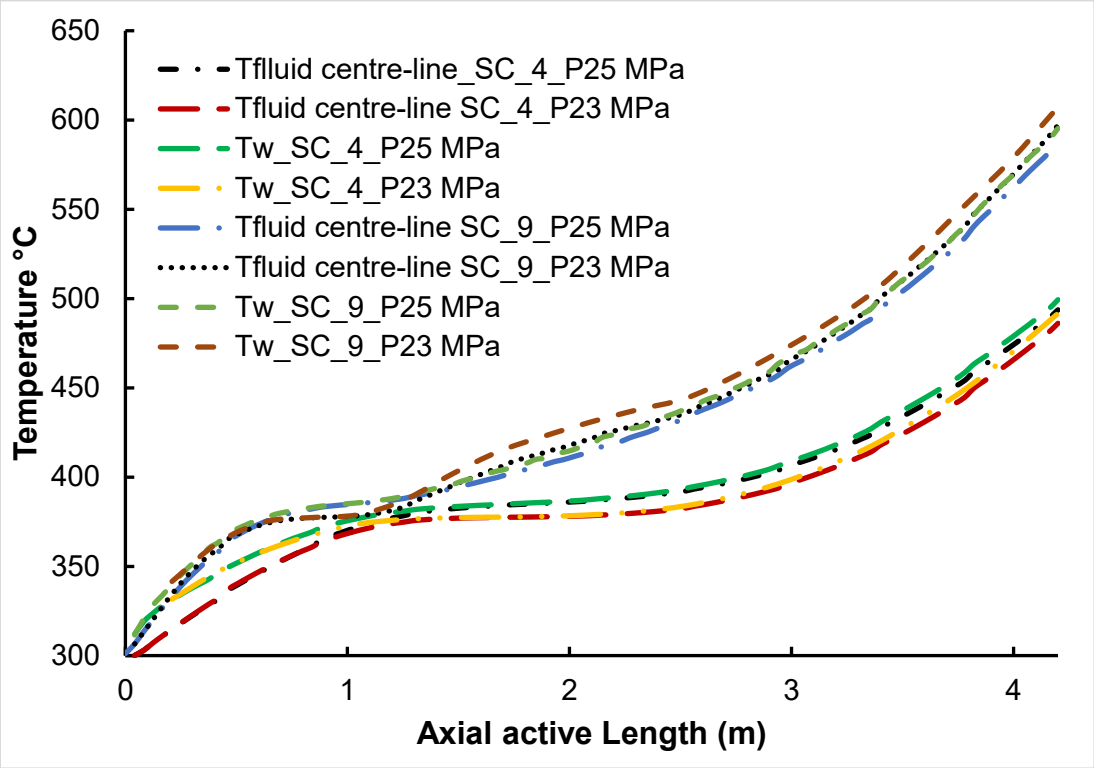

Figure 4.32: Influence of Pressure at 0.1670 kg/s (601.2 kg/h) in SCs (4) and (9)

The simulation results showed that the general trend pattern of the wall and fluid centre-line temperatures under the two different mass flow rates (601.2 kg/h and 561.2 kg/h) behaved almost the same. Nevertheless, in Figure 4.32, below the pseudo-critical region the temperature values for 23 MPa and 25MPA in sub-channel 4 at 601.2 kg/h mass flow rate are the same. However, in and beyond the pseudo-critical region the values of fluid centerline temperature for 25 MPa are relatively larger than that of 23 MPa. A similar trend was observed in sub-channel 9 below the pseudo-critical region, and in the pseudo-critical region, except beyond pseudo-critical region where the values of the fluid centre-line temperature for 23 MPa are larger than that of the 25 MPa.

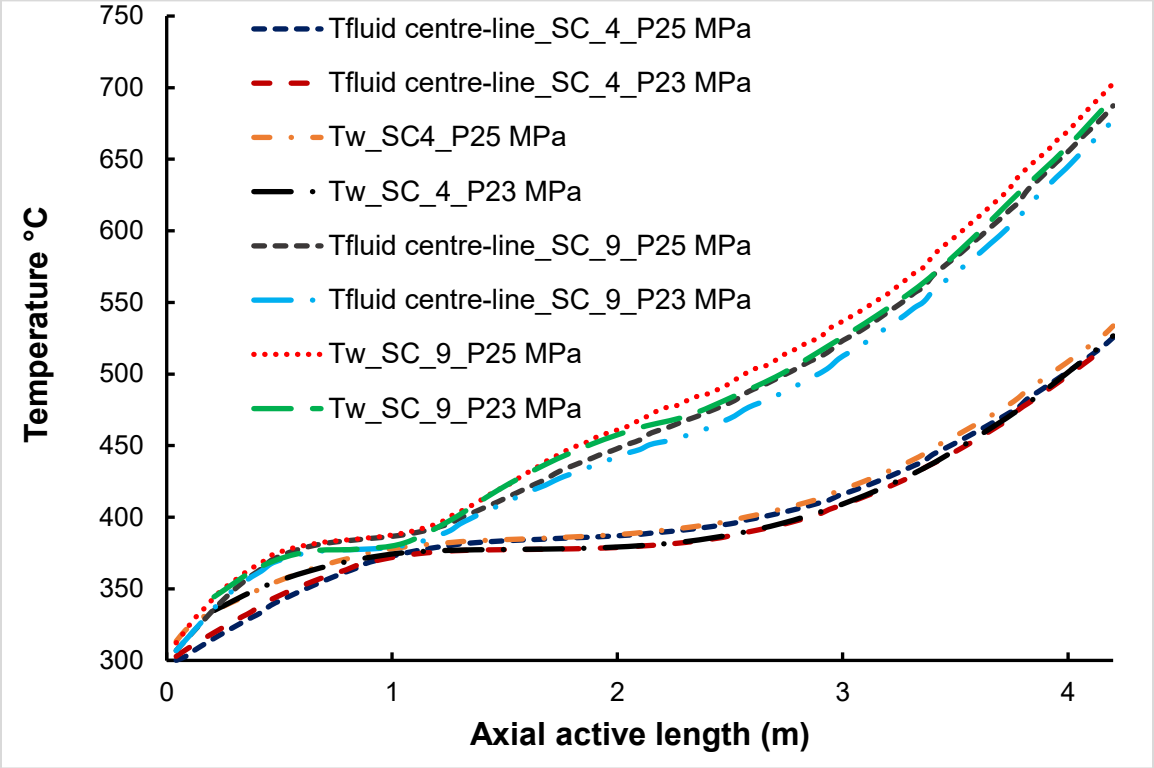

Figure 4.33: Influence of Pressure at 0.1559 kg/s (561.2 kg/h) in SCs (4) and (9)

At 561.2 kg/h in sub-channel 4 (Figure 4.33), the values of the fluid centre-line temperature below the pseudo-critical region for both 23 MPa and 25 MPa were almost the same, while in the pseudo-critical region the fluid centre line temperature values for 25 MPa were relatively larger as compared to that of 23 MPa. Beyond pseudo-critical region the values of the fluid centre line temperature for 25 MPa are slightly larger as compared to that of 23 MPa and became the same towards the exit of the sub-channel. In sub-channel 9, the values of the fluid centre line temperature for 23 MPa and 25 MPa below pseudo-critical region are the same, while in the pseudo-critical region and beyond the pseudo-critical region the values of the fluid centre line temperature for 25 MPa were relatively larger as compared to that of the 23 MPa.

The three heat transfer regimes NHT, HTE and HTD were observed for wall temperature values at both working pressures. It was observed that pressure had no effect in the normal heat transfer region at both 601.2 kg/h and 561.2 kg/h mass flow rates. The wall temperature values in the enhanced heat transfer region increased with pressure for all the two mass flow rates. In sub-channel 4, the wall temperature values for 25 MPa were relatively larger as compared to that of the 23 MPa in the enhanced and deteriorated heat transfer regions at 601.2 kg/h and 561.2 kg/h. In sub-channel 9, the wall temperature values in the enhanced heat transfer region for 25 MPa were relatively larger as compared to that of the 23 MPa for both mass flow rates. However in the deteriorated heat transfer region a different trend of wall temperature values was observed "at 601.2 kg/h the wall temperature values for 23 MPa were larger than that of 25 MPa". But at 561.2 kg/h the wall temperature values for 25 MPa were significantly larger as compared to that of the 23 MPa. It was also observed that between 1.2 m and 2 m, the wall temperature values for 25 MPa and 23 MPa were the same in the deteriorated heat transfer region at 601.2 kg/h, in sub-channel as shown in Figure 4.32.

4.5.3 The influence of Gravity

Figure 4.34 and Figure 4.35 show the influence of gravity on heat transfer based on the wall and fluid centre-line temperature profiles. The analysis was conducted at 25 MPa and 23 MPa working pressures, 300 °C inlet temperature and mass flow rate of 601.2 kg/h.

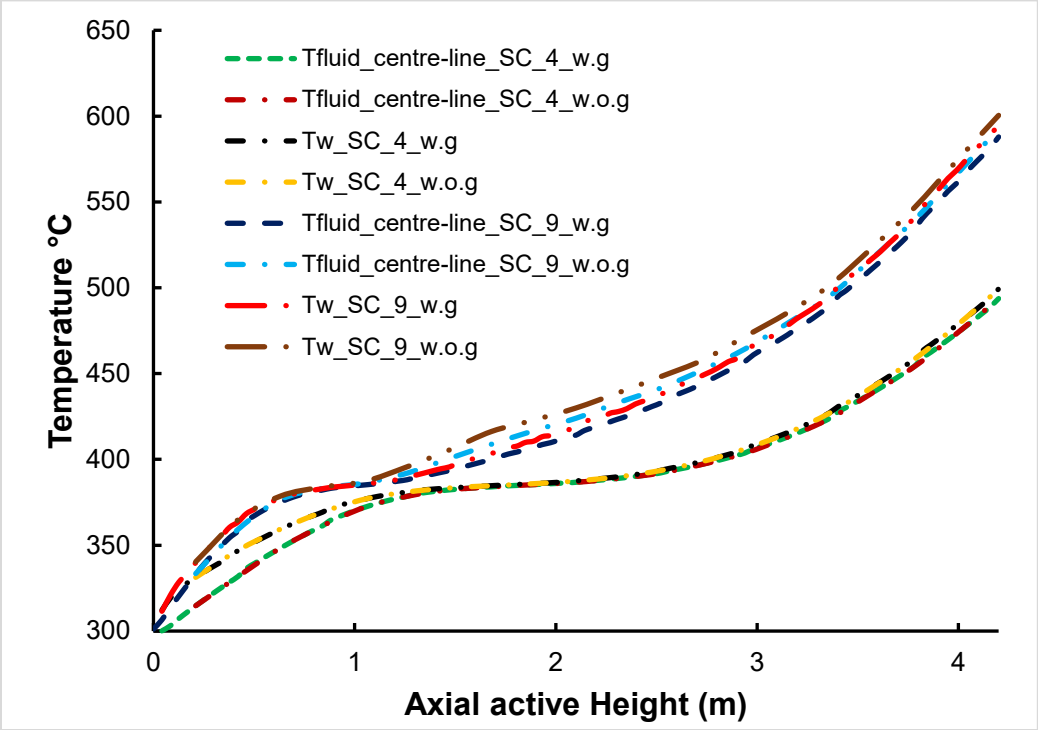

Figure 4.34: Influence of gravity at Pressure 25 MPa and 0.1670 kg/s (601.2 kg/h) as mass flow rate in SCs (4) and (9)

***N.B**: w.g is with gravity and w.o.g is without gravity*

At both 25 MPa and 23 MPa almost equivalent trends and the values for wall temperature for the normal heat transfer, enhanced and deteriorated heat transfer regions were obtained for the systems with or without gravity in sub-channel 4. However, except in sub-channel 9 the wall temperature values for the system without gravity effect were moderately larger as compared to the one with gravity effect in the deteriorated heat transfer region at both 25 MPa and 23 MPa. The occurrence of recovery from deteriorated heat transfer region was observed in the system without gravity at 23 MPa. On the other hand, the trends and values of the fluid centre line temperatures for the two systems were same in sub-channel 4, but in sub-channel 9 the fluid centre line temperature for a system without gravity was larger than the one with gravity beyond pseudo-critical region.

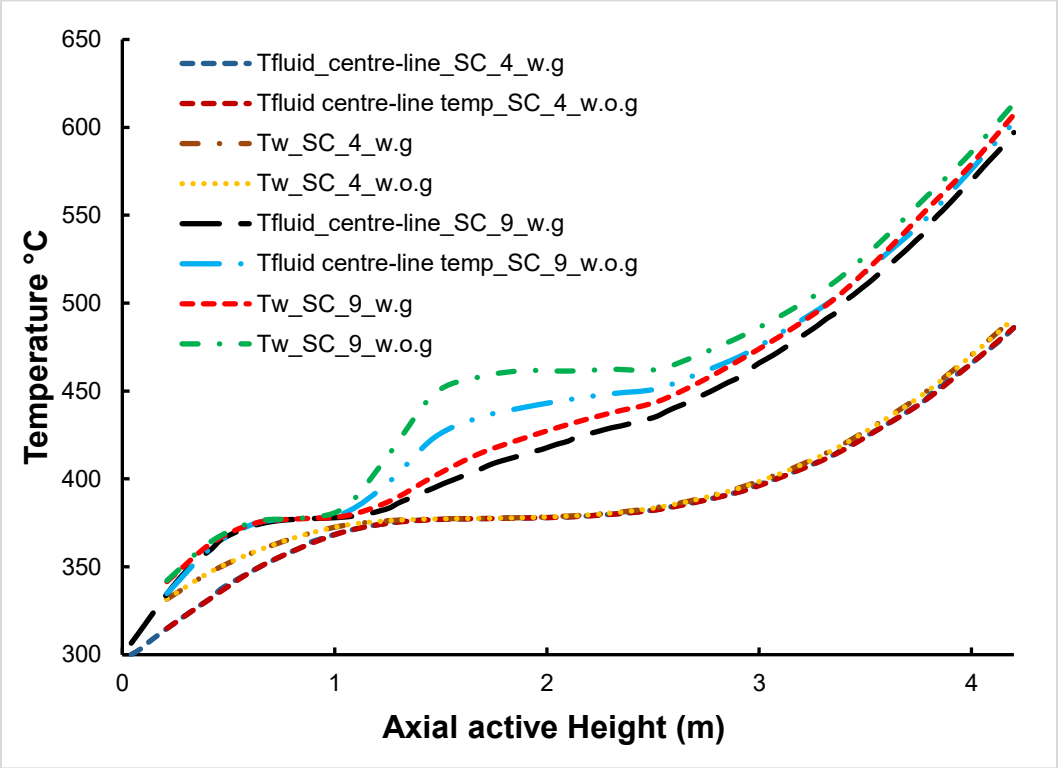

Figure 4.35: Influence of gravity at Pressure 23 MPa (at mass flow rate 0.1670 kg/s (601.2 kg/h) in SCs (4) and (9)

It was also observed that the values of the fluid centre line temperature below and beyond the pseudo-critical region increased linearly, but flattened at the pseudo-critical region. The effect of gravity was more pronounced in sub-channel 9 than in sub-channel 4 at both working pressures of 25 MPa and 23 MPa.

Consequently, based on the parametric analysis carried out, sub-channel 4 performed better in terms of heat transfer because temperatures predicted in sub-channel 9 were higher than the ones obtained in sub-channel 4. Sub-channel 9 was the hottest sub-channel while sub-channel 4 was the coldest sub-channel.

CHAPTER FIVE : CONCLUSION AND RECOMMENDATIONS

5.1 Conclusion

The STAR CCM+ CFD code was used to simulate the flow and heat transfer behaviour of supercritical water in the nine (9) sub-channels of 1/8th FA. Four selected turbulence models were assessed and tested namely, AKN κ–ε, Lien's Lo-Re κ–ε, standard (Wilcox) κ-ω and SST κ–ω. Among the four assessed turbulence models, the Shear Stress Transport and Standard Wilcox κ-ω turbulence models with the low y+ wall treatment qualitatively captured closely the coolant flow and temperature distributions in all the nine sub-channels obtained by Wataa. However, due to the fact that some modifications and improvements made to the Wilcox' Standard κ-ω model was not validated. The SST κ-ω model was chosen to carry out the subsequent simulations. In addition, SST κ-ω turbulence model has also been widely used and recommended by many researchers in studying heat transfer phenomena of supercritical fluids SCWR technology. In the assessment and analysis of the twelve (12) selected different types of heat transfer correlations using SST κ-ω turbulence model, the Cheng et al. correlation consistently captured Wataa's obtained data and provided favorable results. This was followed by the McAdams, Dyadyakin and Popov and Petukhov correlations. The maximum wall temperature was obtained in sub-channel 9, the hottest sub-channel and exceeded the design limit 620 °C by 60 °C for the Cheng correlation while for the other correlations it was more. The difference in temperature between the hottest and coldest sub-channels was approximately 80 °C.

Results obtained from the parametric analysis in the two adopted sub-channels (4 and 9) showed that the fluid centre line temperature linearly increased below and above the

pseudo-critical region, but flattened at the pseudo-critical region for all the system parameters considered. The mass flow rate, pressure and gravity have effects and influence on the wall temperature values in the normal heat transfer region, enhanced heat transfer region and deteriorated heat transfer region. The variation of the system parameters (mass flow rate and gravity) in the enhanced heat transfer and pseudo-critical regions showed no significant difference in the wall temperature and fluid centre line temperature values respectively. However, for the pressure parameter a significant difference in the wall temperature and fluid centre line temperature values was observed. In addition, the wall and fluid centre line temperature values increased with pressure in these regions. This numerical study was not quantitatively compared with experimental data along the axial active heights of the sub-channels. Nonetheless, it was observed that the adopted numerical tool STAR-CCM+ code showed capabilities of capturing the trends for the normal heat transfer, enhanced and deteriorated heat transfer regions.

Based on the parametric analysis carried out, sub-channel 4 performed favorably better in terms of heat transfer in that temperatures predicted in sub-channel 9 where higher than the ones obtained in sub-channel 4. Sub-channel 9 was the hottest sub-channel while sub-channel 4 was the coldest sub-channel.

Accordingly, from the deduced findings, experimental investigation should be carried out to validate the results and ascertain the applicability of the SST κ-ω turbulence model with low y^+ wall treatment at supercritical conditions in SCWR fuel assembly.

5.2 Recommendations

The following are the recommendations made from the numerical analysis conducted using STAR CCM+ CFD code for the SCWRs:

- Experimental investigations involving rod bundles adopted in this study should be conducted to validate the results obtained numerically and address the inconsistence of conclusions drawn so far. These experimental studies would also be helpful in validating similar numerical studies in future.
- More heat transfer related studies in rod bundle geometry with more than 2×2 fuel rod bundles should be carried out. This will provide more data on rod bundle geometry and better understanding on heat transfer in rod bundles.
- More heat transfer correlations should be developed for predictions at supercritical pressures. Currently, most of the existing heat transfer correlations were developed for predictions at subcritical pressures.

References

[1] Mori M., "Core design analysis of the supercritical water fast reactor," FZKA-Scientific Report, 2005.

[2] Lake James A., Ralph G. Bennett, John F. Kotek., "Next-generation nuclear power," *Scientific American,* vol. 286(1), pp. 72-81, 2002.

[3] Buongiorno J., & MacDonald P, "Supercritical water reactor (SCWR). Progress Report for the FY-03 Generation-IV R&D Activities for the Development of the SCWR in the US," INEEL/Ext-03-03-01210, INEEL, USA, September, 2003.

[4] Mori H., Kaida T., Ohno M., Yoshida S., Hamamoto Y.,, "Heat transfer to a supercritical pressure fluid flowing in sub-bundle channels," *Journal of Nuclear Science and Technology,* vol. 49, no. 4, pp. 373-383, 2012.

[5] Hofmeister, J., Waata, C., Starflinger, J., Schulenberg, T., Laurien, E.,, "Fuel assembly design study for a reactor with supercritical water," *Nucl. Eng. Des.,* vol. 237, p. 1513–1521, 2007.

[6] Schulenberg, T., Starflinger, J., Marsault, P., Bittermann, D., Maráczy, C., Laurien, E., LycklamaàNijeholt, J.A.,Anglart, H., Andreani, M., Ruzickova,M., Toivonen, A.,, "European supercritical water cooled reactor.," *Nucl. Eng. Des.,* vol. 241, pp. 3505-3513., 2011.

[7] Schulenberg T, Leung K.H.L., Oka Y.,, "Review of R&D for supercritical water cooled reactors," *Progress in Nuclear Energy ,* vol. 77 , pp. 282-299, (2014) .

[8] Cheng, X., Schulenberg, T., Bittermann, D., Rau, P., , "Design analysis of core assemblies for supercritical pressure conditions," *Nucl. Eng. Des. ,* vol. 223, p. 279–294, 2003.

[9] Pioro I., "Joint ICTP-IAEA Course on Science and Technology of Supercritical Water Cooled Reactors," 2011. [Online]. Available: http://indico.ictp.it/event/a10196/session/4/contribution/4/material/0/0.pdf. [Accessed 25 February 2018].

[10] Jiang K.,, "An Experimental Facility for Studying Heat Transfer in Supercritical Fluids," (Doctoral dissertation,Université d'Ottawa/University of Ottawa), Ottawa, 2015.

[11] Fewster, J., "Mixed forced and free convective heat transfer to supercritical pressure fluids flowing in vertical pipes," University of Machester, Manchester, 1976.

[12] Mokry S., Pioro I.L., Farah A., et al.,, "Developing of supercritical water heat-transfer correlation for vertical bare tubes," *Nucl. Eng. Des.,* vol. 241, pp. 1126-1136, 2011.

[13] Reiss T., Csom Gy., Fehe´r S., Czifrus Sz., "The Simplified Supercritical Water-Cooled Reactor (SSCWR), a new SCWR design," *Progress in Nuclear Energy,* vol. 52, p. 177–189, 2010.

[14] Dobashi, K., Oka, Y., Koshizuka, S.,, "Conceptual Design Of A High Temperature Power Reactor Cooled And Moderated By Supercritical Light Water.," vol. 25, p. 487–505, 1998.

[15] Yamaji A., Kamei K., Oka Y., Koshizuka S.,, "Improved core design of the high temperature supercritical-pressure light water reactor," *Annals of Nuclear Energy,* vol. 32, no. 7, pp. 651-670, 2005a.

[16] Hofmeister, J., Schulenberg, T., Starflinger, J.,, "Optimization of a fuel assembly for a HPLWR," in *ICAPP 05*, Seoul Korea, May 15–19, 2005.

[17] Waata C.L., "Coupled Neutronics/Thermal-Hyhdraulics Analysis of a High Performance Light Water Reactor Fuel Assembly," 2006.

[18] Policy Group, "GIF Annual Report," OECD Nuclear Energy Agency, 2016.

[19] DOE-US, "Nuclear Energy Research Advisory Committee and the Generation IV International Forum," A Technology Roadmap for Generation IV Nuclear Energy Systems, 2002.

[20] Vujic J., Greenspan E. H. U. D., & Milosevic M.,, "New reactor concepts for new generation of nuclear power in the USA: An overview.," 2005.

[21] Pioro I.L., Duffey R.B.,, "Heat transfer and hydraulic resistance at supercritical pressures in power engineering applications," *ASME Press ,* 2007.

[22] Kamei, K., Yamaji, A., Ishiwatari, Y., et al.,, "Fuel and core design of super light water reactor with low leakage fuel loading pattern.," *Journal of Nuclear Science and Technology,* vol. 43, p. 129–139., 2006..

[23] Maráczy C., Hegyi G., Hordósy G., et al.,, "HPLWR equilibrium core design with the KARATE-code system.," *Journal of Progress in Nuclear Energy,* vol. 53, p. 267–277, 2011.

[24] Zhao M., Gu H.Y., Cheng X., "Experimental study on heat transfer of supercritical water flowing downward in circular tubes," *Annals of Nuclear Energy,* vol. 63, p. 339–349, 2013.

[25] Liu, L., Xiao, Z., Yan, X., Zeng, X., Huang, Y.,, "Heat transfer deterioration to supercritical water in circular tube and annular channel," *Nucl. Eng. Des,* vol. 255, p. 97–104, 2013.

[26] LIU X., and CHENG X., "Steady-state thermal-hydraulic analysis of SCWR assembly," *Energy Power Eng. China,* vol. 2(4), p. 475–478, 2008.

[27] Bittermann, D., Squarer, D., Schulenberg, T., Oka, Y., Dumaz, P., Kryki-Rajmaki, R., Aksan, N., Maraczy, C., and Souryri., "A pontential Plant Characteristics of a High Performance Light Water Reactor," *ICAPP,* vol. 30046, 2003.

[28] Waata C., Schulenberg T., Cheng X.,, "Results of a coupled MCNP andsub-channel analysis of HPLWR fuel assembly," in *ICAPP 05*, Seoul Korea, May 15–19, Paper 5064., 2005.

[29] Gu H.Y., Li H.B., Hua Z.X., Liu D., Zhao M.,, "Heat transfer to supercritical water in a 2 × 2 rod bundle," *Annals of Nuclear Energy ,* vol. 83, p. 114–124, 2015.

[30] Schulenberg T., Leung L.,, "Super-critical water-cooled reactors," in *Handbook of Generation IV Nuclear Reactors.*, Germany, Elsevier Ltd., 2016, pp. 189-220.

[31] Oka, Y., Koshizuka, S., Ishiwatari, Y., Yamaji, A.,, Super Light Water Reactors and SuperFast Reactors, ISBN 978-1-4419-6034-4., 2010.

[32] Schulenberg, T., Starflinger, J.,, High Performance Light Water Reactor, Design and Analyses., KIT Scientific Publishing. ISBN:978-3-86644-817-9., 2012.

[33] Yetisir, M., Gaudet, M., Rhodes, D., Guzonas, D., Hamilton, H., Haque, Z., Pencer, J., Sartipi, A.,, "Reactor core and plant design of the Canadian supercritical water-cooled reactor," in *In: Proc. 2014 CanadaeChina Conference on Advanced Reactor Development (CCCARD-2014).*, Niagara Falls, Ontario, Canada, April 27-30, 2014, 2014.

[34] Schulenberg T., Leung L.K.H., Oka Y.,, "Review of R&D for supercritical water cooled reactors," *Progress in Nuclear Energy,* vol. 77, pp. 282-299, (2014).

[35] Novog, D., McGee, G., Rhodes, D., Yetisir, M.,, "Safety concepts and systems of the Canadian SCWR.," in *In: Proc. 3rd China-Canada Joint Workshop on Supercritical Water-Cooled Reactors (CCSC-2012),*, Xi'an, Shaanxi, China., 2012.

[36] Gaudet M., Yetisir M., & Haque, Z.,, "Physical aspects of the Canadian generation IV supercritical water-cooled pressure tube reactor plant design," in *In: Proc. 2014*

CanadaeChina Conference on Advanced Reactor Development (CCCARD-2014), Niagara Falls, Ontario, Canada, April 27e30., 2014.

[37] Ivankovic, Alojz, "Lecture notes for the course Computational Continuum Mechanics (CCM) UCD School of Electrical," www.ucd.ie/mecheng/ccm/CCM.pdf, Dublin, 2009.

[38] Suhas V. Pantakar, "Numerical Heat Transfer and fluid Flow," Hemisphere Publishing Corp.,, Washington, DC,, 1980.

[39] CD-ADAPCO, "CFD Basics. Americas Agency Training Document," 2008.

[40] Bishop A.A., Sandberg R.O., Tong L.S.,, "Forced convection heat transfer to water at near critical temperatures and supercritical pressures.," *WCAP,* pp. 2056-P,Part-III-B., 1964.

[41] Lemmon E. W., Huber M. L., & McLinden M. O., "NIST reference fluid thermodynamic and transport properties—REFPROP," NIST standard reference database,23, v7, 2002.

[42] Podila K., Rao Y.K.,, "CFD analysis of flow and heat transfer in Canadian supercritical water reactor bundle," *Annals of Nuclear Energy,* vol. 75, p. 1–10, 2014.

[43] CD-ADAPCO, "User Guide STAR-CCM+,Version 10.06.009”," New York, 2015.

[44] Wilcox D.C., Turbulence Modeling for CFD, 2nd edition ed., DCW Industries, Inc, 1998.

[45] Wilcox D.C.,, "Formulation of the k- $\boldsymbol{\omega}$ turbulence model revisited," *AIAA Journal,* vol. 46, no. 11, pp. 2823-2838., 2008.

[46] Durbin, P. A., "On the k-epsilon stagnation point anomaly.," *J. turbulence Heat and Mass Transfer,* vol. 17, pp. 89-90., 1986.

[47] Jones, W. P. and Launder, B. E., "The prediction of Laminarization with a Two Equation model of turbulence model," *International Journal, Heat and mass Transfer,* vol. 15, pp. 301-314., (1972).

[48] Menter, F.R., "“Two-equation eddy-viscosity turbulence modeling for engineering applications”," *AIAA Journal,* vol. 21(3), pp. pp. 1598-1605., 1994.

[49] D. Wilcox, "Formulation of the k-omega turbulence model revisited," *AIAA Journal,* vol. 46, no. 11, pp. 2823-2838, 2008.

[50] Ranz W.E., and Marshall W.R, "Evaporation from drops--Part I and II," *Chemical Engineering Progress,* vol. 48, no. 3, p. 141, 1952.

[51] Dittus F.W., Boelter L.M.K.,, "Heat transfer in automobile radiators of tubular type.," *University of California, Publications of Engineering,* vol. 13, pp. 443-461, 1930.

[52] Cheng X., Yang Y.H., Huang S.F.,, "A simplified method for heat transfer prediction of supercritical fluids in circular tubes," *Ann. Nucl. Energy,* vol. 36, pp. 1120-1128, 2009.

[53] Chen W.W., Fang X.D.,, "A new heat transfer correlation for supercritical water flowing in vertical tubes," *Int. J. Heat Mass Transf,* vol. 78, p. 156–160, 2014.

[54] Shitsi, E., Debrah, S. K., Agbodemegbe, V. Y., & Ampomah-Amoako, E., "Numerical investigation of heat transfer in parallel channels with water at supercritical pressure," *Heliyon,* vol. 3(11), p. e00453, 2017.

[55] B. P. A. Dyadyakin, "Heat transfer and thermal resistance of tight seven-rod bundle cooled with water flow at supercritical pressures," *Trans. VTI,* vol. 11, pp. 244-253, 1977.

[56] Griem H., "A New Procedure for the Prediction of Forced Convection Heat Transfer at Near- and Supercritical Pressure," *Heat and Mass Transfer,* vol. 31, pp. 301-305, 1996.

[57] Shitsman M.W., "Heat transfer to supercritical helium, carbon dioxide, and water: analysis of thermodynamic and transport properties and experimental data," *Cryogenics,* pp. 77-83, 1974.

[58] McAdams W.H., Kennel W.E. and Addoms J.N., "Heat Transfer to Superheated Steam at High Pressures," *Transactions of ASME,* vol. 72, pp. 421-428.

[59] Ornatsky A.P., Glushchenko L.P., Siomin E.T.,, "The research of temperature conditions of small diameter parallel tubes cooled by water under supercritical pressures," in *In: Proceedings of the 4th International Heat Transfer Conference*, Paris-Versailles, France. Elsevier, Amsterdam, 1970.

[60] Gupta S., Saltanov E., Mokr, S.J., Pioro I., Trevani L. and McGillivray D., "Developing Empirical Heat-Transfer Correlations for Supercritical CO2 Flowing in Vertical Bare Tubes.," *Nuclear Engineering and Design,,* vol. 261, pp. 116-131, 2013.

[61] Petukhov B.S., Kurganov V.A., Ankudinov V.B.,, "Heat transfer and flow resistance in the turbulent pipe flow of a fluid with near-critical state parameters," *High Temperatures,* vol. 21, pp. 81-89, 1983.

[62] Krasnoshchekov E.A., Protopopov V.S., Van F.,, "Experimental investigation of heat transfer for carbon dioxide in the supercritical region," in *In: Proceedings of the 2nd All-Soviet Union Conference on Heat and Mass Transfer*, Minsk, Belarus, 1967.

[63] Chen W.W., Fang X.D.,, "A new heat transfer correlation for supercritical water flowing in vertical tubes," *Int. J. Heat Mass Transf.,* vol. 78, pp. 165-160, 2014.

[64] Amoako E.A., Ambrosini W., "“Developing a CFD Methodology for the Analysis of Flow Stability in Heated Channels with Fluids at Supercritical Pressures”," *Annals of Nuclear Energy,* vol. 54, pp. 251-262, 2013.

[65] Wang H., Bi Q., Wang L., & Leung L. K., "Nonuniform heat transfer of supercritical water in a tight rod bundle–Assessment of correlations," *Annals of Nuclear Energy,* vol. 110, pp. 570-583, 2017.

[66] CASL, 2015.

[67] THINS, "THINS," 2013.

[68] Versteeg H. K., Malalasekera, W., "An Introduction to Computational Fluid Dynamics, the Finite Volume Method. Second edition.," 2007.

[69] Bardina J.E, Haung P.G., Coakley T.J., "Turbulence Modeling, Validation, Testing and Development.," in *28th Fluid Dynamics Conference, Fluid Dynamics and Co-located Conferences*, 1997.

[70] Compass Ingeniería y Sistemas, "Tdy Turbulence Handbook," 2015. [Online]. Available: http://www.compassis.com/downloads/Manuals/TdynTurbulenceHB.pdf. [Accessed 1 March 2018].

[71] Palko, D., Anglart, H.,, "Theoretical and numerical study of heat transfer deterioration in high performance light water reactor," ASME Press, New York, 2008.

[72] Zhu, Y.,, "Numerical investigation of flow and heat transfer within the core cooling channel of a super critical water reactor," Stuttgart, Germany., 2010.

[73] Spalart, P.R. and Rumsey, C.L., "“Effective Inflow Conditions for Turbulence Models in Aerodynamic Calculations”," *AIAA Journal,* vol. 45(10), pp. 2544-2553, 2007.

[74] Wigeland R., Hamman K.D.,, "“Fast Reactor Subassembly Design Modifications for Increasing," in *Proceedings of Global 2009*, Paris, France, 2009.

[75] Ishmael B.Celik, , "Introductory Turbulence Modeling Lecture Notes," 1999.

[76] Schulenberg, T., Visser, D.C.,, "Thermal-hydraulics and safety concepts of supercritical water cooled reactors," *Nucl. Eng. Des,* Vols. 264,, p. 231–237., 2013.

[77] Smith B.L., , "Thermal Hydraulics Laboratory on the Use of Computational Fluid Dynamics (CFD) in Reactor Technology.," 2013.

[78] Schatz, Markus, "Numerical Simulation Method," https://www.cfd.tu.-berlin.de /research/flow control/ gurneys/node4.html, 2004.

[79] Bakker, André, "Lecture-10: Turbulence Models. Applied Computational Fluid Dynamics.," 2002.

[80] Feng D.D.,, "Innovative fuel designs for high power density pressurized water reactor.," 2006..

[81] Ellis T.S., "Advanced design concepts for PWR and BWR high-performance annular fuel assemblies.," 2006..

[82] Paolo, M.,, "Design of annular fuel for high power density BWRs," 2005.

[83] Angelucci, M., Ambrosini, W., Forgione, N.,, "Numerical estimation of wall friction ratio near the pseudo-critical point with CFD models," *Nucl. Eng. Des.,* vol. 264, p. 71–79., 2013.

[84] Manceau, R. and Hanjalic, K., "Elliptic blending model: A new near-wall Reynolds-stress turbulence closure," *Nuclear Engineering & Design,* p. 4:744, 2002.

[85] Davidson, L., Nielsen, P. V. and Sveninsson A. , " Modification of V2F model for computing the flow in a 3D wall jet," *turbulence Heat and Mass Transfer,* vol. 7, pp. 577-584., (2003)..

[86] Abe, K., Kondoh, T. and Nagano, Y., " A new turbulence model for predicting fluid flow and heat transfer in separating and reattaching flows—I. Flow field calculations," *International Journal, Heat Mass Transfer,* vol. 3, p. 139–151., (1994).

[87] Lien, L.S., Kalitz G. and Durbin, P. A., "RANS modeling for compressible and transitional flows,," in *center for Turbulence Research Proceedings of Summer Program.*, (1998).

[88] International Atomic Energy Agency, "Heat Transfer Behaviour and Thermohydraulics Code Testing for Supercritical Water Cooled Reactors (SCWRs)," Vienna, Austria,, September 2014., p. 496 pp..

[89] Rohde, M., Peeters, J.W.R., Pucciarelli, A., Kiss, A., Rao, Y.F., Onder, E.N., M€uhlbauer, P., Batta, A., Hartig, M., Chatoorgoon, V., Thiele, R., Chang, D., Tavoularis, S., Novog, D., McClure, D., Gradecka, M., Takase, K.,, "A blind, numerical benchmark study on supercritical water heat transfer experiments in a 7-rod bundle," in *In: The 7th International Symposium on Supercritical Water-Cooled Reactors ISSCWR-7, March 15e18 paper 2044*, Helsinki, Finland., 2015.

[90] Guzonas, D., Novotny, R.,, "Supercritical water-cooled reactor materials - summary of research and open issues," *Progress in Nuclear Energy,* vol. 77, pp. 361-372, 2014..

[91] Luca Ammirabile, "Studies on supercritical water reactor fuel assemblies using the sub-channel code COBRA-EN," *Nuclear Engineering and Design ,* vol. 240 , p. 3087–3094, (2010) .

[92] Menter F.R., "Two-equation eddy-viscosity turbulence modeling for engineering applications," *AIAA Journal,* vol. 8, no. 32, pp. 1598-1605, 19994.

[93] Schulenberg T., Starflinger J., Heinecke J. , "Three pass core design proposal for a high performance light water reactor," *Progress in Nuclear Energy ,* vol. 50, pp. 526-531, 2008.

APPENDICES

APPENDIX A: Sub-channel Data from Wataa [17]

Sub-channel Label	**Area** (mm^2)	P_{ht} (mm)	P_{wt} (mm)	D_h (mm)	G_0 (kg/m^2s)
1	20.9	12.6	21.8	3.8	790.5
2	34.4	25.1	25.1	5.5	1003.2
3	14.7	9.4	12.7	4.6	894.3
4	34.4	25.1	25.1	5.5	1003.2
5	20.9	12.6	21.8	3.8	790.5
6	20.9	12.6	21.8	3.8	790.5
7	17.1	12.6	12.6	5.4	997.5
8	20.9	12.6	21.8	3.8	790.5
9	3.5	3.1	7.1	2	510.7

NB: P_w is the wetted perimeter, P_{ht} is the heated perimeter

The diameter of each individual sub-channel is defined by the equation (i):

$$D_h = \frac{4A}{P_w} \qquad \text{(i)}$$

Where D_h is the hydraulic diameter (mm), A is the cross sectional area (mm^2) of a sub-channel and P_w is the wetted perimeter (mm)

APPENDIX B: Heat transfer correlations applicability range

References	Applicability Range
Dittus and Boelter [44]	Subcritical pressures
Shitsman [47]	P = 0.4–27.4 MPa; G = 170–3000 kg/m^2 s; q = 420–8400 kW/m^2; t_b = 2.5–420 °C
Bishop et al. [48]	P = 22.8–27.6 MPa; G = 651–3662 kg/m^2 s; q = 310–3460 kW/m^2; t_b = 282–527 °C
Ornatsky et al. [50]	P = 22.6–29.4 MPa; G = 450–3000 kg/m2 s; q = 280–1200 kW/m^2; H_{in} = 420–1400 kJ/kg
Griem [46]	P = 23 - 25 MPa, q = 0.3 - 0.6 MW/m^2, and G = 500 - 2500 kg/m^{2}s
McAdams et al. [49]	P = 0.8 - 24 MPa, t_b = 221°C - 538°C, q = 0.035 - 0.336 MW/m^2 and G = 75 - 224 kg/m^{2}s
Dyadyakin and Popov [45]	P = 24.5 MPa; G = 500–4000 kg/m^2 s; q < 4700 kW/m^2; t_b = 90–570 °C
Mokry et al. [9]	P = 24 MPa; G = 200–1500 kg/m^2 s; q = 70–1250 kW/m^2; tin = 320–350 °C
Gupta et al. [51]	P = 24 MPa; G = 200–1500 kg/m^2 s; q = 70–1250 kW/m^2; tin = 320–350 °C
Petukhov et al. [52]	P = 7.7 -8.9 MPa; G = 1000-4100 kg/m^2 s; q = 384-1053 kW/m^2; t_b = 0-80 °C
Krasnoshchekov-Protopopov [53]	$2\times10^4 < Re_b < 8.6\times10^5$, $0.85<$ [illegible] < 65: $0.90 <$ [illegible] <3.60; $1.00<$ [illegible] <6.00 and $0.07 <$ [illegible] < 4.50
Cheng et al. [54]	P = 22.5–25 MPa; G = 700–3500 kg/m^2 s; q = 300–2000 kW/m^2; t_b = 300–450 °C
Chen and Fang [55]	P = 22–34.3 MPa; G = 201–2500 kg/m^2 s; q = 129–1735 kW/m^2; H_b = 278–3169 kJ/kg

APPENDIX C: Water Properties Tools

C1: Thermo-physical properties of the fluid materials tool

Thermophysical Properties of Fluid Systems

Accurate thermophysical properties are available for several fluids. These data include the following:

Density	Specific volume
C_p	C_v
Enthalpy	Entropy
Internal energy	Speed of Sound
Viscosity	Thermal conductivity
Joule-Thomson coefficient	Surface tension (saturation curve only)

Please follow the steps below to select the data required.

1. Please select the species of interest:

   Water

2. Please choose the units you wish to use:

   Temperature ◉ Kelvin ○ Celsius ○ Fahrenheit ○ Rankine

   Pressure ◉ MPa ○ bar ○ atm. ○ torr ○ psia

   Density ◉ mol/l ○ mol/m³ ○ g/ml ○ kg/m³ ○ lb-mole/ft³ ○ lbm/ft³

   Energy ◉ kJ/mol ○ kJ/kg ○ kcal/mol ○ Btu/lb-mole ○ kcal/g ○ Btu/lbm

   Velocity ◉ m/s ○ ft/s ○ mph

   Viscosity ◉ µPa*s ○ Pa*s ○ cP ○ lbm/ft*s

   Surface tension* ◉ N/m ○ dyn/cm ○ lb/ft ○ lb/in

3. *Surface tension values are only available along the saturation curve.

4. Choose the desired type of data:

   Data type ◉ Isothermal properties ○ Isobaric properties ○ Isochoric properties ○ Saturation properties — temperature increments ○ Saturation properties — pressure increments

5. Please select the desired standard state convention:

   Standard state convention ◉ Default for fluid ○ Normal B.P. convention ○ ASHRAE convention ○ IIR convention

C 2: Isothermal Properties for Water tool

Isothermal Properties for Water

This option will supply data on a constant temperature curve over the specified pressure range. Values should not extend extend outside the minimum and maximum values given. Calculations are limited to a maxium of 601 data points; increments resulting in a larger number of points will be adjusted upward to limit the number of points computed.

1. Enter temperature in selected units:
   [ ] (Acceptable range: 273.16 to 1275.0 K)
2. Enter pressure range and increment in selected units:
   P_{Low} [ ] (min value: 0.0 MPa)
   P_{High}* [ ]
   $P_{Increment}$ [ ]
3. * The maximum pressure limit is the lowest of the following values:
   - 1000.0000 MPa
   - The pressure at which a density of 73.96 mol/l is reached.
4. Check here if you want to use the intereactive display (requires JavaScript and HTML 5 canvas capable browser) [x]
5. Number of digits to be displayed in tables (does not effect accuracy of computations):
   [ ]
6. Press for Data

C 3: Compressed Water and Superheated Steam Properties

25 MPa				
v	ρ	h	s	t, °C
1.3459	743.02	1331.3	3.1919	**300**
1.3810	724.09	1384.1	3.2832	**310**
1.4215	703.49	1438.9	3.3764	**320**
1.4690	680.74	1496.4	3.4726	**330**
1.5264	655.13	1557.5	3.5731	**340**
1.5988	625.45	1623.9	3.6804	**350**
1.6969	589.31	1698.6	3.7993	**360**
1.8503	540.46	1789.8	3.9423	**370**
2.2182	450.82	1935.7	4.1671	**380**
4.6474	215.18	2395.7	4.8660	**390**
6.0047	166.54	2578.6	5.1400	**400**
6.8833	145.28	2687.1	5.3000	**410**
7.5792	131.94	2769.4	5.4197	**420**
8.1725	122.36	2837.8	5.5176	**430**
8.6986	114.96	2897.3	5.6016	**440**
9.1763	108.98	2950.6	5.6759	**450**
9.6176	103.98	2999.4	5.7428	**460**
10.030	99.701	3044.6	5.8042	**470**
10.419	95.976	3087.2	5.8610	**480**
10.789	92.686	3127.5	5.9142	**490**
11.143	89.744	3165.9	5.9642	**500**
11.811	84.670	3238.4	6.0569	**520**
12.436	80.411	3306.5	6.1416	**540**
13.029	76.752	3371.2	6.2202	**560**
13.595	73.555	3433.3	6.2940	**580**
14.140	70.720	3493.5	6.3637	**600**
14.667	68.180	3552.1	6.4300	**620**
15.179	65.881	3609.4	6.4935	**640**
15.678	63.785	3665.7	6.5545	**660**
16.165	61.861	3721.2	6.6133	**680**

APPENDIX D: Density variation in all 9 sub-channels

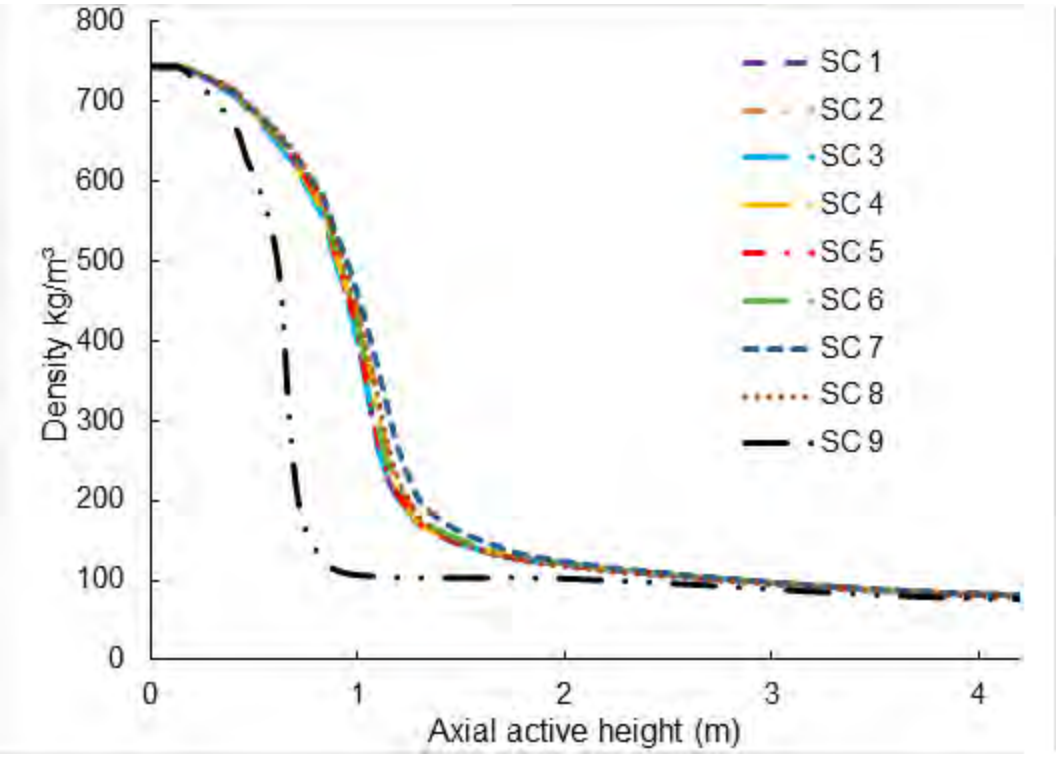

Density variation in all the sub-channels (using K-Omega SST turbulence model)

- The coolant density is observed to decrease steadily with increasing assembly height.
- The coolant density decreases from 743.01 kg/m³ at the inlet to about 77 kg/m³ similar to what Wataa (2006) obtained.
- Density is SC 9 is lower, due to the low mass flux.

APPENDIX E: Temperature profiles at 0.25 m, 2 m and 4 m

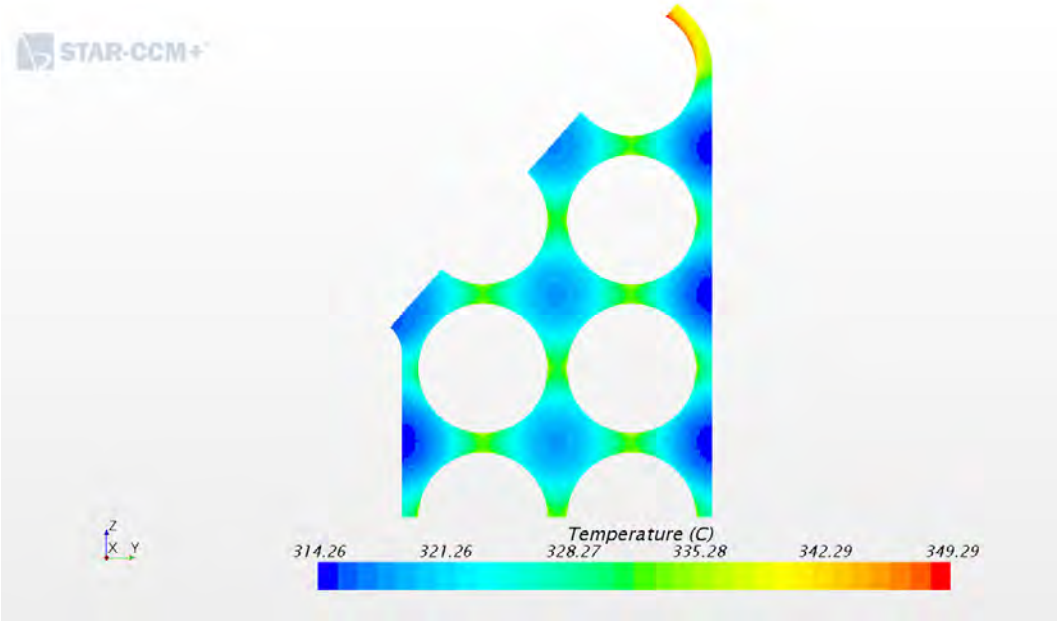

Temperature profiles at 0.25 m

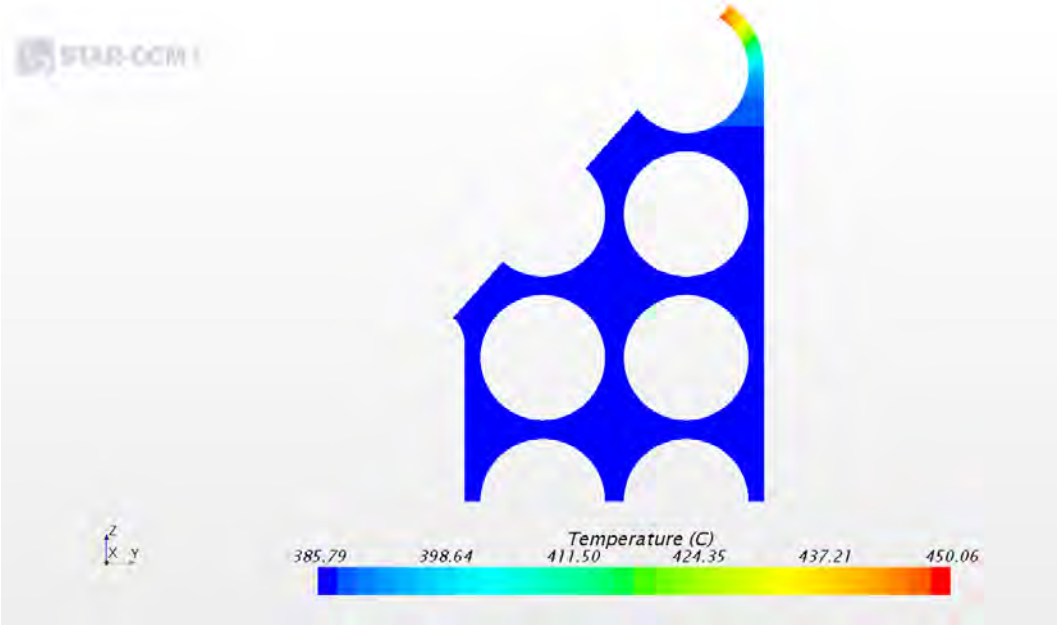

Temperature profiles at 2 m

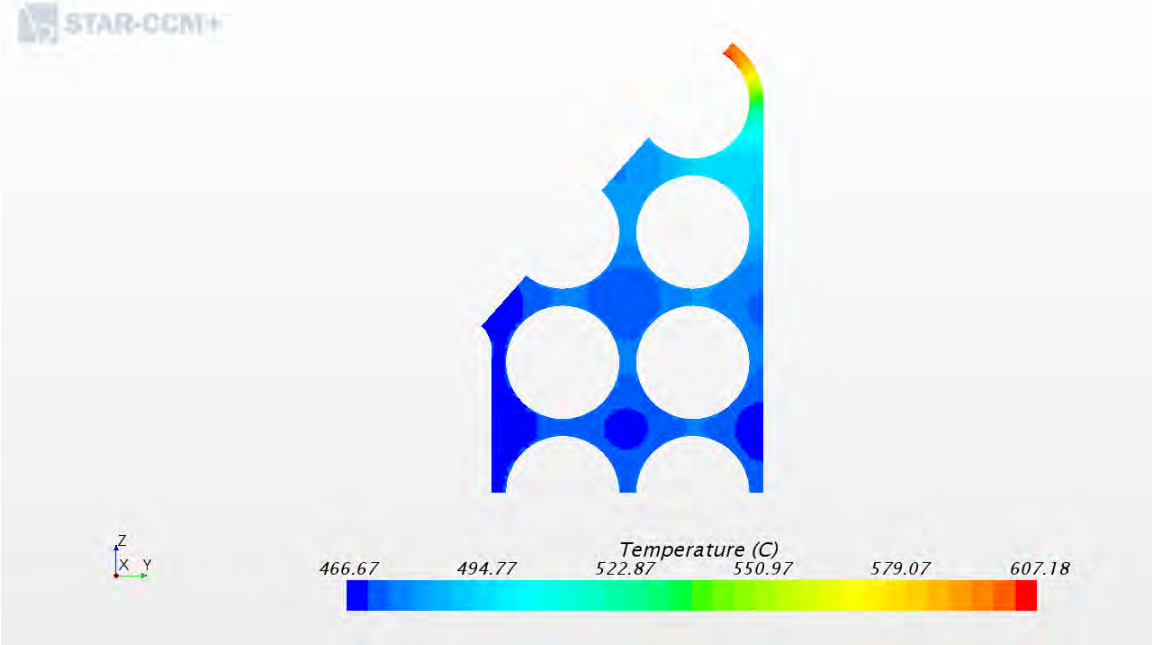

Temperature profiles at 4 m

NB: Obtained using κ-ω SST Turbulence Model

APPENDIX F: Turbulence model's Simulation Results

F 1-AKN Turbulence model Predicted SC Coolant Temperatures

SCs: Direction [1,0,0] (m)	SC 1: Temperature (°C)	SC 2: Temperature (°C)	SC 3: Temperature (°C)	SC 4: Temperature (°C)	SC 5: Temperature (°C)	SC 6: Temperature (°C)	SC 7: Temperature (°C)	SC 8: Temperature (°C)	SC 9: Temperature (°C)
0	300.00	300.12	300.16	302.23	299.82	300.10	303.62	299.83	301.22
0.21	317.66	318.17	318.08	318.11	317.75	317.76	317.89	319.01	327.66
0.42	333.97	334.30	334.19	334.22	334.15	334.44	334.38	336.70	344.29
0.63	349.90	350.12	350.08	350.21	350.24	350.80	350.85	353.22	358.73
0.84	362.56	362.73	362.72	362.95	362.98	363.60	363.76	365.57	369.00
1.05	373.03	373.17	373.18	373.42	373.43	373.90	374.05	375.09	376.63
1.26	379.19	379.26	379.28	379.42	379.42	379.68	379.77	380.24	380.82
1.47	382.71	382.74	382.75	382.81	382.81	382.91	382.96	383.10	383.27
1.68	384.40	384.41	384.41	384.44	384.44	384.48	384.50	384.55	384.60
1.89	385.14	385.15	385.15	385.15	385.12	385.12	385.14	385.10	385.10
2.1	385.19	385.21	385.20	385.20	385.18	385.17	385.19	385.16	385.15
2.31	385.17	385.19	385.18	385.19	385.16	385.15	385.17	385.13	385.13
2.52	385.14	385.16	385.15	385.15	385.12	385.11	385.13	385.10	385.09
2.73	385.12	385.14	385.13	385.14	385.11	385.10	385.12	385.09	385.09
2.94	385.16	385.18	385.17	385.18	385.15	385.14	385.16	385.13	385.13
3.15	385.20	385.22	385.21	385.21	385.19	385.18	385.20	385.16	385.16
3.36	385.21	385.23	385.22	385.23	385.20	385.19	385.21	385.18	385.18
3.57	385.24	385.26	385.25	385.26	385.23	385.22	385.24	385.20	385.20
3.78	385.20	385.21	385.21	385.21	385.18	385.18	385.19	385.16	385.16
3.99	385.31	385.33	385.32	385.33	385.30	385.30	385.32	385.30	385.30
4.2	385.45	385.47	385.46	385.46	385.44	385.44	385.45	385.43	385.43

F 2-AKN Turbulence model Predicted Average Wall Temperatures

SCs: Direction [1,0,0] (m)	Avg T_W (°C) SC 1	Avg T_W (°C) SC 2	Avg T_W (°C) SC 3	Avg T_W (°C) SC 4	Avg T_W (°C) SC 5	Avg T_W (°C) SC 6	Avg T_W (°C) SC 7	Avg T_W (°C) SC 8	Avg T_W (°C) SC 9
0.21	320.21	320.24	320.17	320.20	320.27	324.24	322.88	324.24	328.26
0.42	337.32	337.35	337.31	337.37	337.37	341.20	339.92	341.20	344.77
0.63	351.34	351.36	351.30	351.42	351.39	355.42	354.03	355.42	359.02
0.84	363.55	363.61	363.59	363.72	363.67	366.63	365.62	366.63	369.17
1.05	373.60	373.65	373.67	373.77	373.70	375.38	374.81	375.38	376.70
1.26	379.45	379.48	379.51	379.57	379.51	380.29	380.03	380.29	380.85
1.47	382.80	382.82	382.83	382.85	382.83	383.09	383.00	383.09	383.28
1.68	384.50	384.54	384.44	384.52	384.58	384.60	384.55	384.60	384.60
1.89	385.16	385.16	385.16	385.16	385.16	385.12	385.14	385.12	385.10
2.1	385.22	385.21	385.22	385.21	385.21	385.18	385.19	385.18	385.16
2.31	385.20	385.20	385.20	385.19	385.19	385.15	385.17	385.15	385.13
2.52	385.16	385.16	385.16	385.16	385.15	385.12	385.13	385.12	385.09
2.73	385.15	385.14	385.15	385.15	385.14	385.11	385.12	385.11	385.09
2.94	385.19	385.19	385.19	385.19	385.18	385.15	385.16	385.15	385.13
3.15	385.22	385.22	385.23	385.22	385.22	385.18	385.20	385.18	385.16
3.36	385.24	385.23	385.24	385.23	385.23	385.20	385.21	385.20	385.18
3.57	385.27	385.26	385.27	385.26	385.26	385.22	385.24	385.22	385.20
3.78	385.22	385.22	385.22	385.22	385.22	385.18	385.20	385.18	385.16
3.99	385.34	385.34	385.34	385.34	385.34	385.31	385.32	385.31	385.30
4.2	385.48	385.48	385.48	385.47	385.48	385.44	385.44	385.44	385.43

F 3-Lien's Standard Lo-Re κ-ε Turbulence model Predicted SC Coolant Temperatures

Direction [1,0,0] (m)	SC 1: Temperature (°C)	SC 2: Temperature (°C)	SC 3: Temperature (°C)	SC 4: Temperature (°C)	SC 5: Temperature (°C)	SC 6: Temperature (°C)	SC 7: Temperature (°C)	SC8: Temperature (°C)	SC 9: Temperature (°C)
0	301.03	300.23	300.98	300.15	300.94	301.03	301.03	301.03	301.19
0.21	332.48	332.51	332.48	332.47	332.40	332.36	332.40	332.30	332.28
0.42	332.33	332.36	332.34	332.33	332.27	332.24	332.28	332.21	332.22
0.63	335.68	335.70	335.68	335.66	335.61	335.56	335.58	335.50	335.50
0.84	341.94	341.96	341.93	341.91	341.88	341.81	341.82	341.76	341.78
1.05	346.18	346.22	346.19	346.17	346.09	346.04	346.08	345.95	345.92
1.26	344.55	344.61	344.58	344.57	344.39	344.33	344.42	344.18	344.04
1.47	339.40	339.41	339.38	339.35	339.36	339.29	339.26	339.23	339.30
1.68	346.19	346.20	346.17	346.17	346.15	346.12	346.13	346.10	346.15
1.89	350.66	350.67	350.64	350.61	350.59	350.52	350.51	350.45	350.47
2.1	351.40	351.44	351.42	351.40	351.28	351.22	351.28	351.11	351.03
2.31	369.69	369.68	369.67	369.65	369.68	369.65	369.63	369.66	369.74
2.52	361.37	361.43	361.41	361.41	361.25	361.21	361.31	361.13	361.04
2.73	354.05	354.12	354.12	354.19	354.08	354.16	354.28	354.28	354.36
2.94	367.21	367.22	367.20	367.21	367.24	367.25	367.25	367.31	367.42
3.15	377.43	377.42	377.40	377.38	377.43	377.39	377.36	377.39	377.46
3.36	379.76	379.76	379.74	379.71	379.68	379.61	379.61	379.51	379.46
3.57	381.60	381.59	381.59	381.59	381.63	381.64	381.61	381.68	381.76
3.78	383.98	383.97	383.96	383.94	383.96	383.92	383.89	383.88	383.89
3.99	384.68	384.67	384.66	384.63	384.63	384.60	384.59	384.55	384.54
4.2	384.44	384.43	384.42	384.39	384.43	384.39	384.37	384.38	384.40

F 4-Lien's Standard Lo-Re κ-ε Turbulence model Predicted Average Wall Temperatures

Wall 2: Direction [1,0,0] (m)	Avg Tw (°C) SC 1	Avg Tw (°C)SC 2	Avg Tw (°C) SC 3	Avg Tw (°C) SC 4	Avg Tw (°C) SC 5	Avg Tw (°C) SC 6	Avg Tw (°C) SC 7	Avg Tw (°C) SC 8	Avg Tw (°C) SC 9
0.21	332.53	332.52	332.52	332.50	332.50	332.48	332.41	332.36	332.29
0.42	332.71	332.70	332.70	332.69	332.69	332.68	332.53	332.44	332.22
0.63	335.72	335.71	335.71	335.69	335.70	335.68	335.62	335.57	335.50
0.84	341.97	341.97	341.96	341.94	341.95	341.93	341.87	341.83	341.79
1.05	346.23	346.22	346.22	346.20	346.20	346.18	346.09	346.02	345.92
1.26	344.61	344.59	344.61	344.58	344.56	344.54	344.37	344.25	344.04
1.47	339.43	339.42	339.40	339.39	339.41	339.38	339.35	339.32	339.30
1.68	346.86	347.17	346.21	346.84	346.84	347.46	346.60	346.80	346.16
1.89	350.69	350.68	350.67	350.65	350.66	350.63	350.57	350.53	350.47
2.1	350.74	351.08	350.73	350.71	351.41	350.69	350.80	350.48	351.03
2.31	369.70	369.70	369.69	369.69	369.69	369.68	369.70	369.71	369.74
2.52	360.53	360.06	360.54	360.51	360.49	360.48	361.27	361.19	361.05
2.73	354.15	354.15	354.18	354.19	354.16	354.20	354.25	354.29	354.36
2.94	368.05	367.65	368.87	368.06	368.06	367.25	368.39	368.16	369.05
3.15	377.43	377.43	377.41	377.41	377.43	377.41	377.42	377.43	377.46
3.36	379.56	379.55	379.55	379.63	379.34	379.71	379.49	379.57	379.46
3.57	381.61	381.61	381.60	381.61	381.61	381.61	381.66	381.69	381.76
3.78	384.05	384.01	384.04	384.00	383.97	383.95	383.93	383.91	383.89
3.99	384.67	384.66	384.65	384.65	384.65	384.64	384.60	384.58	384.54
4.2	384.42	384.42	384.42	384.41	384.39	384.41	384.40	384.40	384.40

F 5: SST (Menter's) κ-ω Turbulence model Predicted SC Coolant Temperatures

Direction [1,0,0] (m)	SC 1 Temperature (°C)	SC 2: Temperature (°C)	SC 3: Temperature (°C)	SC 4: Temperature (°C)	SC 5: Temperature (°C)	SC 6: Temperature (°C)	SC 7: Temperature (°C)	SC 8: Temperature (°C)	SC 9: Temperature (°C)
0	300.25	300.01	299.98	303.21	299.96	299.98	300.05	299.96	301.15
0.21	313.44	314.76	315.39	314.73	313.23	313.17	315.07	313.20	333.22
0.42	329.62	331.81	331.71	331.77	329.52	329.48	331.19	329.73	358.27
0.63	346.04	348.36	347.85	348.26	346.10	346.07	347.09	346.76	375.05
0.84	359.26	361.45	360.75	361.31	359.42	359.39	359.91	360.80	382.18
1.05	370.66	372.29	371.65	372.14	370.83	370.81	371.03	372.88	385.14
1.26	377.70	378.62	378.24	378.51	377.82	377.83	377.88	379.72	388.15
1.47	381.99	382.32	382.17	382.25	382.08	382.11	382.02	383.27	393.47
1.68	383.92	384.07	383.99	384.02	383.99	384.03	383.93	384.87	399.98
1.89	385.27	385.38	385.30	385.33	385.35	385.42	385.33	386.50	407.05
2.1	386.60	386.75	386.63	386.69	386.73	386.87	386.79	388.69	414.16
2.31	388.77	389.03	388.82	388.96	389.00	389.32	389.34	392.42	423.56
2.52	391.75	392.15	391.84	392.12	392.12	392.72	392.94	397.38	432.80
2.73	396.52	397.16	396.73	397.28	397.14	398.21	398.86	404.78	444.37
2.94	402.55	403.42	402.94	403.77	403.43	405.02	406.13	413.50	457.05
3.15	411.08	412.28	411.74	413.02	412.31	414.62	416.47	425.75	472.48
3.36	421.06	422.66	422.07	423.90	422.72	425.89	428.55	439.04	488.79
3.57	434.89	436.88	436.38	438.70	436.96	440.93	444.35	455.74	511.03
3.78	449.48	451.79	451.39	454.10	451.85	456.53	460.58	473.13	533.87
3.99	467.69	470.39	470.09	473.29	470.43	475.95	480.70	494.64	560.73
4.2	486.98	490.24	489.90	493.69	490.14	496.46	501.90	517.10	587.88

F 6: SST (Menter's) κ-ω Turbulence model Predicted SC Wall Temperatures

Direction [1,0,0] (m)	Avg T_w SC 1 (°C)	Avg T_w SC 2 (°C)	Avg T_w SC 3 (°C)	Avg T_w SC 4 (°C)	Avg T_w SC 5 (°C)	Avg T_w SC 6 (°C)	Avg T_w SC 7(°C)	Avg T_w SC 8 (°C)	Avg T_w SC 9 (°C)
0.21	331.28	331.37	331.06	331.18	331.46	331.31	334.07	335.54	339.82
0.42	346.98	346.93	346.86	346.91	346.87	346.96	352.71	355.47	363.52
0.63	359.42	359.35	359.19	359.26	359.29	359.33	365.31	368.37	377.07
0.84	369.27	369.32	369.26	369.28	369.37	369.29	373.87	376.12	382.95
1.05	376.86	376.88	376.83	376.84	376.90	376.85	379.75	381.23	385.60
1.26	381.00	381.01	380.98	381.00	381.01	381.02	383.82	385.25	389.43
1.47	383.38	383.39	383.35	383.36	383.40	383.38	387.45	389.50	395.60
1.68	384.71	384.73	384.61	384.68	384.76	384.76	390.98	394.17	403.54
1.89	385.88	385.90	385.85	385.87	385.91	385.90	394.15	398.30	410.66
2.1	387.49	387.46	387.41	387.46	387.43	387.52	397.70	402.91	418.14
2.31	389.92	389.94	389.81	389.91	389.95	390.01	402.60	409.03	427.89
2.52	393.52	393.69	393.46	393.62	393.85	393.77	408.33	415.90	437.97
2.73	398.79	398.86	398.74	398.97	398.93	399.21	415.77	424.34	449.04
2.94	405.92	405.84	406.34	406.29	405.76	406.23	425.54	435.18	463.51
3.15	414.95	415.13	415.08	415.55	415.30	416.02	436.59	447.38	477.92
3.36	426.64	426.84	426.92	427.23	427.03	427.53	450.20	461.61	494.49
3.57	440.91	441.18	441.45	442.18	441.45	442.92	467.48	480.56	516.84
3.78	457.33	457.27	458.16	458.56	457.21	458.96	486.17	500.54	540.56
3.99	476.14	476.54	477.08	478.05	476.94	479.02	508.75	524.58	568.26
4.2	497.87	497.86	497.87	499.34	497.84	500.08	548.83	548.83	595.33

F 8: Standard (Wilcox) κ-ω Turbulence model Predicted SC Coolant Temperatures

Direction [1,0,0] (m)	SC 1: Temperature (°C)	SC 2: Temperature (°C)	SC 3: Temperature (°C)	SC 5: Temperature (°C)	SC 6: Temperature (°C)	SC 7: Temperature (°C)	SC 8: Temperature (°C)	SC 9: Temperature (°C)
0	300.03	301.36	300.01	299.96	300.58	300.23	299.96	301.15
0.21	313.25	314.38	315.44	313.04	312.98	314.96	313.02	334.06
0.42	329.55	331.47	331.79	329.47	329.44	331.05	329.72	359.49
0.63	346.03	348.08	347.91	346.12	346.10	346.96	346.94	375.63
0.84	359.29	361.25	360.81	359.50	359.48	359.84	361.15	382.21
1.05	370.75	372.23	371.73	370.99	370.99	371.06	373.27	384.87
1.26	377.75	378.63	378.30	377.91	377.94	377.95	379.94	387.23
1.47	381.99	382.35	382.19	382.09	382.14	382.12	383.34	391.16
1.68	383.92	384.09	384.00	383.99	384.05	384.02	384.90	395.86
1.89	385.26	385.40	385.31	385.34	385.43	385.43	386.52	401.08
2.1	386.59	386.78	386.65	386.72	386.90	386.95	388.68	406.30
2.31	388.76	389.06	388.86	389.00	389.38	389.63	392.30	413.34
2.52	391.74	392.19	391.93	392.13	392.81	393.36	397.09	420.96
2.73	396.53	397.24	396.91	397.18	398.35	399.42	404.21	431.15
2.94	402.61	403.54	403.22	403.51	405.21	406.78	412.58	442.52
3.15	411.24	412.49	412.18	412.46	414.86	417.19	424.36	456.60
3.36	421.35	422.97	422.69	422.96	426.17	429.26	437.29	471.69
3.57	435.36	437.32	437.20	437.33	441.23	444.94	453.58	492.29
3.78	450.13	452.37	452.38	452.36	456.85	461.07	470.56	513.96
3.99	468.56	471.15	471.26	471.08	476.26	481.07	491.62	539.79
4.2	488.08	491.18	491.25	490.96	496.79	502.14	513.72	566.15

F 9: Standard (Wilcox) κ-ω Turbulence model Predicted Wall Temperatures

Direction [1,0,0] (m)	Avg Tw (°C) SC 1	Avg Tw (°C) SC 2	Avg Tw (°C) SC 3	Avg Tw (°C) SC 4	Avg Tw (°C) SC 5	Avg Tw (°C) SC 6	Avg Tw (°C) SC 7	Avg Tw (°C) SC 8	Avg Tw (°C) SC 9
0.21	330.63	330.74	330.42	330.58	330.85	330.74	333.53	335.02	339.30
0.42	346.23	346.21	346.18	346.25	346.19	346.32	352.29	355.15	363.46
0.63	358.79	358.72	358.61	358.67	358.65	358.73	364.95	368.12	377.16
0.84	368.75	368.79	368.73	368.75	368.83	368.77	373.48	375.81	382.83
1.05	376.50	376.52	376.46	376.49	376.54	376.51	379.40	380.87	385.22
1.26	380.78	380.79	380.77	380.79	380.81	380.81	383.20	384.42	388.00
1.47	383.27	383.29	383.24	383.26	383.30	383.27	386.30	387.84	392.41
1.68	384.64	384.67	384.54	384.62	384.70	384.70	389.05	391.32	397.92
1.89	385.81	385.83	385.79	385.81	385.85	385.84	391.62	394.54	403.20
2.1	387.39	387.37	387.34	387.39	387.34	387.45	394.44	398.06	408.50
2.31	389.80	389.82	389.73	389.83	389.84	389.93	398.50	402.92	415.75
2.52	393.36	393.53	393.38	393.53	393.70	393.69	403.59	408.82	423.90
2.73	398.60	398.67	398.66	398.90	398.75	399.13	410.68	416.73	433.91
2.94	405.70	405.63	406.29	406.22	405.56	406.15	419.92	426.77	446.76
3.15	414.75	414.93	415.09	415.53	415.10	415.97	430.54	438.28	459.77
3.36	426.45	426.65	426.98	427.24	426.86	427.50	443.76	451.87	475.10
3.57	440.79	441.05	441.57	442.23	441.31	442.89	460.54	470.04	495.91
3.78	457.25	457.17	458.30	458.61	457.09	458.91	478.74	489.29	518.20
3.99	476.09	476.46	477.25	478.08	476.83	478.92	500.85	512.61	544.59
4.2	497.99	497.99	497.99	499.32	497.98	499.98	536.51	536.51	571.04